Università Degli Studi Di Salerno

Dipartimento di Fisica "E.R. Caianiello"

Dottorato di Ricerca in Matematica, Fisica e Applicazioni

Curriculum: FISICA

XXX Ciclo – II Serie

2014-2017

Low and high field Magnetic Resonance Imaging and its application in food science and plants

Cristina Ripoli

Tutor :

Prof. SALVATORE DE PASQUALE

PhD Coordinator :

Prof. ROBERTO SCARPA

Index

Introduction

Nuclear Magnetic Resonance (NMR) and Magnetic Resonance Imaging (MRI) are techniques that have seen a remarkable success and a fast growth over the past decades.

These techniques, extensively used as survey and investigation tools in several fields, give usually a relatively rapid response, have a good level of accuracy and does not present the harmful disadvantages of other diagnostic approaches based on ionizing radiations.

In particular, MRI emerged as a medical imaging technique to obtain pictures of the anatomy and physiological processes of organs and body structures in both health and disease. Even if originally developed in the medical field, it is nowadays used in a large number of disciplines to study a wide variety of processes and materials.

MRI technique involves a nice combination of superconductivity, cryogenics, quantum physics, digital and computer technology.

Thanks to its non-invasivity and non-descrutivity, the MRI enhances its potential to perform inspections and studies of the internal structure of material samples without modifications caused by the measurements.

In particular, in the field of food science, the understanding of global information about the food matrix and a better identification of the determinants characterizing food quality and safety represent a new challenge and MRI has proven to be a very promising answer.

This technique can be used to acquire 2-dimensional (2D) and 3-dimensional (3D) high spatial resolution images of the internal structure of the material under study. The signal of each voxel depends on the physical properties of the sample such as proton density, relaxation times, temperature and diffusion.

Information extracted from the images can be exploited for spatially resolved measurements of concentration, structure, temperature, velocity, and diffusivity.

MRI, as non-destructive technique, allows the study of intact samples such as fruits and vegetables. Due to the presence of a high water content in these products, MRI can be useful to obtain information about tissue properties and, thanks of its sensitivity, can trace water distribution and migration.

MRI shows a great potential for the investigation of the structural changes induced by food processes and allows the characterization of vegetable and plant structure. The characteristic NMR relaxation times are used as parameters for the quantification of water content or for the extraction of information related to changes in microstructure.

Nevertheless, the way to affirm the MRI as a recognized tool for the assessment of food properties, quality, processing and storage is still quite long and the implementation of simple and fast protocols, suitable to respond to food industry demands, is far to be reached. The idea behind this thesis is the investigation of new methodologies intended to carry out fast and accurate evaluation of moisture content in a food matrix through MRI. At the same time the development of appropriate protocols and analysis tools allowing a simple extraction of those information in a reproducible and reliable way.

This thesis work is divided into six chapters.

Chapter 1 and 2 offer a general introduction respectively to the NMR physics and to the imaging technique based on it. In particular, the processes behind the image formation and the used sequences are discussed.

A general description of the instrument is presented in chapter 3.

Chapter 4 provide a short overview of the most prominent applications of MRI and the state of the art in various fields of use.

In chapter 5, we explain our advances in efforts to develop an objective, accurate and non-invasive tool for the detection and quantification of the moisture content in a specific food matrix. Two different approaches have been used, both based on data extracted by MR Imaging and a comparison of the two methods is presented. The goal is to exploit MRI as a real measurement instrument with a simple and

fast measurement protocol: to achieve this goal we need to identify quantitative MR parameters that provide the most relevant information with respect to the physical quantities we want to measure.

The final chapter describes a preliminary MRI study of in vivo monitoring of plants behaviour and their growing inside the spectrometer. The determination of roots viability, water uptake and absorption of nutrients can be explored through MRI in a continuous way with very light interference on the plant development. The first results and the perspectives of this kind of studies are presented.

The thesis ends with a general conclusion where are summarized the main results and the key perspectives for future work.

1. Principles of Nuclear Magnetic Resonance

The Nuclear Magnetic Resonance (NMR) is a quantum mechanical phenomenon in nature, but at the macroscopic scale, it is possible to describe it quite accurately using semi-classical physics. This point of view allows having a practical and simpler approach to understand the NMR phenomenon.

1.1 A mix description

Electrons, protons and neutrons are particles inherently provided with spin, characterized by quantum behaviour. The angular momentum associated with the spin is:

$$L = \hbar\sqrt{I(I+1)} \quad ; \quad \hbar = \frac{h}{2\pi}, \tag{1}$$

where I is the spin number and $h = 6{,}63\ 10^{-34}\ Js^2$ is the Plank constant.

For nuclei possessing an odd mass number, I value is a half-integer, like the hydrogen (^{1}H) which possess a spin of +1/2 (Table 1).

Nucleus	Spin quantum number I
^{1}H	1/2
^{13}C	1/2
^{19}F	1/2
^{31}P	1/2
^{23}Na	3/2

Table 1 *Spin quantum numbers for some nuclei.*

The components measured along the axis are quantized. The quantum number m may have only (2I + 1) value and may be any one of a discrete set of integer or half-integer values in the range:

$$m_I = I, I-1, \ldots\ldots, -I\,, \tag{2}$$

that correspond to the basis states of the particles.

Atomic nuclei have a magnetic dipole moment proportional to the angular momentum:

$$\vec{\mu} = \gamma\,\vec{L} = \gamma\,\hbar\,\vec{I}\,. \tag{3}$$

The constant of proportionality is the gyromagnetic ratio, γ, it is the ratio of the magnetic moment to the angular momentum and it depends on the considered nuclei, for the proton $\gamma_P = 268\,MHz/T$. The gyromagnetic ratio over 2π, gives most common value used in NMR: $\gamma_P = 42{,}56\,MHz/T$.

The component of the angular momentum and the corresponding magnetic moment along the z-axis are respectively given by:

$$L_z = \hbar\,m_I \quad ; \quad \mu_z = \gamma\,\hbar\,m_I\,. \tag{4}$$

Applying an external magnetic field $\vec{B}$ the interaction energy of a magnetic dipole $\vec{\mu}$ with the field is:

$$E = -\vec{\mu}\cdot\vec{B}\,. \tag{5}$$

The consequence is the splitting of the energy levels that occurs because of the interaction of the magnetic moment $\vec{\mu}$ of the atom with the magnetic field $\vec{B}$, slightly shifting the energy of the atomic levels.

Considering $\vec{B}$ oriented on the z-axis,$\vec{B}_0 = B_0\hat{k}$, the (5) reduces to:

$$E_I = -\mu_z B_0 = -\gamma\, \hbar\, m_I B_0 \tag{6}$$

Remembering that for the proton I=1/2, along the z-axis, *m* can only result in two values:

$$m_I = {}^1/_2, -{}^1/_2 \tag{7}$$

The only two possible energy states for the spin proton are:

$$E = \begin{cases} E_{1/2} = -\dfrac{1}{2}\gamma\hbar B_0 \\ E_{-1/2} = \dfrac{1}{2}\gamma\hbar B_0\,. \end{cases} \tag{8}$$

The splitting of energy levels due to an external magnetic field is the so-called *Zeeman effect*. In the absence of $\vec{B}_0$, the two energy levels are degenerate. The two energy levels for the proton correspond to the two discrete values of I (Figure 1).

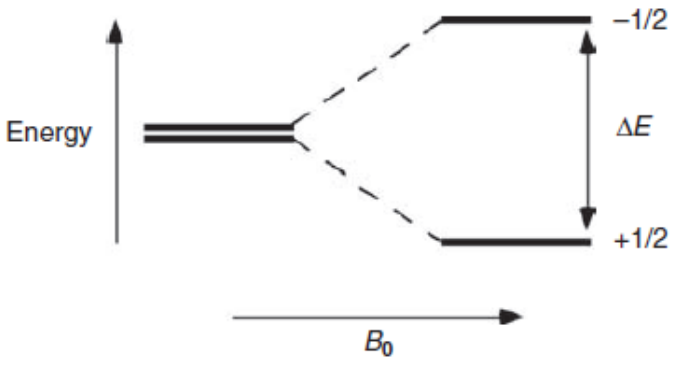

Figure 1 *The energy level diagram for a nucleus with spin quantum number I = ±1/2.*

The proton can swap between the two states simply by gaining or losing a certain amount of energy in the form of a photon. The spin-up state has less energy than the spin-down state:

$$E_{1/2} < E_{-1/2} \tag{9}$$

The lower energy level occurs when the proton magnetic moment component and the external magnetic field are parallel while, a higher energy level is obtained if they are anti-parallel. The energy separation between the levels is always $\gamma\hbar B_0$, for the proton difference in energy ΔE between these two levels is:

$$\Delta E = E_{-1/2} - E_{1/2} = \gamma\hbar B_0 = 2\mu B_0 \tag{10}$$

From the quantic point of view, not only spin angular momentum, but also the transfer of energy, may assume only discrete unit, such a transition can be caused by a photon of light whose frequency, ν, is related to the energy gap, ΔE, between the two levels according to:

$$\Delta E = h\,\nu = \hbar\omega, \tag{11}$$

where ω is called *resonance frequency* ω_R.

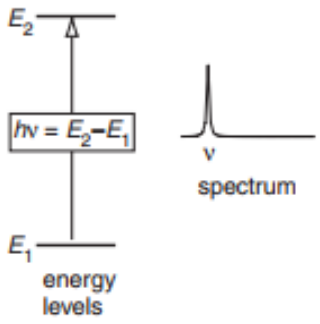

Figure 2 *A line in the spectrum is associated with a transition between two energy levels.*

Comparing the latter equation and the Zeeman equation (10) it is possible to find:

$$\omega_R = \frac{\Delta E}{\hbar} = \gamma B_0\,. \tag{12}$$

The energy required to the transition from one energy state to the other, corresponds to an electromagnetic wave with an energy ΔE and a frequency ω_R proportional to the magnetic field $\vec{B}_0$. The increasing of the magnetic field get a greater resonance frequency.

At the same time, considering the classical description, the proton spin will tend to precess around the magnetic field with a frequency traditionally called the *Larmor frequency*, $\vec{\omega}_L$.

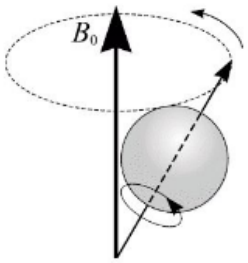

Figure 3 *Precession of a nucleus.*

When the proton interacts with the external magnetic field, $\vec{B}_0 = B_0\hat{k}$, it experiences a torque given by:

$$\vec{\tau} = \vec{\mu} \wedge \vec{B}_0 \,. \tag{13}$$

This torque acts to rotate the magnetic moment vector of a proton to align it with the external magnetic field. Using the cardinal equation of dynamics:

$$\vec{\tau} = \frac{d\vec{L}}{dt}, \tag{14}$$

and replacing (3) and (14), follow:

$$\frac{d\vec{\mu}}{dt} = \gamma\vec{\mu} \wedge \vec{B}_0 = \left(-\gamma\vec{B}_0\right) \wedge \vec{\mu} \,. \tag{15}$$

The Larmor frequency can be visualized classically in terms of the precession of the magnetic moment around the magnetic field:

$$\vec{\omega}_L = -\gamma \vec{B}_0. \tag{16}$$

The minus sign is there to make sure that $\vec{\omega}_L$ defines a clockwise rotation about the z-axis.

The resonance frequency and the Larmor frequency are the same:

$$\omega_L = \omega_R\,, \tag{17}$$

this is the principal result about the NMR phenomenon.

The link between the classical and quantum mechanical is clear, the precessional frequency of the proton in a magnetic field is the same as the frequency of radiation required to cause transitions between two states.

This is not a rigorous derivation from quantum mechanics but does show how directly the Larmor relation results from very basic concepts. The fact that Planck's constant disappears from the solution implies that a non-quantum explanation using classical physics is possible [1].

Applying a transverse RF wave at the Larmor frequency (usually in the 10 to 10^3 MHz range) nuclear spins are excited. Successively they return to the lower energy state emitting an electromagnetic wave that can be detected.

1.2 Net Magnetization and Boltzmann distribution

In a macroscopic sample there is a larger number of spins, so it is necessary to use the methods of Statistical Physics and to introduce the macroscopic magnetization. Under the hypothesis of non interacting protons, all of them add up their magnetic moment to the net magnetization $\vec{M}$.

Instead of using the individual nuclear spins, it is possible to use $\vec{M}$, which can be treated as a vector of the classical physics.

In the absence of the external magnetic field ($\vec{B}_0 = 0$) there is no preference for 'spin up' or 'spin down' states, the magnetic dipoles are oriented randomly and there is no net magnetization ($\vec{M} = 0$).

For a population of spins with I = 1/2, only the two spin states are allowed:

- $\vec{\mu}$ parallel to $\vec{B}_0$ (m = +1/2)
- $\vec{\mu}$ antiparallel to $\vec{B}_0$ (m = -1/2)

Applying an external magnetic field the magnetic moments of the nuclei can align either parallel to the field (lower energy) or antiparallel (higher energy). The two energy levels are respectively referred to "spin-up" (α) and "spin-down" (β) states.

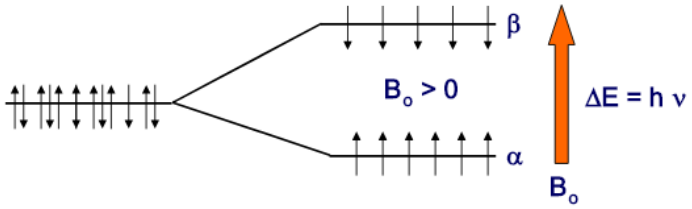

Figure 4 *Boltzmann distribution, the net magnetization M_0 is proportional to the population difference $(N_\alpha - N_\beta)$ and it is aligned exactly with the field.*

Under thermal equilibrium conditions, these two energy levels are populated according to the Boltzmann probability distribution that describes the number of nuclei in each spin state:

$$\frac{N_\beta}{N_\alpha} = e^{\Delta E/k_B T} = e^{-\mu B_0/k_B T} \tag{18}$$

where N_α and N_β represent the number of spins one would expect to respectively measure in the spin-up and spin-down configurations, ΔE is the energy separation between the two states, $k_B = 1.381 \times 10^{-23}$ J/°K is the Boltzmann constant and T is the absolute temperature in Kelvin degrees.

At room temperature, the number of spins in the lower energy level, N_α, slightly outnumbers the number in the upper level, N_β, only a small excess of spins can be expected to be found in the lower energy (spin-up) state when measurements

occurred. In presence of the main magnetic field $\vec{B}_0 = B_0\hat{k}$, the net magnetization M_0 is proportional to the population difference $(N_\alpha - N_\beta)$ and it is aligned exactly with the field (Figure 5), there is no net transverse component of M as the phase of the spins is randomly distributed.

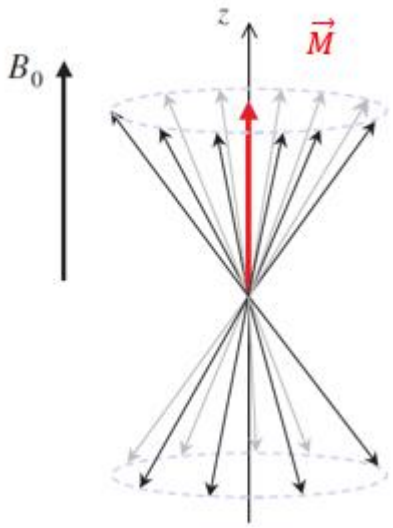

Figure 5 *The applied magnetic field causes an energy difference between aligned (α) and unaligned (β) nuclei producing the net magnetization $\vec{M}$.*

In a magnetic resonance experiment, the energy difference ΔE, between the two energy levels, is proportional to the field strength. Increasing the field strength there is an increasing of the energy difference and hence also of the population difference. Since the intensity of the NMR signal is directly dependent on the population difference, the signal also increases.

In principle to increase the spin polarization (population difference), there are two possibilities: either increase the external magnetic field or low the temperature. In practice, only the former way is exploited in NMR experiments.

For the majority of MR-experiments and for this thesis work, the proton (^{1}H) is the nucleus of interest, because of its high natural abundance (Table 2) under the form of H_2O in the biological samples. However, other nuclei such as ^{19}F, ^{13}C, ^{23}Na and ^{31}P can also use with NMR.

Isotope	Spin	Natural abundance (%)	Gyromagnetic ratio γ/2π (MHz/T)	NMR frequency in MHz		
				3.0 T	7.0 T	17.16 T
^{1}H	1/2	99.985	42.58	127.728	298.03	730.20
^{2}H	1	0.015	6.54	19.608	45.75	112.09
^{3}He	1/2	$1.4x10^{-4}$	32.43	97.302	227.04	556.24
^{7}Li	3/2	92.580	16.55	49.638	115.82	283.76
^{13}C	1/2	1.108	10.70	32.112	74.93	183.57
^{14}N	1	99.630	3.08	9.231	21.54	52.77
^{15}N	1/2	0.370	-4.32	-12.948	-30.21	-74.02
^{17}O	5/2	0.037	5.77	17.316	40.40	98.99
^{19}F	1/2	100	40.05	120.156	280.36	686.89
^{23}Na	3/2	100	11.26	33.786	78.83	193.14
^{31}P	1/2	100	17.24	51.705	120.65	295.58
^{39}K	3/2	93.10	1.99	5.964	13.92	34.10
^{129}Xe	1/2	26.44	11.78	35.331	82.44	201.98

Table 2 *summarizes the NMR characteristics of the nuclei studied in vivo (Bernstein, et al., 2004 p. 960; de Graaf, 2007 p. 9).*

1.3 Excitation and Bloch equations

In the case of independent spins, it is possible to describe their motion in terms of the precession of the spins magnetization vector. By equating the torque to the rate of change of angular momentum, follow:

$$\frac{d\vec{M}}{dt} = \gamma\vec{M} \wedge \vec{B}_0 \,. \tag{19}$$

The solution to equation (19), when B_0 is a magnetic field, corresponds to a precession of the magnetization, $\vec{M}_0 = M_0\hat{k}$, at the Larmor frequency $\omega_0 = \gamma B_0$. Remembering $\vec{B}_0 = B_0\hat{k}$:

$$\begin{aligned} \frac{dM_x}{dt} &= \gamma M_y B_0 \\ \frac{dM_y}{dt} &= -\gamma M_x B_0 \\ \frac{dM_z}{dt} &= 0 \,. \end{aligned} \tag{20}$$

follow:

$$M_x(t) = M_x(0)\cos\omega_0 t + M_y(0)\sin\omega_0 t$$

$$M_x(t) = -M_x(0)\sin\omega_0 t + M_y(0)\cos\omega_0 t \qquad (21)$$

$$M_z(t) = M_z(0).$$

To carry out an NMR experiment is necessary to apply a short burst of resonant RF field in order to disturb the spin system from the equilibrium.

Considering the circularly polarized component of a transverse time varying magnetic field $\vec{B}_1$, oscillating at ω_0, in the same sense as the spin precession, it is possible to create a resonance phenomenon.

$$\vec{B}_1(t) = B_1\cos(\omega_0 t)\,\hat{\imath} - B_1\sin(\omega_0 t)\,\hat{\jmath}\,. \qquad (22)$$

The Bloch equations become:

$$\frac{dM_x}{dt} = \gamma\left[M_y B_0 + M_z B_1\sin\omega_0 t\right]$$

$$\frac{dM_y}{dt} = \gamma[M_z B_1\cos\omega_0 t - M_x B_0] \qquad (23)$$

$$\frac{dM_z}{dt} = \gamma\left[-M_x B_1\sin\omega_0 t - M_y B_1\right].$$

Under the initial condition $\vec{M}(t) = M_0\hat{\mathrm{k}}$ the solutions are:

$$M_x(t) = M_0\sin\omega_1 t\sin\omega_0 t$$

$$M_y(t) = M_0\sin\omega_1 t\cos\omega_0 t \qquad (24)$$

$$M_z(t) = M_0\cos\omega_1 t\,,$$

where $\omega_1 = \gamma B_1$.

These equations imply that applying a rotating magnetic field of frequency ω_0, the magnetization simultaneously precess about the longitudinal polarizing B_0 at ω_0 and about B_1 at ω_1.

In the laboratory frame, the motion looks like a spiral since it is also precessing about the z-axis (Figure 6).

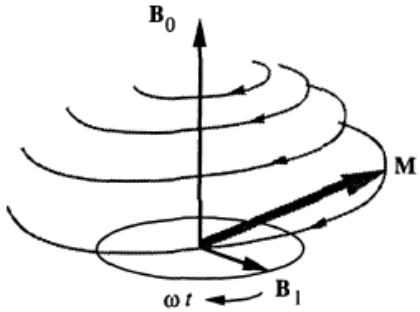

Figure 6 *Laboratory frame:Evolution of the magnetitation in the presence of B_0 and B_1* (taken from [1]).

At this point, it is helpful to make a coordinate transformation to a rotating frame (x',y',z') at the Larmor frequency about the z-axis, which is defined by the direction of B_0. In this frame, the time dependence from the RF field B is rem oved and B_1 appear stationary.

The motion of the magnetization $\vec{M}$ in the new rotating frame at ω frequency can be described by:

$$\left(\frac{d\vec{M}}{dt}\right)_{rot} = \left(\frac{d\vec{M}}{dt}\right)_{fixed} - \vec{\omega} \wedge \vec{M} \,. \tag{25}$$

Comparing this equation with the (19) it is possible to model the motion of the magnetization in the rotating frame by the same equation as in the fixed frame:

$$\left(\frac{d\vec{M}}{dt}\right)_{rot} = \gamma \vec{M} \wedge \left(\vec{B}_0 + \frac{\vec{\omega}}{\gamma}\right). \tag{26}$$

The term ω/γ represents a fictitious magnetic field due to the rotation.

The new expression define a new effective field $\vec{B}_e$, experienced by the spins:

$$\vec{B}_e = \left(\vec{B}_0 + \frac{\vec{\omega}}{\gamma}\right) \tag{27}$$

follow:

$$\left(\frac{d\vec{M}}{dt}\right)_{rot} = \gamma\vec{M} \wedge \vec{B}_e \tag{28}$$

So in the rotating frame, the magnetization precede about $\vec{B}_e$ as shown in the picture (Figure 7):

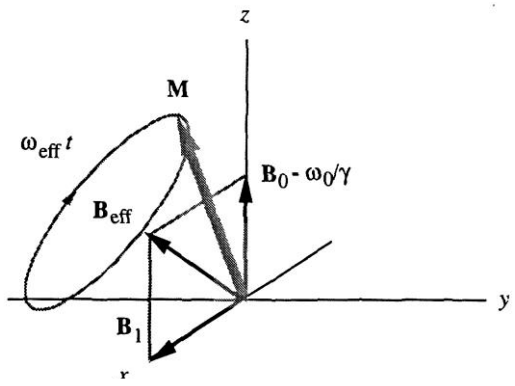

Figure 7 *Rotating frame: precession of the magnetization (taken from* [1]*).*

When the frame rotates at $\vec{\omega} = -\gamma\vec{B}_0$, the effective field becomes zero and $\vec{M}$ is a fixed vector in the rotating frame.

In the real systems the spins interaction have to be take into account.

1.4 Relaxation

When the RF pulse, used to excite the spin system, is over the system tends to recover its original repose state, there must subsequently be a process to restore the equilibrium. This involves the exchange of energy between the spin system and respectively its surroundings and among themselves. Both relaxations occur at the same time.

In the first case, the recovering of M_0 to equilibrium means the restoration of the state of polarization where M_0 is directed along the longitudinal magnetic field B_0, this is the reason because of the process is alternatively named longitudinal relaxation. The phenomenological description of this process is defined in a new equation of motion for M_z:

$$\frac{dM_z}{dt} = \frac{-(M_z - M_0)}{T_1} \tag{29}$$

where T_1 is known as the *spin-lattice* or *longitudinal relaxation time* and the solution of the (29) is:

$$M_z(t) = (0)e^{-t/T_1} + M_0\left(1 - e^{-t/T_1}\right). \tag{30}$$

The process is known as *spin-lattice* relaxation.

In the second case the process that bring about the nuclear spins to thermal equilibrium among themselves is known as spin-spin relaxation and the time constant involves is called T_2 *spin-spin relaxation time* or *transverse relaxation time* (see section 1.4.1).

This phenomenon has a decreasing exponential behaviour described by the equations describing the evolution of M_x and M_y:

$$\frac{dM_{x,y}}{dt} = \frac{-M_{x,y}}{T_2} \tag{33}$$

where the solutions are:

$$M_{x,y}(t) = M_{x,y}(0)e^{-t/T_2}. \tag{34}$$

Transverse magnetization corresponds to a state of phase coherence between the nuclear spin states. This means that transverse relaxation is sensitive to interaction terms which cause the nuclear spins to dephase [1].

If the system was initially in equilibrium and RF pulse was a 90° pulse applied along x'-axis:

$$M_x(0) = M_z(0) = 0 \;\; ; \;\; M_y(0) = M_0, \tag{31}$$

and

$$M_z(t) = M_0\left(1 - e^{-t/T_1}\right). \tag{32}$$

Mx and My oscillate at the Larmor frequency while decaying with time constant

T_2, while the z magnetization simply grows from zero back to M_0.
In the rotating frame the Bloch equations become:

$$\frac{dM_x}{dt} = \gamma\left[M_y B_0 + M_z B_1 \sin\omega_0 t\right] - \frac{M_x}{T_2}$$

$$\frac{dM_y}{dt} = \gamma\left[M_z B_1 \cos\omega_0 t - M_x B_0\right] - \frac{M_y}{T_2} \qquad (35)$$

$$\frac{dM_z}{dt} = \gamma\left[-M_x B_1 \sin\omega_0 t - M_y B_1\right] - \frac{(M_z - M_0)}{T_1}.$$

These set of differential equations describe the changes in the magnetization during excitation and relaxation and describe completely the main phenomena in NMR imaging using classical mechanics [1].

1.4.1 Spin-lattice and spin-spin relaxation

Spin-lattice relaxation

As mentioned before, the exchange of energy between the spin system and its surroundings is the so called spin-lattice relaxation. Since the magnetic field is applied to the sample until the thermal equilibrium is reached, the macroscopic magnetization experiments grow exponentially.

As spins go from a high energy state back to a low energy state, RF energy is released back into the surrounding lattice. The rate at which equilibrium is restored is characterized by the longitudinal relaxation time, T_1. The recovery of longitudinal magnetization follows an exponential curve (Figure 8).

The recovery rate is characterized by time constant T_1 that represents the time needed to recover the 63% of the longitudinal magnetization M_z.

It depends on the structure and molecular composition, the material state, viscosity and magnetic interactions. It has a lower value in solid than in a liquid state.

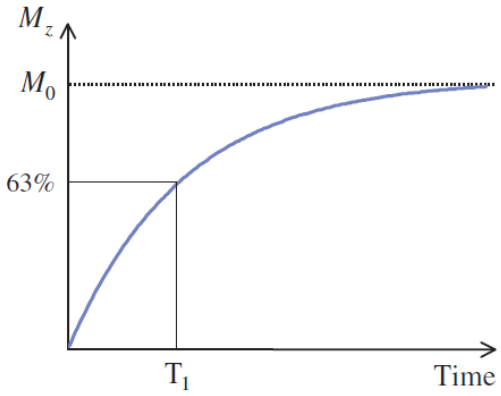

Figure 8 *Spin- lattice relaxation (taken from* [2]*).*

Spin-spin relaxation

The spin-spin relaxation is in general a faster process than spin-lattice relaxation and it is characterized by the spin-spin or transverse relaxation time, T_2. Transverse magnetization decay is described by an exponential curve characterized by the time constant T_2 (Figure 9). Protons are influenced by non-uniform, low magnetic fields produced by the near nuclei, which cause different speed precession. When the RF stops, the proton suffers a phase difference, M_{xy} decreases and tend to zero. After time T_2, transverse magnetization has reduce its intensity of 37% of its original value. In the spin-spin interaction, the relaxation time T_2 is independent of field strength.

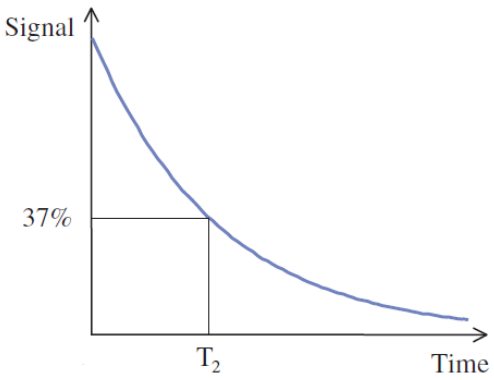

Figure 9 *Spin- spin relaxation (taken from* [2]*).*

Since the longitudinal magnetization cannot be restored, if the transverse magnetization does not disappear, T_2 is always shorter than T_1 (Figure 10). The relation between the two time constants is:

$$T_2 \leq T_1. \tag{36}$$

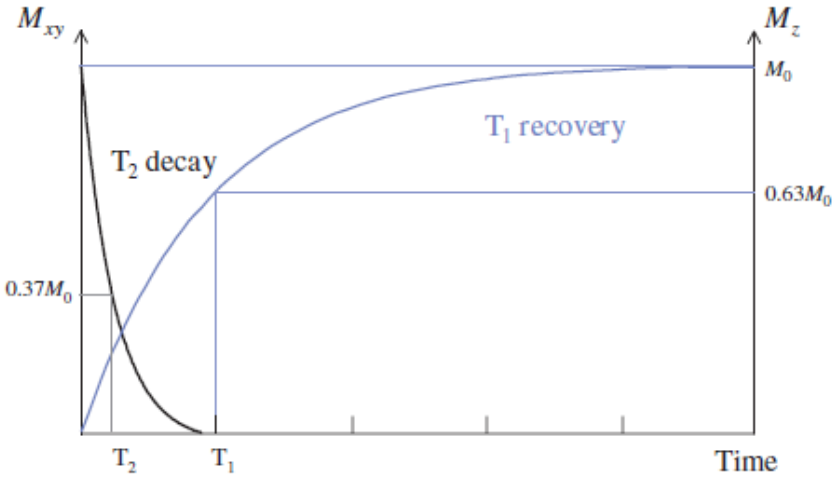

Figure 10 *T_1 and T_2 relaxation occur simultaneously, the T_2 decay is much quicker than the T_1 recover (taken from* [2]*).*

In the hypothesis of interacting spins, the decay of the transverse magnetization is caused by the combination of two factors. It is necessary to take into account that in the M_{xy} decay the time constant T_2 due to the molecular interactions is not the only contribution but also the inhomogeneity due to B_0 variations are characterized by a time constant, T_2'.

The combination of these two factor gives the effective time constant of M_{xy} decay called T_2^* following the relation:

$$\frac{1}{T_2^*} = \frac{1}{T_2} + \frac{1}{T_2'}. \tag{37}$$

1.5 Signal detection

The equilibrium is characterized by a state of polarization with M_0 directed along the longitudinal magnetic field B_0. M_0 is a measurable magnetization of the order of microtesla (μT), but smaller than the main magnetic field (T) so its detection results really difficult.

M_0 becomes a significant signal, easier to record, simply tipping it in the transverse plane (x-y) and detecting the induced voltage using a receiver coil which measures the magnetic fields only in this plane. To rotate the magnetization a 90° RF pulse is applied, this pulse tips M_0 vector from the longitudinal plane (parallel to B_0) to the transverse plane (perpendicular to B_0) where it can be detected.

The semi-classical magnetization approach again gives a complete explanation of the process. The RF pulse creates a magnetic field within the transmit coil which is perpendicular to B_0 and oscillating at the Larmor frequency (to respect the resonance conditions).

In the rotating frame, this is the static field B_1 aligned along x' in the transverse plane (Figure 11 a). M_0 moves away from the z-axis until the RF pulse is switched off (Figure 11 b). As seen in the previous section (Figure 6) the motion looks like a spiral since it is also precessing about the z-axis.

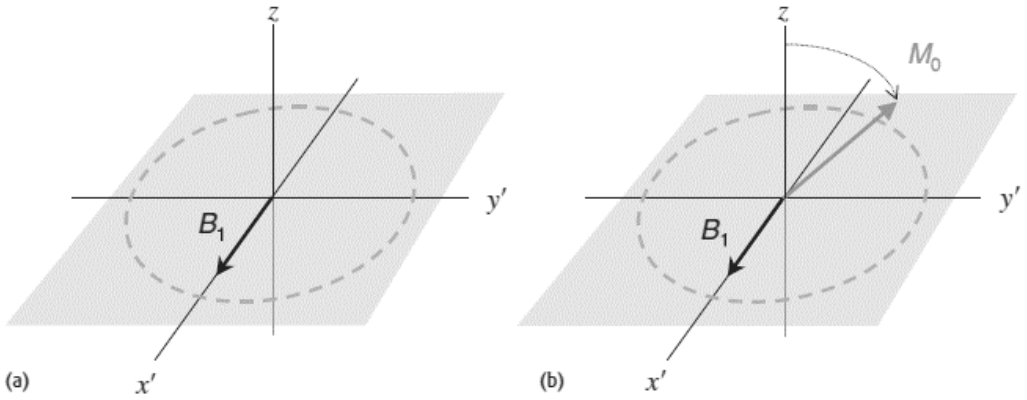

Figure 11 *(a) The RF pulse produces a fixed magnetic field B_1 in the rotating frame. (b) M_0 precess about B_1 until the RF is switched off (taken from* [2]*).*

The RF pulse brings the spins into phase coherence consequently, M_0 induce a voltage in the receiver coil into the x-y plane, the coil is sensitive only to

magnetization perpendicular to B_0. In the laboratory frame, M_0 is now precessing in the transverse plane (Figure 12 a), so the coil sees an oscillating magnetic field which induces a voltage varying at the Larmor frequency.

Since the protons rapidly dephase with respect to each other the amplitude of the signal decays exponentially to zero in only a few milliseconds (Figure 12 b). The free precession of magnetization induces a decaying signal known as *Free Induction Decay* (FID) that is measured in the time domain and represent the primary NMR signal.

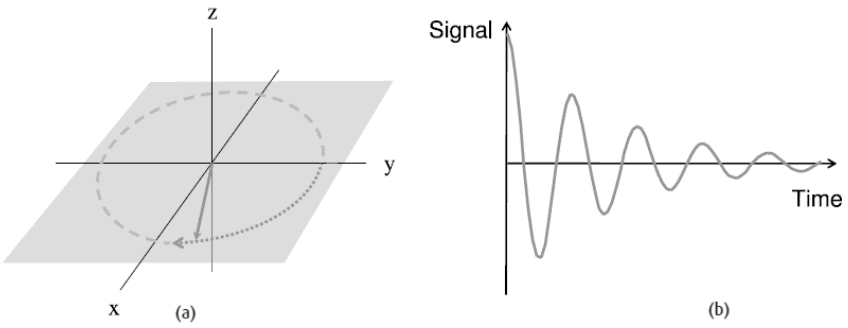

Figure 12 *(a) Precession on the flipped magnetization in the transverse plane. (b) FID- Signal induced in the receiver coil (taken from* [2]*).*

It is possible to represent this signal in the frequency domain through the Fourier transformations.

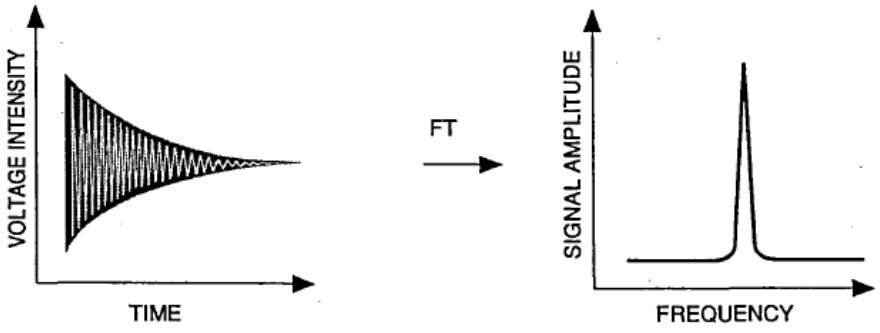

Figure 13 *The FT process takes the time domain function (the FID) and converts it into a frequency domain function (the spectrum).*

Once all these signals are collected, the application of a Fourier transform converts the spatial frequency distribution into a spatial distribution of the excited nuclei.

The FID is never directly measured in a MRI experiments, what happens is described in the next chapter where the MRI principles will be described in detail.

2. Imaging by Nuclear Magnetic Resonance

The strength of the magnetic resonance imaging is to exploit linearly varying magnetic fields to enhance a spatial dependence.

Over the static field B_0, that points in the longitudinal direction and the transverse RF field B_1 produced by coils tuned to the Larmor frequency, in MR imaging there are three additional fields that vary spatially, the so called gradients.

The local frequency will vary with position by the linear relation between the Larmor frequency and the nuclear spin coordinates $\vec{r}$, following the relation:

$$\omega(\vec{r}) = \gamma(B_0 + \vec{G} \cdot \vec{r}\,)\,, \tag{38}$$

where $\vec{G}$ is defined in the usual manner as the grad of pulsed gradient field component parallel to $\vec{B}_0$. This equation describes the frequency precession in presence of a gradient field. The first term comes from the static magnetic field but because of the presence of the gradient field, there is an additional term which adds another element to the Larmor equation that depends on the position.

This simple relation between the Larmor frequency and the nuclear spin coordinates $\vec{r}$ in the sample, lies the fundamental of the imaging principle; the resonance frequency of the magnetization will vary in proportion to the gradient field and this change in frequency can be used for spatial encoding.

2.1 Spatial encoding

Spatial encoding consist on successively applying magnetic field gradients.

The magnetization precessing close to the resonance frequency is affected by the RF field whereas the pulse does not affect magnetization at distant frequencies. The RF pulse includes a set of frequencies centered on the Larmor frequency; this range of frequencies constitutes the RF *bandwidth*, Δf, (expressed in Hertz).

In absence of the gradient fields, all the spins experience the same field B_0 and have the same frequency; the application of a gradient causes a protons frequency variation as a function of position along the direction of the gradient.

When a gradient is added for example, on the x direction, the resonance frequency varies with position and the magnetic field produced adds to the main field B_0. Along the x-direction, the MR signal shows higher or lower frequencies, which means that protons can resonate faster or slower depending on their precession position. In this way frequency measurements may be used to distinguish between MR signals at different positions in the space.

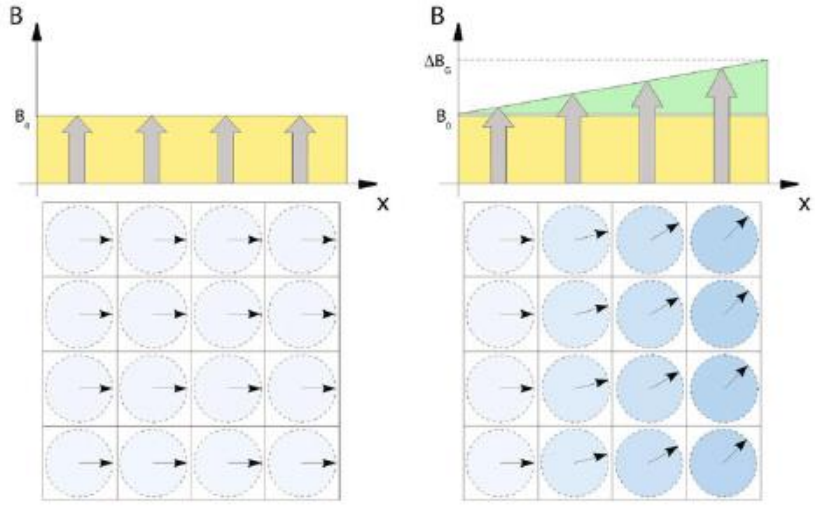

Figure 14 *All the spins experience the same field and have the same frequency. When the gradient is added moving along the x direction these protons resonate faster or slower depending upon their position. (Taken from* [3].

The sets of gradients give MR its three dimensional capability. Firstly, a slice selection gradient (G_s) is used to select the volume of interest. Within this volume,

the position of each point will be encoded vertically and horizontally by respectively applying a phase encoding gradient (G_Φ) and a frequency encoding gradient (G_f). Magnetic field gradients form the basis of MR signal localization.

Slice selection

Through the selection gradient G_s ,applied in the z-direction, a selective excitation of slice in the x-y plane is possible. The slice selection process is achieved by applying the RF pulse to tip the spins at the same time as the gradient.

The resonance frequency of the spins during the application of the z gradient becomes:

$$\omega(z) = \gamma(B_0 + G_z z\ ). \tag{39}$$

The RF excitation pulse contains a narrow range of frequencies centered about the Larmor frequency; at isocentre of the gradient (z = 0) where the effect of the gradient is zero, the frequency is: $\omega = \gamma B_0$.

Modulating the RF envelope with a predetermined shape, for example a SINC shaped envelope pulse, a selective RF pulse is generated (Figure 15).

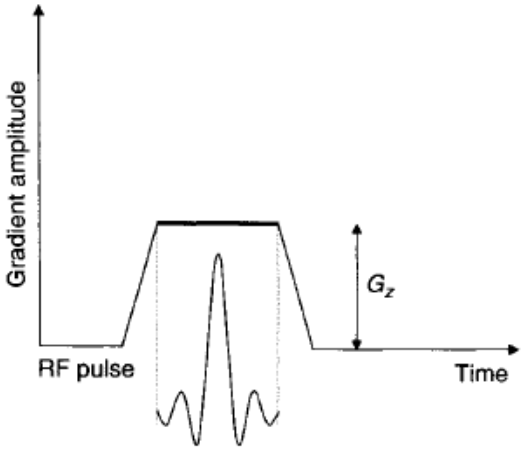

Figure 15 *Slice selection gradient Gz (taken from* [4]*).*

The excitation will take place only if the required frequency is present within the RF pulse's transmit bandwidth (or close to the isocentre) otherwise the resonance does not happen and no MR signal is produced.

For extreme points along the gradient axis, in fact, the frequency required for resonance will not be present within the RF pulse bandwidth so no signal will be produced from these points. Only one slice remains selected. The slice-selection gradient translate the desired band of frequencies into the desired band of locations, corresponding to the slice [4].

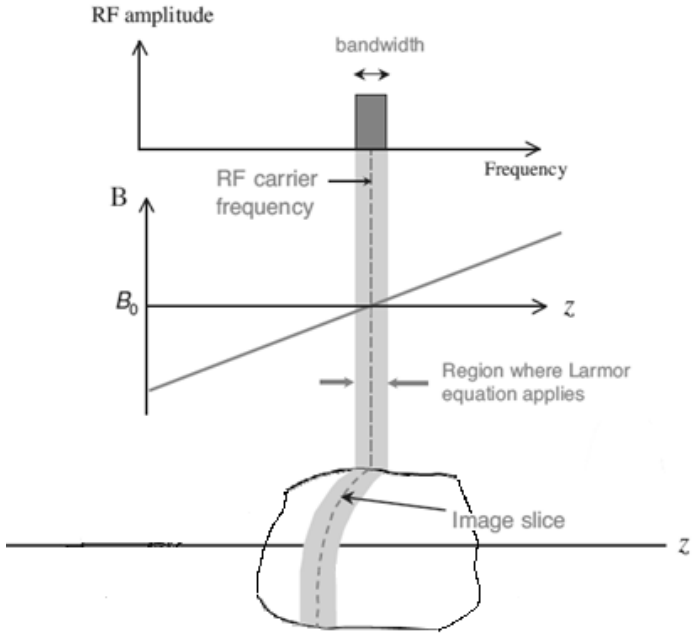

Figure 16 *Selective excitation of an image slice by applying a shaped RF pulse and a field gradient at the same time.*

The amplitude of slice selection gradient G_z and RF pulse bandwidth determine the slice thickness. For a fixed RF bandwidth Δf, the increasing of the amplitude of the gradient correspond to a decreasing of the thickness of the slice.

As shown in the Figure 17, the slope of each of the two lines represents the strength of a slice selection gradient ($G_{z,1}$ and $G_{z,2}$). For a given Δf of the RF pulse, the stronger gradient produces a thinner slice.

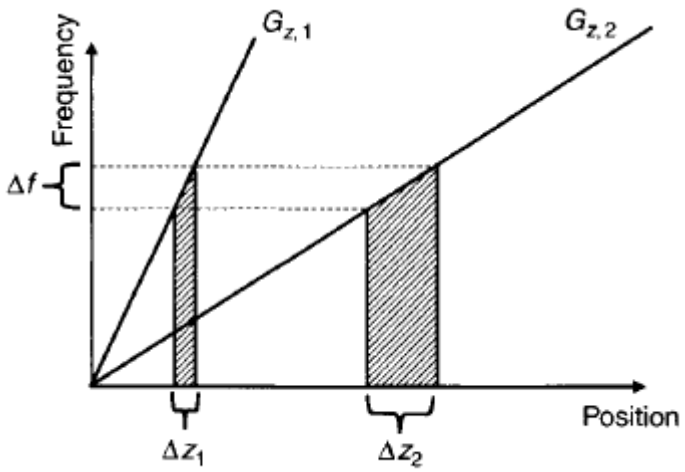

Figure 17 *Larmor frequency versus position along the gradient direction , z-axis (taken from* [4]*).*

By applying the selective gradient and changing the central frequency of the RF pulse it is possible to move the position of the slice. In this way it is possible to make multi-slices acquisitions.

The slice-select gradient is applied simultaneously to the RF pulse and it will not be on during the readout.

Phase encoding

The idea behind phase encoding is to create a linear spatial variation of the phase of the magnetization (the phase is the angle made by the transverse magnetization vector with respect to some fixed axis in the transverse plane). The phase encoding gradient, G_{Φ}, is applied on the y-direction. It modifies the spin resonance frequencies, inducing dephasing, which persists after the gradient is interrupted. This means that all the protons precess in the same frequency but in different phases: this phase difference lasts until the signal is recorded. The protons in the same row, perpendicular to the gradient direction, will all have the same phase (Figure 18).

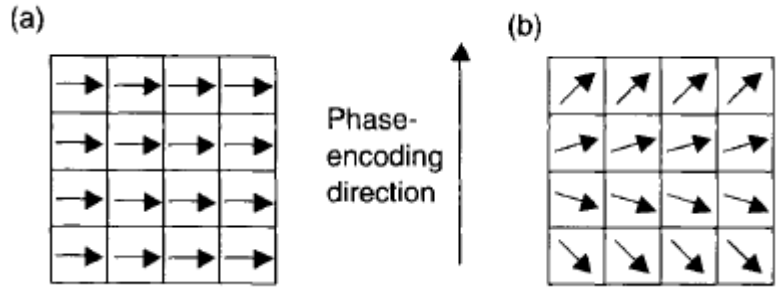

Figure 18 *Phase encoding. The arrows represent transverse magnetization at the center of each pixel.*

At the end of the RF excitation pulse, the transverse magnetization has the same phase (direction) in each pixel (Figure 18 a). After a phase-encoding gradient is applied, the phase of the transverse magnetization varies at each location along the phase-encoded direction (Figure 18 b).

In principle, during the gradient pulse spins at different y locations precess at different frequencies, the spins precession will speed up or slow down according to their position along the y-axis. This causes the spins to dephase to a progressively greater degree as long as the gradient is applied, the relative phase shift is linear with y.

When the gradient is interrupted, all the spins come back to their original frequency, but keep their different phase angles, so they are *phase encoded*: in this way they can be localized on y-axis.

All of them precess in the same frequency but in different phases. This phase difference lasts until the signal is recorded. The MR signal is sampled after the gradient is turned off, so during the sampling there is no spread of frequencies due to the gradient; all the spins are precessing at $\omega_0 = \gamma B_0$.

The MR sequence consists of multiple repetitions of the excitation process followed by a different phase encode gradient until all possible spatial frequencies are interrogated, a RF pulse is required for every line of data. This is the reason because of in a pulse sequence diagrams the phase-encode steps are represented by a series of parallel lines (Figure 19).

Frequency encoding

Frequency-encoding of spatial position is accomplished through the use of a third magnetic field gradient, G_F. Applying the frequency encoding gradient, the Larmor frequency in the horizontal direction is modified becoming a function of the position and the x direction results encoded. It thus creates proton columns, which all have an identical Larmor frequency. The frequency encoding gradient is turn on during the readout, this is the reason because of such time it is known also as *read gradient*.

Firstly the slice selection take place applying the RF pulse simultasionely with the slice-selective gradient. After that, the phase encoding is on for a short amount of time and then it is turned off. Finally the frequency encoding is turn on during the readout of the signal (Figure 19).

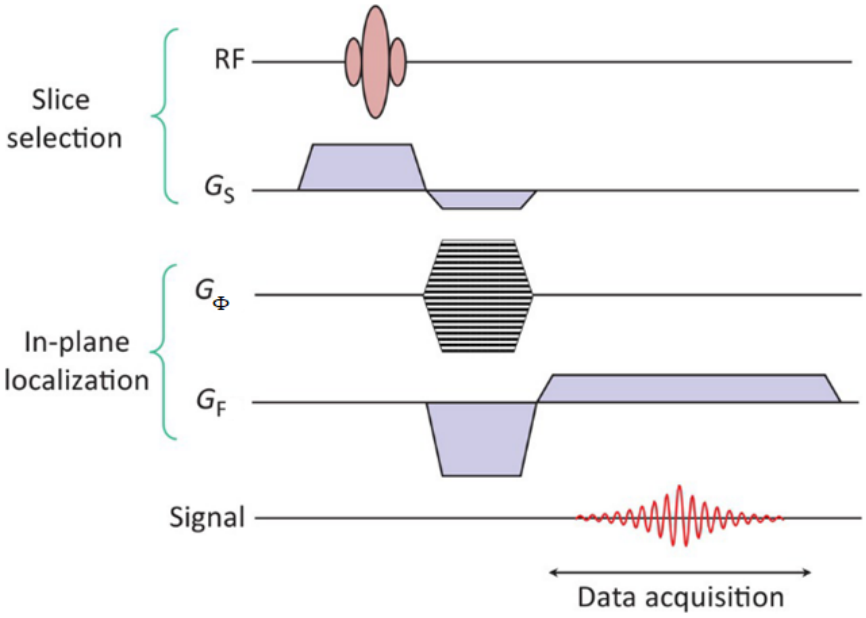

Figure 19 *NMR pulse sequence diagram. In a sequence diagram it is common to find a negative lobe to correct the phase dispersion of transverse magnetization that occurs concomitant with application of the main G_z gradient (taken from* [2]*).*

The signal is stored in a matrix known as *k-space*, trough the Fourier transform it the image in the real space is obtained.

2.1.1 Readout signal and k-space

The readout MR signal is the combination of plenty RF waves characterized by different amplitudes, frequencies and phases, containing spatial information.

The spatial encoded raw data are arranged into an array of numbers representing spatial frequencies in the MR image. This is a matrix of frequencies (k_x,k_y), the so called *k-space*.

The *k*-space is commonly displayed like a rectangular grid where the axes, k_x and k_y, represent spatial frequencies respectively in the x and y directions rather than positions.

Each *k*-space point contains spatial frequency and phase information about every pixel in the final image. Conversely, each pixel in the image maps every point in *k*-space.

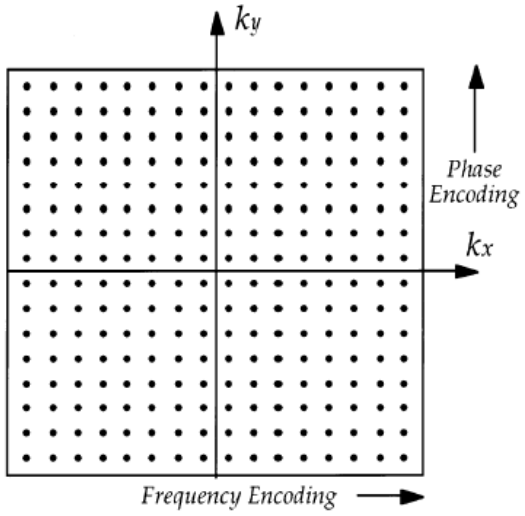

Figure 20 *Representation of k-space. It is a grid of raw data of the form (kx,ky) obtained directly from the MR signal.*

The k-space grid is filled by frequency and phase encoded with magnetic gradient fields. During frequency encoding, gradient amplitude is constant and different data are acquired along k_x at different times of echo sampling. During the phase encoding, gradient amplitude is varied from line to the next and the gradient

duration time is constant. Each k_y line represent the point that are collected for a given amplitude of the phase encoding gradient [5].
Data near the centre of *k*-space corresponds to low spatial frequencies, whereas data from the periphery relates to high-spatial frequencies, different parts of the k-space influence the apparence of MR images: line around the centre determine the contrast of image while the outer lines of the raw data matrix provide information on image spatial resolution.
The individual points (k_x,k_y) in k-space do not correspond one-to-one with individual pixels (x, y) in the image, but they may be converted to one another using the FT. To go from a k-space data to an image a 2D inverse FT is required.

2.2 Image contrast

Depending on what it is necessary to visualize in an MR image, it is needed to enhance a type of contrast. The Proton Density (PD), the spin-lattice relaxation time (T_1) and the spin-spin relaxation time (T_2) are intrinsic properties of the samples; in general, images have contrast that depends on one of these parameters. The contrast of MR image can be manipulated by varying several parameters among which the main ones the *Repetition Time* (TR) and the *Echo Time* (TE).

- TR is the length of time between corresponding consecutive points on a repeating series of pulses and echoes. It determines how much longitudinal magnetization recovers between each pulse.

- TE refers to the time between the application of the radiofrequency excitation pulse and the peak of the signal induced in the coil. TE controls the amount of T_2 relaxation.

The manipulation of these parameters permits to obtain images where contrast depends on the time constants T_1 or T_2 (that describe how long the magnetization

takes to get back to equilibrium after an RF pulse) or on proton density (it is related to the number of hydrogen atoms in a particular volume).

The TR dominates *T_1-weighted images*, in these type of images, a short TE and a short TR are required. The intensity of the image pixels is proportional to the protons concentration and it depends on the spin-lattice relaxation time of the sample. In presence of a long T_1, the magnetization will take longer to recover back to the equilibrium. This means that a short TR will make dark pixels compared to pixels associated with short T_1, like fat, which appears brighter. Bright pixels on T_1 are associated with short T_1 values. Water is characterized by a long T_1 giving a weak signal.

In *T_2-weighted images*, water give the highest signal intensities, producing a bright appearance, because of its long T_2.
The intensity of the image pixels is proportional to the protons concentration and it depends on the spin-spin relaxation time of the sample.
The magnetization will take longer to decay and the signal will be grater, so it will appear brighter in the image than the signal from tissue with a short T_2 (like fat). In these type of images, a short TE and a short TR are required. These images are dominated by TE.

In *PD weighted images* high PDs give high signal intensities which in turn have bright pixels on the image. The signal contrast is derived from the density of spins in a given volume because the intensity of the image pixels is proportional to the protons concentration in a voxel. In these type of images, a short TE and a long TR are chosen to minimize both weightings.
To sum up (Figure 21), sequences with:

- Long TR and short TE return PD weighted images
- Short TR and short TE return T_1 weighted images
- Long TR and long TE return T_2 weighted images

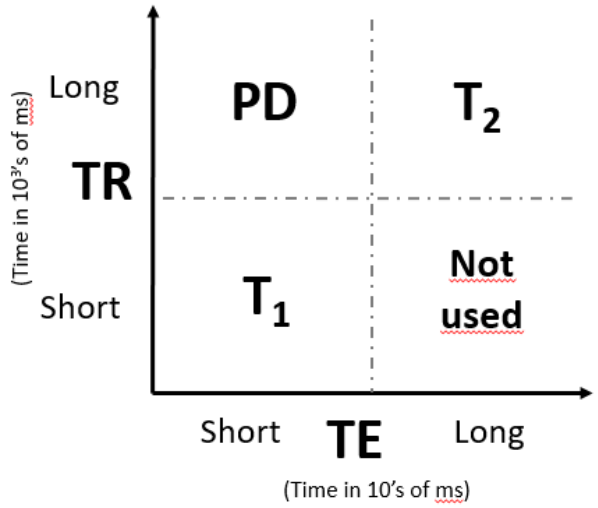

Figure 21 *Contrast dependence on TR and TE*

Maps

It is possible to obtain *maps*, in which each pixel contains information not about the intensity of the signal, but about relaxation time either T_1 or T_2. These maps can be obtained by acquiring series of MR images with different levels of T_1 or T_2 weighting and performing nonlinear regression on the signal (see section 5.5).

In conclusion, starting from an image the extrapolation of the relaxation times and the consequently interpretation of them is a great approach to interpreting MRI images and to attributing physiological meaning to them.

2.3 Sequences

The basic concept of MRI is the magnetic field inhomogeneity that induce spins precess at differing Larmor frequencies according to their location in the sample.

All MR images are produced using pulse sequences [4]. The architecture of a sequence consists of radiofrequency pulses and gradient pulses which have carefully controlled durations and timings. There are many different types of sequences, but they all have the timing values TR and TE, which can be modified.

Spin echo (SE) pulse sequence is one of the earliest developed and still widely used of all MRI pulse sequences, it is also known as a *Hahn echo*. The pulse sequence timing can be adjusted to give T_1, PD or T_2-weighted images. Dual echo and multi-echo sequences can be used to obtain both PD and T_2-weighted images simultaneously.

From this point (x,y,z) notation it is referred to the rotating frame.

2.3.1 Spin echo

The SE sequence consists of a 90° applied on the x-axis pulse after which the spins dephase naturally for a certain time. Then a 180° pulse is applied on the y-axis causing the flips of all the spins of an angle of 180° [6].

Following the 90° pulse, spins in a region of relatively high magnetic field precess faster, while those in a region of relatively low magnetic field precess slower.

After a certain time *t*, the phases of the spins across all these regions are sufficiently different to degrade the overall magnetization.

The application of the 180° pulse has the effect of reflecting the spins in the direction of the applied pulse. The spins continue to precess, but their relative motion is now precisely reversed. This means that the 180° pulse does not change the precessional frequencies of the spins, but it does reverse their phase angles.

After a time equal to the delay between the 90° and the 180° pulse, those regions which were precessing faster and accumulated more phase difference undo their phase accumulation at a faster rate.

The result is that all the spins are back in phase and the total magnetization reaches a maximum, producing the echo.

The 180° RF pulse is applied at time TE/2, TE being the time between the center of the first RF pulse and the peak of the spin echo. The sequence is repeated at each time interval TR (Figure 22).

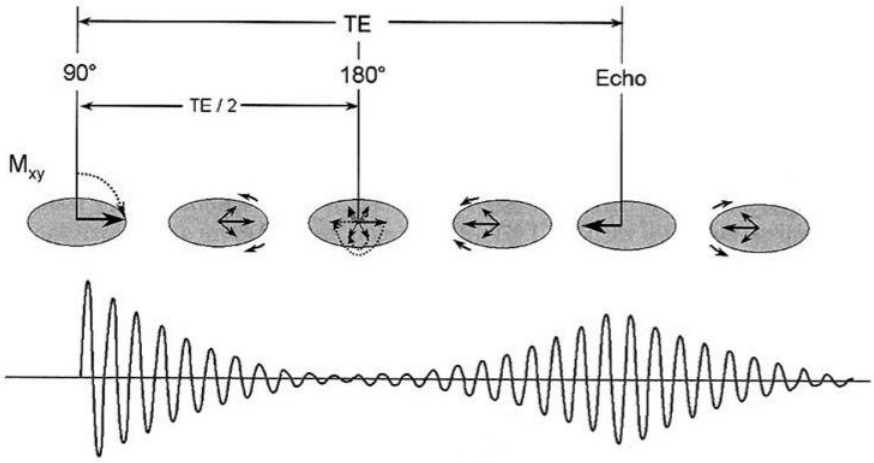

Figure 22 *Spin echo diagram in the rotating frame (taken from Medical Radiation Resources).*

The phase-reversal implies that the echo height will only depend on T_2 and not on the magnetic field inhomogeneities (no dependence from T_2*) or on tissue susceptibilities. The spin echo signal is given by:

$$S_{SE} = S_0 exp\left(-\frac{TE}{T_2}\right). \tag{40}$$

2.3.2 Sequences based on the spin echo

The main sequences are based on the SE. A variation on the spin echo sequence is the so called *inversion recovery* (IR) which has an extra 180° RF before the 90° pulse. An IR pulse sequence is a spin echo pulse sequence preceded by a 180° RF pulse. This pre-pulse flips the longitudinal magnetization to its negative value. The time elapsed between the preparatory 180° pulse and the 90° readout pulse is termed *time to inversion* (TI) separated a timing parameter, specific of this sequence.

IR is often used to make signal 'suppression', since, tissues regain M_z at different longitudinal relaxation rates determined by their T_1 relaxation times. By selecting the TI carefully the signal from any particular tissue can be nulled. The spin echo

90° readout pulse is applied at the exact time when longitudinal magnetization reaches the null point for the signal that is necessary to suppress. If a 90° excitation and two 180° refocusing pulses are used it is the so called *double spin-echo* method [7].

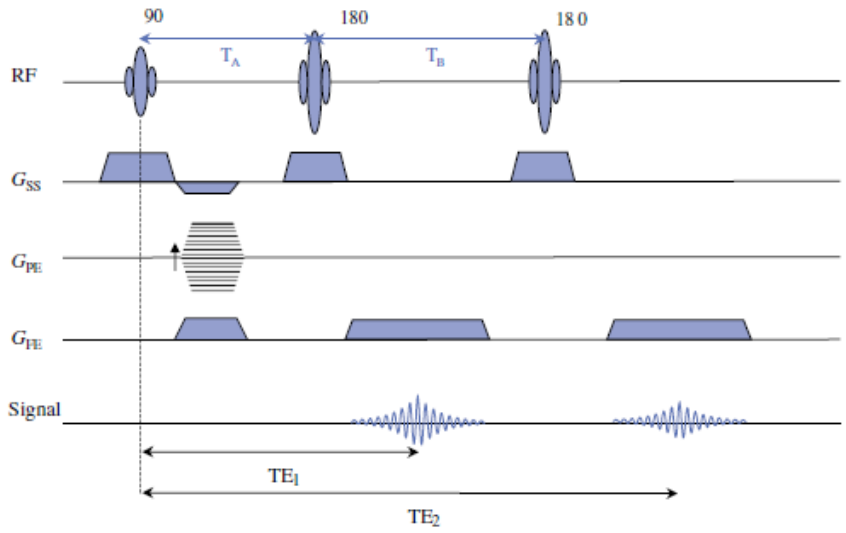

Figure 23 *Double spin echo pulse sequence (taken from* [2]*).*

When after the 90° pulse an echo train by successive 180° is induced, a new sequence is obtained, the so called *Carr–Purcell–Meiboom–Gill* (CPMG).
The initial 90° pulse is on the x-axis and the train of 180° pulses is on the y-axis and all the echoes are positive. On the CMPG is based the sequence widely used in this work the *Multi Slices Multi Echo* (MSME).

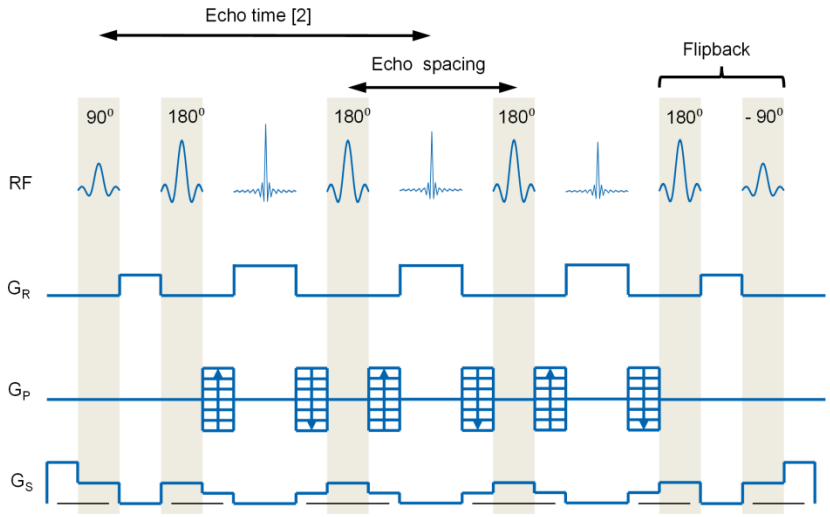

Figure 24 *Pulse sequence of MSME (taken from Bruker manual).*

RARE (Rapid Acquisition with Refocused Echoes) sequence is based on multiple-echo sequence filling more than one k-space trajectory in a single excitation this is the reason because of it is also named Fast Spin Echo (*FSE*) or Rapid Spin Echo (*RSE*).

Multiple spin echoes are generated using the CPMG sequence with slice selective RF pulses. Each echo is separately phase-encoded, and the phase encoding is incremented within one echo train to accelerate the acquisition. It is possible to obtain two or more echo-images with different effective TEs. The sequence scheme is the same of the MSME (Figure 24).

ZTE (Zero echo time) sequence is based on a non-selective excitation and a signal acquisition in the presence of a constant gradient, a particular features is zero echo time. ZTE is a radial acquisition method, performing center-out readouts.

2.3.3 Gradient echo

In the gradient echo sequence, the angle used to flip the magnetization in the x-y plane is smaller than 90°. The sequence used in this work is the Fast Low Angle SHot (FLASH).

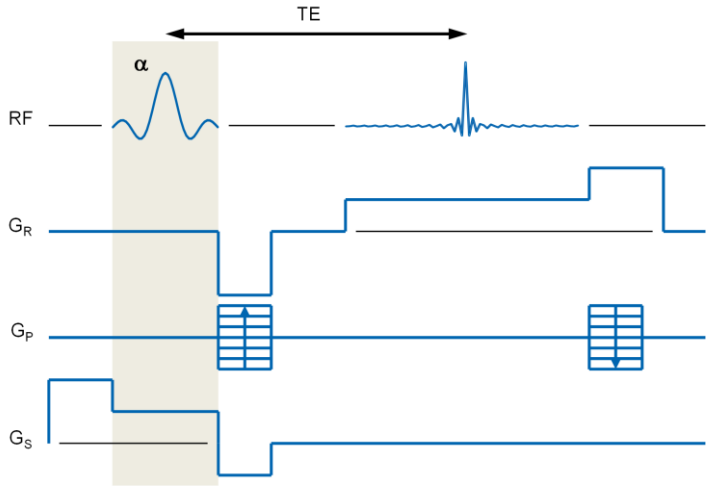

Figure 25 *Pulse sequence of FLASH (taken from Bruker manual).*

A negative gradient lobe is applied after the RF pulse causing a rapid dephasing of the transverse magnetization M_{xy}, faster than FID that is acquired in a spin-echo. To rephasing spins, immediately after the negative lobe a positive gradient is applied. Spins that were precessing at a low frequency due to their position in the gradient will now precess at a higher frequency because the gradient will now add to the main field, and vice versa. After a certain time spins will all come back into phase along the y-axis forming the gradient echo.

A crucial point is that the positive gradient can compensates only the dephasing caused by the negative gradient lobe, it can't refocus dephasing due to the main magnetic field inhomogeneities or spin-spin relaxation how happens in the spin echo sequences.

If S0 indicate the initial height of the FID, the height of the echo is thus determined by the FID decay curve which depends on T_2*:

$$S_{GE} = S_0 exp\left(\frac{TE}{T_2^*}\right). \tag{41}$$

Remembering that T_2* is a composite relaxation time which includes T_2, inhomogeneities due to the main field and tissue susceptibility, and diffusion of the protons (see section 1.4.1). In this case images acquired using a gradient echo are T_2* weighted. Of course playing with the flip angle and the TR, it is possible

acquire gradient echo images T1 weighted or PD weighted for more details look at [2].

2.4 Single Voxel Spectroscopy

The single voxel spectroscopy (SVS) is one of the two method through which it is possible to perform the Magnetic Resonance Spectroscopy (MRS); the second method is the multi-voxel spectroscopy.

In the SVS the signal comes from a volume limited to a single voxel, the volume of interest (VOI) is selected and a spectrum obtained from it, whereas in the multi-voxel MRS spectra are obtained from multiple voxels in a single slice of sample.

In this work the MRI technique has been supplied by the SVS as it will be show in the chapters 5 and 6.

The two sequence most widely used in MRS are the PRESS (Point-RESolved Spectroscopy) and the STEAM (STimulated Echo Acquisition Mode). PRESS sequence results really useful for the purposes of this thesis, the acquisition is fairly fast (1 to 3 minutes) and the spectrum is easily obtained, it is the dominant method for ^{1}H spectroscopy used for single and multi-voxel studies.

The sequence is based on the double spin-echo; the RF pulses have flip angles of 90°-180°-180° so the signal emitted by the voxel of interest is thus a spin echo.

It works identically as in MR imaging but the signal is sampled without the read out gradient (see section 2.1: Frequency encoding) since the frequency differences are used to constitute the spectrum and not the position. The 90° pulse is followed by two 180° pulses so that the primary spin echo is refocused again by the third pulse. Each pulse has a slice-selective gradient on one of the three principle axes and the protons within the voxel are the only ones to experience all three RF pulses.

So using a combination of magnetic field gradients and frequency-selective 180° pulses, a three-dimensional voxel of well-defined position and size is selected and its spectrum is then collected and analyzed.

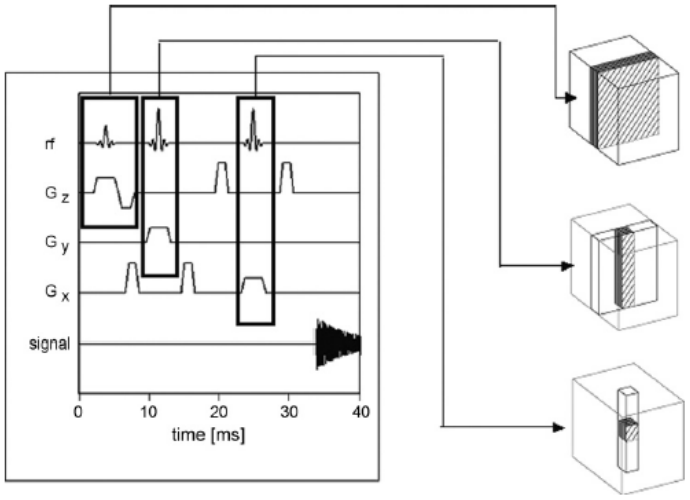

Figure 26 *Selection of a cube with a PRESS sequence. The three RF pulses within the sequence are marked and the selected regions after each pulse are shown for an cubic object* [7]**.**

All the sequences described in this section have been used for the aim of this work. These and many others are implemented in the software package of the Bruker spectrometer used for the experiments. This latest generation instrument make available various acquisition and processing tools and broad spectrum of applications. The experimental setup used to perform the analysis will be describe deeply in the next chapter.

3. Experimental Setup

MRI technique has been performed with a Bruker NMR Spectrometer 300 MHz/89 mm ASCEND^{TM} . The spectrometer consists of the following subunits:

• Operator console including the host computer, monitor and the keyboard

• Console containing the electronic hardware

• Magnet system including the shim system and the probe.

Figure 27 *Magnet, Operator Console, and Console at MNR Laboratory of Physics Department of Salerno.*

Magnet

The main component of the MR system is the magnet, which generates the magnetic field required to induce NMR transitions.

The Bruker Ascend magnet design features advanced superconductor technology, enabling the design of smaller magnet coils, thus resulting in a significant reduction in physical size and magnetic stray fields [Bruker User Guide].

The Exclusion Zone (the area inside the magnet's 5 Gauss field line) is completely confined inside the instrument, as shown below in Figure 28.

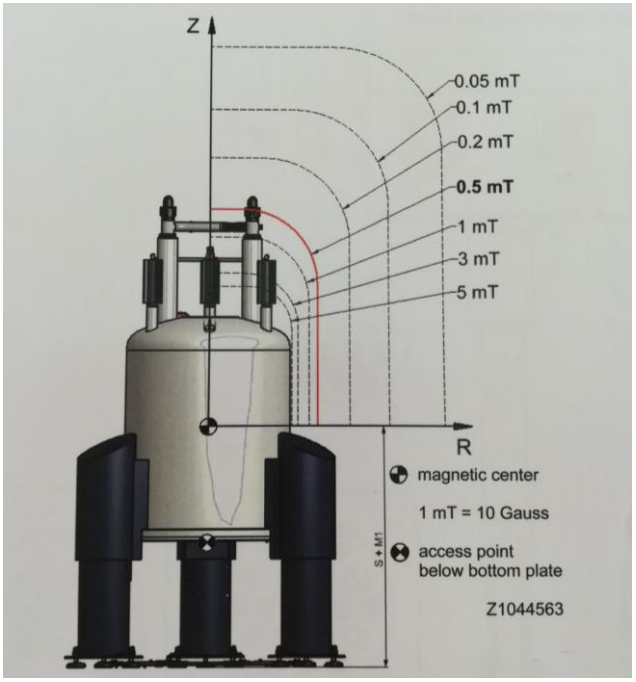

Figure 28 *Fringe field plot (taken from Bruker manual).*

At MNR Laboratory of Physics Department of Salerno, the spectrometer is equipped with a superconducting magnet that generates a field of 7 Tesla (300 MHz). As known, superconducting magnets at temperatures approaching absolute zero, 0K, have zero electrical resistance. A superconducting wire held below its transition temperature will give the possibility to get a continuously circulating

current. To maintain a superconducting system the magnet core is cooled to very low temperature using nitrogen and helium. The spectrometer in our lab requires helium every 6 months and nitrogen every 15 days.

The magnet core consists of a large coil of carrying wire in the shape of a solenoid. At the center of the coil, the static field is very intense, to allow the analysis of the sample placed inside the field.

The superconductive magnet consists of several sections. Like a “thermos” the outer casing of the magnet is evacuated and inner surfaces are silvered. Next comes a bath of nitrogen which reduces the temperature to 77.35 K (195.8°C) and finally a tank of helium in which the superconducting coil is immersed in.

This tank is thermally isolated against the nitrogen bath by a second evacuated section as shown in the picture below [Bruker User Guide].

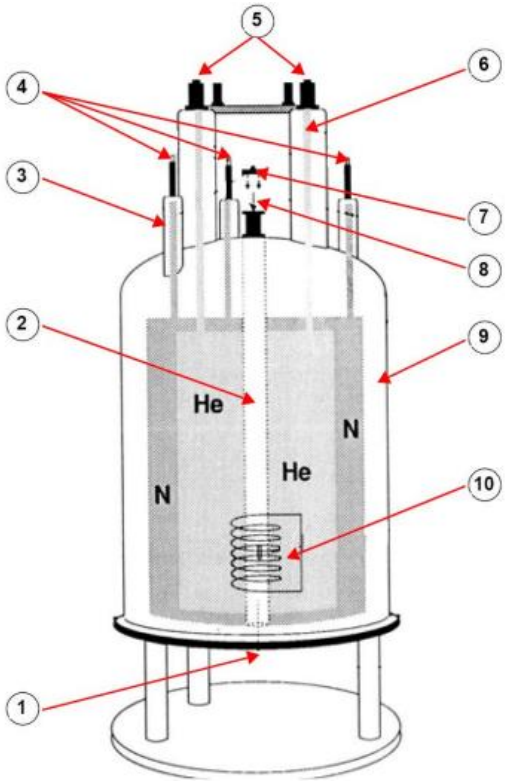

Figure 29 *Superconducting Magnet (taken from Bruker User Guide).*

1	Bore insertion	**6**	Helium Tower
2	Bore	**7**	Metal Plug
3	Nitrogen Tower	**8**	Sample insertion
4	Nitrogen Ports	**9**	Vacuum
5	Helium Ports	**10**	Magnet

The helium and nitrogen tanks are wrapped around the magnet bore (central column). A metal plug normally closes off the top of the bore. Samples to be analyzed are introduced into the magnet via the top of the bore. Probes, which hold the sample and carry signals to and from the samples are inserted from the bottom, like in the micro-imaging case.

3.1 Probes

The spectrometer is equipped with a MicWB40 Probe in combination with the Micro2.5 Gradient System. The MicWB40 probe has been developed for micro-imaging of small objects (max. diam. 30 mm) in wide bore magnets (89 mm ID).
The probe has an outer diameter of 40 mm and fits into the separate Micro2.5 gradient system.

Probe tuning and matching
The sensitivity of any probe will vary with the frequency of the signal transmitted to it and there exists a frequency at which the probe is most sensitive. Furthermore, this frequency may be adjusted over a certain range using capacitors built into the probe circuitry. Tuning involves adjusting the probe circuitry so that the frequency at which it is most sensitive is the relevant transmission frequency. Each coil in the probe will be tuned (and matched) separately. If the probe has been changed or the transmission frequency altered significantly, it may be necessary to retune the probe.

Whenever a probe is tuned it should also be matched. Matching involves ensuring that the maximum amount of the power arriving at the probe base is transmitted up to the coil which lies towards the top of the probe. This ensures that the minimum amount of the power arriving at the probe base is reflected back towards the amplifiers (and consequently wasted). It is also possible using an automatic tool ATM (Automated Tuning Routine) [Bruker User Guide].
Four different probes can be interfaced with the spectrometer:

1. Double Resonance Broadband Probe (BBI) – Liquid state
2. Probe Cross Polarization Magic Angle Spinning (CPMAS) - Solid state
3. Probe High Resolution Magic Angle Spinning (HRMAS)
4. Micro-Imaging Probe for Wide Bore Magnets

The latter is the one which has been used in this work (Figure 30, Figure 31).

Figure 30 *Exchangeable coil insert.*

Figure 31 *Micro-imaging probe and coil.*

3.2 Gradients

Usually, three sets of gradient coils are used in all MR systems: the *x*, *y* and *z* gradients**.** The gradient fields are produced by three sets of gradient coils one for each direction, can be applied in any direction or orientation. Each coil set is driven by an independent power amplifier and creates a gradient field whose *z*-component varies linearly along the *x*, *y*, and *z*-directions, respectively.

These fields are normally applied only for a short time as pulses through large electrical currents applied repeatedly in a carefully controlled pulse sequence. During an image acquisition, when the current is pulsed through the gradient coils in the presence of the static magnetic field, the gradient pulse produce Lorentz force which causes vibrations of the coils against their supports. The characteristic 'knocking' noise heard when an images is acquired is due to this reason.

The three sets of gradient coils are included in the MR system: G_x, G_y and G_z create a linear variation in the longitudinal magnetic field strength as a function of spatial position as seen in the section regarding the spatial encoding (section 2.1).

3.3 Nmr software

TopSpin and *ParaVison* are two processing software provided by Bruker.

TopSpin is used for NMR data analysis, acquisition and processing every time a spectrum is acquired.

TopSpin is designed with a highly intuitive interface and provides easy access to vast experiment libraries including standard Bruker pulse sequences and user generated experiment libraries. [https://www.bruker.com/products/mr/nmr/nmr-software/nmr-software/topspin/overview.html].

To perform MRI data acquisition and reconstruction has been designed a software package called ParaVision. It can be used to analyse, visualize and manage the data generated on Bruker systems.

A sub-package of ParaVision program is the *Image Sequence Analysis* (ISA) Tool, which provides a general and flexible framework for the visualization and statistical analysis of such sequences of images. It has been used as explained in the chapter 5 and 6.
The Bruker NMR Spectrometer is only one of the wide range of product available as research tool; NMR and MRI technology is continuously developing. Much of the success of these techniques is due to its flexibility and its potential for probing the properties of complex materials.

The use of NMR and MRI has spread from medical area to a large range of application: quality control in industrial, research in building materials, wood, paper and cultural heritage, geohydrology, plant physiology, well logging, cosmetic [8][9], paper industry [10], and food processing.
Some of these applications will be shown in the next chapter.

4. MRI Application

MRI born as a “safe” diagnostic protocol to obtain good resolution images of the patient and has gained in the last few years growing interest relying also on the absence of ionizing radiation.

Nowadays is the most dominant imaging method employed in medical investigation. It provides the best soft-tissue contrast among the existing imaging modalities.

The development of superconductive magnets to generate stronger magnetic fields and the new computing technologies have contributed to make MRI ever more performing.

4.1 Medicine

MRI plays an increasingly important role in clinical diagnosis; it helps to visualize the structures of the body that include water and fat molecules. MRI is a technique for taking very clear and detailed pictures of tissues and internal organs. Using different acquisition parameters (TE,TR), MRI allows acquiring high quality images with the possibility to enhance different types of tissues. Because of its high soft-tissue contrast and multiplanar imaging capability, MRI can reach excellent anatomic details. It is more sensitive than computed tomography (CT)

and allows differentiation among fat, muscle, tendon, bone and vascular structures based on characteristic signals. Due to these reasons, MRI has a major role in the evaluation of soft tissue tumours, for recognition, staging, and treatment planning of soft tissue and bone tumours [11]. This type of imaging allows also the detection of recurrent tumours in the presence of non-ferromagnetic metallic implants [12].

The appealing properties of imaging by magnetic resonance bring to several application like integration of MRI with PET (Positron Emission Tomography) or in conjunction with radiation therapy treatment.

In medical research, a current and increasingly in development application of high field MRI is the study of the brain. MRI currently is the most versatile and informative imaging modality for the central nervous system (CNS) [13], the investigation of the CNS from microstructure to physiology of the brain is under continuous investigation [14]. Several pathologies, like multiple sclerosis, brain tumours, aging-related changes and cerebrovascular diseases can be studied with high field (7-11 T) technologies [15][16].

One of the latest neuroimaging technique is the *functional Magnetic Resonance Imaging* (fMRI), used to visualize functional activity in the brain, investigate human brain function and cognition, measuring changes in blood flow in different parts of the brain comparing healthy and abnormal brain states. fMRI can detect small changes in the signals, associated with neuronal activity in the brain, which are used to produce magnetic resonance images. The haemoglobin contained in the blood exhibit different properties depending on whether or not it is bound to oxygen. When a specific activity is performed in the area of the brain responsible for that activity, the blood flow increases. This phenomenon is the so called *Blood Oxygen Level Dependent* (BOLD) effect. Setting specific parameters MRI can detect this increasing and BOLD can be used to create maps of brain activity. It is used to observe brain structures and to determine which parts of the brain are handling critical functions. One of the specific applications of fMRI is for example the investigations of abnormal functioning in psychological disorders.

fMRI may also be used to evaluate damage from a head injury or Alzheimer's disease.

It is also possible to combine fMRI with complementary imaging modalities, one of these is the use of the Diffusion Tensor Imaging (DTI).

Whereas with the fMRI it is possible to collect information about the synchronization of brain activation across different brain areas during rest or during a specific activity, DTI examines the diffusion of water in the brain to infer the integrity of white matter fibers. This technique allows to measures how water molecules diffuse through brain areas. A disease like stroke or tumor reduce this diffusion, so DTI allows to locate the anomalies. Using diffusion gradients the water diffusion in the brain is examined in several directions. The use of MRI in neuroscience research and in clinical neurological applications is more and more rapidly expanding [17].

4.2 Porous media

It easy to find a wide range of specific application of the NMR technique and of the imaging by magnetic resonace related to the study of porous media [18] [19].

Through the knowledge of the water distribution inside the porous structure, it is possible to identify the degradation processes and understand how to manage it.

Relying on the ability of MRI technique to achieve very high resolution images its use has found an interesting application also in the field of the study and preservation of artifacts related to our *cultural heritage* [20][21][22][23].

MRI results to be a good procedure to investigate the porosity of different lapideous materials (i.e.: marble, granite) as well as monuments or walls of historical buildings. Injecting a water agent contrast liquid in a porous material, the mobile molecules are confined in the matrix of the stones filling the pores. NMR signal shows an intensity that gives quantitative measurements of the content of the liquid.

An example is the study on the damage due to salt coming from seawater and from the environment. Salt crystallisation of porous media is widely recognized as

one of the primary causes of irreversible damage to many artifacts of historical or cultural interest such as wall paintings, sculptures, historic buildings, and other artwork. The presence of salt weathering in material such mortar and concrete characterized with small pores can cause cracks caused by the pressure which builds up during the formation of salt crystals. To prevent possible damage a deeper understanding of this mechanism would be very helpful.

The investigation of the pore-size distributions and porosity of rocks has relevant importance for geophysics and especially for the reservoirs of water, gas or oil. Oil companies are showing an increasing interest in the single sided NMR used for in situ well logging [24]. It provides a valuable tool in the exploration of hydrocarbon wells and has become a significant commercial application of NMR. Recent advances in the technique of NMR well logging have greatly enhanced the versatility and robustness of this measurement.

This technique, based on low field NMR, measures physical properties of the subsurface. Using NMR sensors that are lowered into boreholes, the measurements respond directly to the fluids in the subsurface and provide a unique tool for their characterization [25].

The analysis of NMR well logging data enables the quantification of the fluids occupying the pore space and the prediction of the fluid flow properties through the reservoir.

MRI and 2D T_1-T_2 correlation experiments have been developed to measure porosity and pore size distributions on water-saturated drill cores [26], to characterise pores and water dynamics in natural soil [27].

4.3 Engineering applications

MRI scanning is the only non-destructive technique for direct observation and quantitative measurement of internal crack structures in such detail, that’s why its development has led to several applications in material science [28][29].

As seen MRI allows the direct observation of both static and dynamic phenomena of fluid transport in porous media, providing detailed information about the porous microstructure (porosity, pore-size distribution) of these materials. This is the reason because of in civil engineering MRI is used in a wide range of fields; to determine the pore size distribution of cement pastes [30] [31] [32], to measure water content in a range of porous media including rocks [33][34][35][36], soils [37][38] and construction materials like bricks, cements and concrete [39][40][41]. The physical characteristics of construction materials and their microstructure (e.g., clays, sands, and concretes) are significantly affected by the action of water. MRI can follow up how water permeation causes and accelerates deteriorations such as rebar corrosion and freezing and thawing [42].

MRI is nowadays a powerful tool for basic research in civil engineering field and into various aspect of process engineering like the maps of temperature distribution in conventional or microwave heating, measurement fluid flow through complex geometries and measurement of solid–liquid separation using filters [43] or evaluation of chemical cleaning of biofouled reverse osmosis membrane using MRI [44].

4.4 Plants

Using NMR spectroscopy and MRI techniques it is possible to examine several aspects of plant function and performance, dynamics of plant water relations and water transport. The study of plants has an additional level of complexity since they are living systems which critically depend on transport and signalling processes between and within tissues and organs [45].

A phenomenon that commonly occurs, is the reduction of water in plant's cells respect to the normal level, the so-called *plant water stress*. This phenomenon affects the water content and hydraulic conductivity, including transport within cells, over membranes, cell-to-cell, and long-distance xylem and phloem transport. The stress responses transport processes can be followed non-invasively with MRI in the intact plant [46] [47].

As shown in chapter 6, a really interesting application of MRI on plants is the 3D analysis of root growth, root anatomy and water uptake. The precise measurements of root system architecture is an important requirement for plants studies. [48][49].

The combined use of MRI and of the diffusion tensor imaging technique (DTI) [50] allow the visualization of the root system architecture of plants and provide a 3D map of water mobility inside soil and roots.

Tractography generates channels that constitute pathways of facilitated water movement, representing the roots, calculated from water diffusion properties obtained from DTI experiments [51][52].

Although physiologically controlled MRI plant studies can be performed in laboratories, mobile systems for outdoor measurements have been developed to investigate tree and plants in their natural environments [53] [54]. Natural phenomena such as plant diseases and damage by insects can be investigated in this way.

4.5 Food

In food science and industry processing, MRI represents a fundamental work tool to collect precious information such as moisture migration, fat content and determine adulteration or measure the solid-to-liquid ratio of fats and oil and microbial spoilage. NMR and MRI have become a potential tool to explore and understand the structure and dynamics of various food constituents and able to give a relevant contribution to food analysis. In recent years MRI has started to be extensively used in the field of food research and food process development.

It has been applied to investigate different kind of foods: fruit, vegetables, meat, dairy products, cereals [55].

It is easy to observe the external qualities of food stuff such as size, shape, colour presence of damage, but a deeper analysis in the inspection of food is necessary if the aim is to determine the internal structure [56][57].

Several techniques are available to point out the internal quality of food. Near Infrared Radiation (NIR) has been used on apples, citrus and mandarina [58][59] [60][61]; multispectral technique for the detection of deterioration of fresh spinach related to storage; hyperspectral imaging on maturity stage of banana at different temperatures [62]; X-rays on cucumber fruit [63] and obviously NMR and MRI.

MRI has the potential to examine how moisture interacts in various food products and provides an understanding of the moisture uptake mechanism, moisture migration kinetics, and moisture interaction with various food matrices [64].

The moisture distribution of one of the most consumed foods, pasta, has been intensively studied to probe the internal moisture distribution in the pasta texture [65], crucial for the consumers perception. MRI has been applied to monitor the water ingress and distribution in pasta and noodle samples at different cooking stages [66][67], and the deterioration that comes quickly after cooking and during distribution because of the homogenization of moisture distribution [68]. It is possible to study the mobility and distribution of water in foods with low and intermediate moisture content [69], the moisture migration mapping in real time for cereal-based food [70] and to study the moisture migration during engrossing and aging in soft-panned confections [71]. The results of the cited studies and a lot of published articles, has shown that MRI is a great technique to study and monitor the moisture migration in multicomponent food systems [72].

MRI has been used to study the internal browning in some fruits such as pears [73] and apples [74] and to evaluate the maturity and the variation of internal structure and physical and chemical characteristics of tomatoes [75][76].

It revealed to be useful also to examine the growth and maturity of wine grapes and avocado [77][78] or to determine the presence of black heart in the pomegranate [79].

Over the years dedicated NMR systems, that are specially designed with smaller magnets and lower magnetic fields for the needs of food industry have been developed. Bruker has proposed NMR FoodScreener Solutions for the detection of adulteration and mislabelling of content or origin of honey, wine and juice. The

acquisition of the spectroscopic fingerprint, specific to each individual sample returns profiles that are compared to a large database of authentic food samples, using a multivariate statistical approach. Food profiling is an innovative and promising solution for the analysis of food using NMR spectroscopy. The availability of a portable system would increase the research and commercial applications of NMR and MRI in the food industry in the next future.

5. Application in food science

As seen in the previous chapter the MRI, as a quantitative tool has significantly increased over the last twenty years [80].

Among the several advantages of MRI, the knowledge of mobility and distribution of water in a food matrix represent a powerful tool for characterizing food quality during processing and storage [81][82], since it can provide information about changes on a microscopic scale.

The water relaxation time sensitivity to changes in the molecular dynamics is the starting point of MRI investigations into food processing operations.

Since the majority processing operations induce changes in water content and molecular structure, it is desirable to develop strategies to study and to monitor the moisture migration in order to collect useful information to improve the processes on terms of production, storage, transportation and shelf life stability. The idea of the present study is to design appropriate MRI protocols and provide correct interpretations of the data collected through different techniques and approaches.

5.1 Moisture migration

The advantage of using ^{1}H imaging is that it is very sensitive to water protons that are the major components of all food matrices.

Due to the presence of high water content, fruits and vegetables are suitable to be analysed by MRI. Studying the internal moisture content and distribution and their changes in food products during drying is essential.

Through the study of water mobility, MRI allows a deeper understanding about the physical and chemical characteristics of food systems.

Investigating the drying process through MRI analysis provide a real-time, non-destructive, and non-interrupted testing and monitoring of the process.

The moisture migration within the components of a food with varying water activity is indispensable to understand food microstructure and to preserve it from degradation [83].

Moisture migration is a complex mechanism that plays a significant role in food science and engineering. Keeping a check on the water changing, during drying processes, MRI provides plenty of information about microstructure, moisture distribution and mobility.

The most common process used to remove water from fresh vegetables or fruits is the drying method. It is the process whereby moisture is vaporized from a material and is taken away from the surface (Figure 32). Commonly in food-drying operations to describe depriving a material of its water or the loss of water as a constituent the drying process it is said *dehydration*.

The thermal process of removing water and evaporating moisture leads to a variation in the spatial distribution of water inside the samples. This involves several physical, chemical and biological changes such as shrinkage, cracking, etc. This is the reason why the dehydration process is a crucial technique in food industry.

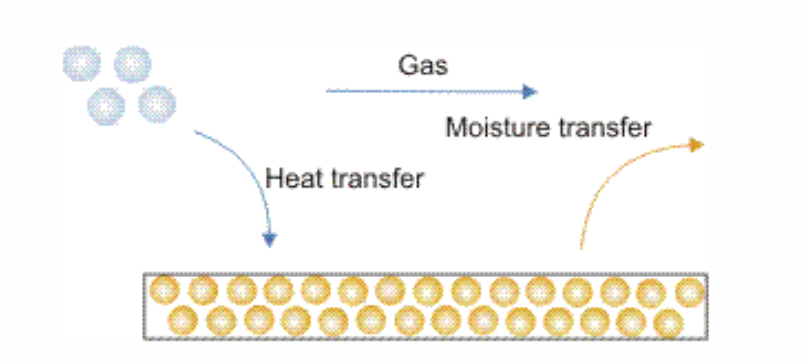

Figure 32 *Drying process (Taken form 10.1615/AtoZ.d.drying).*

In this work the drying process of pumpkin, a sample with high water content (> 90%), has been investigated at four different drying temperatures.
In order to correlate relaxation time T_2 to water content, T_2 maps of the samples have been carried out. The aim of this experiment is to obtain quantitative moisture distribution maps that allow the study of the mass transport phenomena in foods during dehydration.

5.2 Low field investigation on eggplants

The NMR Laboratory at the Physics Department of the University of Salerno has started the use of NMR on food through imaging already few years ago.
A first study has been done on eggplants (*Solanum melongena L.*) [84]. This study has been performed using a low field (0.5 T) NMR spectrometer (Resonance Instruments LDT mod. Maran DRX, 21.4 MHz).
The eggplants study investigated the effect of hot air drying on the physical properties of cylindrical eggplant samples. Through MRI, the drying kinetics, the water profiles along longitudinal and transversal sample sections and the volumetric shrinkage have been determined. MRI showed the water migration occurring mainly in the transverse direction; the variation in the longitudinal direction being negligible, see Figure 33.

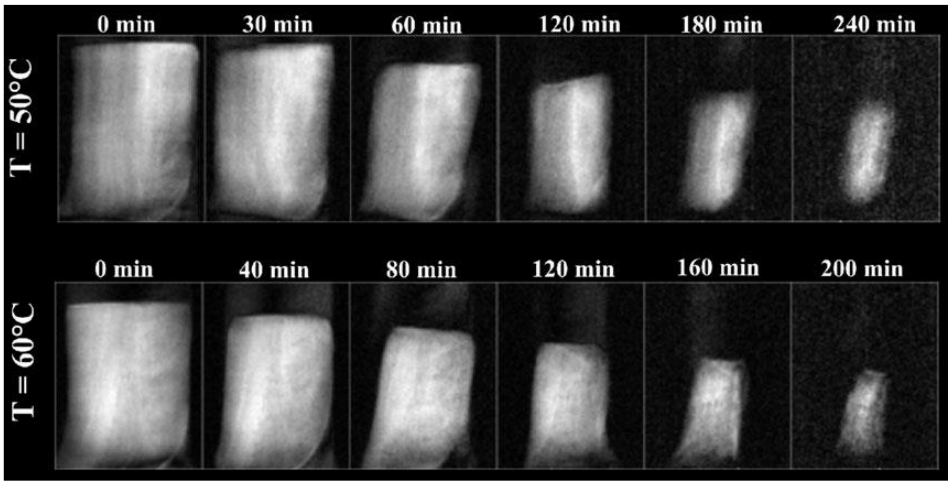

Figure 33 *Two-dimensional spin echo images of eggplant at both investigated temperatures and selected drying times.*

In the same figure the signal contrast displayed in each image, is obtained from the sample protons density.

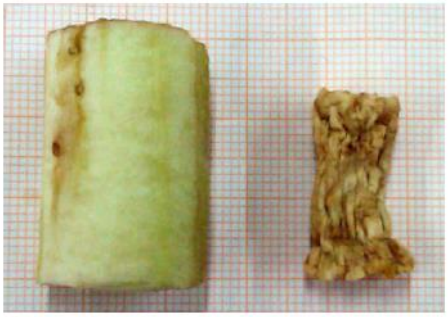

Figure 34 *Eggplant fresh sample (left) and dried sample after 240 min of dehydration at 50 °C (right).*

Figure 35 shows the signal intensity profiles along the longitudinal and the transverse cross sections, taken at the geometric centre of each sample. It has been observed that in the first drying steps, the profiles show a bigger distance one from each other at 60 °C with respect to the 50 °C drying process. In fact, at 50 °C the signal intensity profiles along both the longitudinal and transverse cross sections were very close to each other in the range from 0 to 60 min. In addition, the water removal at 60 °C was faster than at 50 °C, keeping as a benchmark the same water distribution profile in each drying step [83].

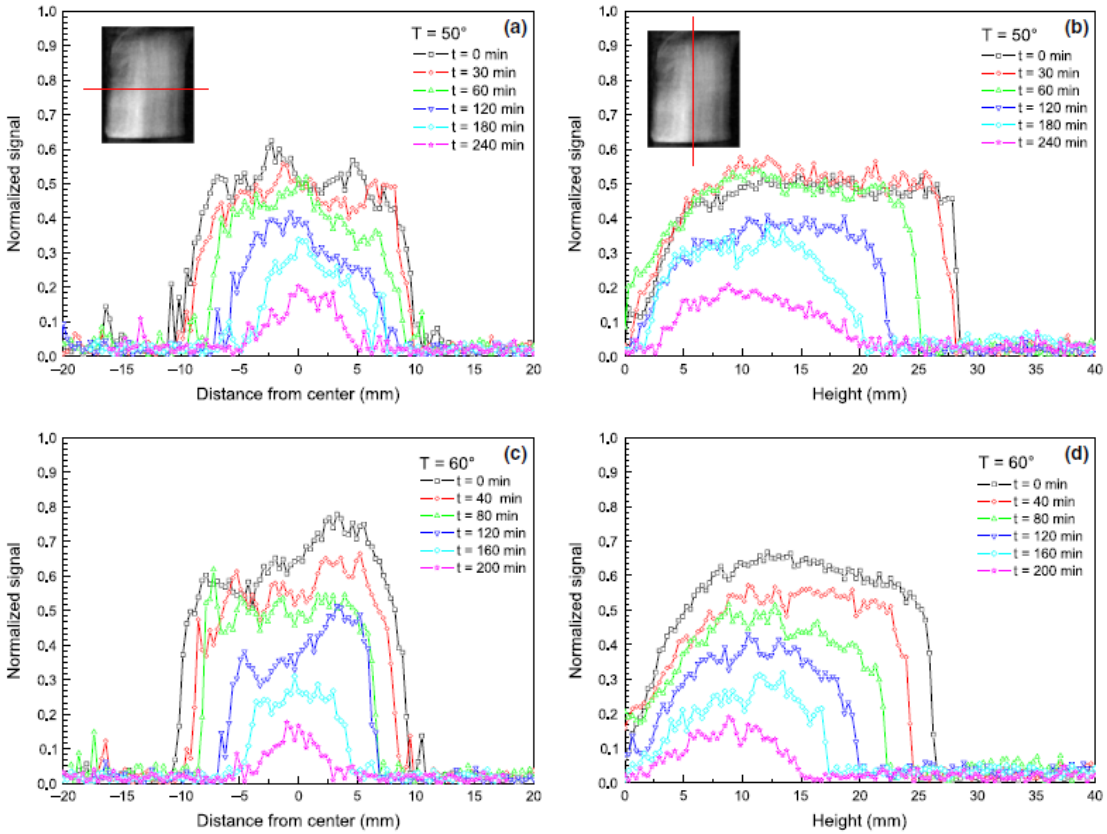

Figure 35 *Profiles of normalized signal along the transverse (a, c) and longitudinal cross section (b, d), taken at the geometric centre of each sample, for selected drying times at T = 50 °C (a, b) and 60 °C (c, d).*

slice The curves of mass water loss obtained by both the standard weighting method and MRI, show a good agreement. This can be seen in Figure 36 where the comparison between the values obtained by gravimetric and MR method is shown for each temperatures of the dehydration process.

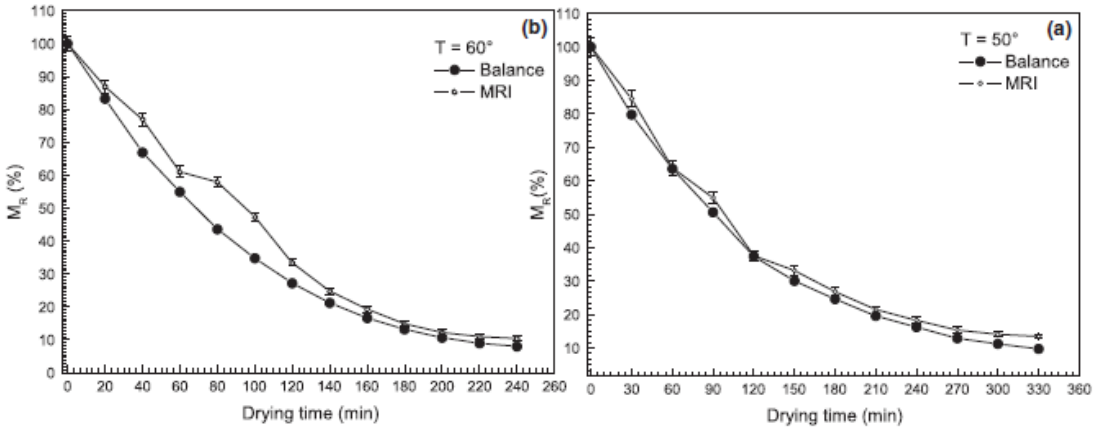

Figure 36 *Moisture ratio (%) of samples during drying, obtained by gravimetric method and MRI at T=50°C (a) and T=60°C (b).*

This preliminary study shown that MRI technique offers the possibility to study water distribution in food during drying processes in a non-destructive way. In addition, a FEM (Finite Element Method) model has been developed in order to simulate the water concentration profile [85].

A significant improvement of this approach has been obtained taking advantage from the new Bruker spectrometer acquired by the lab, with which we have studied moisture content in other food matrices using high magnetic field.

5.3 High field experiment on pumpkin

Using the new Bruker NMR spectrometer (7T) equipped with a micro-imaging probe a new analysis has been performed.

Pumpkin is one of the most important vegetables grown in the world because of its nutritional and healthful qualities. It is a good source of vital antioxidants and vitamins (carotene and vitamin-A, vitamin-C and vitamin-E) [86]. This fruit is rich in phenolics, flavonoids, polysaccharides, mineral salts and other substances beneficial to health.

Fresh pumpkin should be stored at temperature between 10° C and 13 °C and relative air humidity should be between 50% and 70%. When stored at lower

temperatures, unfavorable physiological processes occur causing chill damages. Furthermore, after peeling, pumpkin is susceptible to moisture loss, softening, color changes and microbial spoilage. The high level of water content in pumpkin makes it easily damageable.

Therefore, it is desirable to use optimal methods of pumpkin preservation, appropriate for the specific final use of the fruit.

Pumpkin is generally processed to obtain juice, pickles and dried products in many countries worldwide. As a dried product, it is available as snack food, dried premix, soup, etc. In order to reduce the water and microbiological activities and to minimize the physical and chemical changes during vegetable storage, the drying technique is commonly used [87] [88] [89].

In the following experience, MRI is applied to detect and monitor the progression of internal amount of water in pumpkin and to investigate the changes in moisture distribution vs time observed during drying of pumpkin samples.

Materials and methods

The analysis on the pumpkin samples have been performed on the cultivar *Cucurbita Maxima*. The samples have been cut from the fresh pumpkin, using a steel mould to make small parallelepiped of about $(10 \times 10 \times 16)$ mm^3.

The dimensions of samples have been chosen on the basis of the test tube diameter (15 mm) and in order to obtain a well detectable signal also at high drying temperatures.

For each experiment the samples from several peeled vegetables have been mixed randomly, in order to minimize the differences in the food matrix, which could invalidate the analysis,

To express the water content, the concept of dry basis is used. The dry basis is a measure of the amount of water in a solid and it is expressed in terms of the weight of water as a percentage of the completely dry solid.

When a sample loses moisture, the change in the dry basis moisture is somehow linearly related to the weight loss. For the fresh pumpkin the initial moisture content of samples was (13.29 ± 0.53) $kg\ kg^{-1}$ *dry basis* corresponding to a water

percentage of 93% *(13.29/14.29=0.93).* The water activity, which is a parameter used to describe the energy status or escaping tendency of the water in a sample, is 0.96 (measured by a hygrometer).

A bench-top temperature humidity chamber (Espec Corp. mod. SU-221), with an air velocity of 1.2 m/s, has been used to dry pumpkin samples at fixed temperatures.

The drying experiments have been carried out at four different temperatures: 50°, 60°, 65° and 70° C, to investigate the effects of temperature on moisture migration. The samples have been placed in the climate chamber and were weighted at fixed time intervals during the drying process until the weight does not significantly change anymore (changes in weight are less than 5% of the whole sample).

All specimens have been weighted using a digital balance (Shimadzu mod. AW320). Each test has been conducted on five samples and the weight loss with standard deviation is registered.

Figure 37 *Digital balance (Shimadzu mod. AW320) and bench-top temperature humidity chamber (Espec Corm mod. SU-221).*

From gravimetric measurements, the Moisture Ratio values (M_R) have been evaluated using the following formula:

$$M_R = \frac{M(T) - M_\infty}{M_0 - M_\infty} \tag{42}$$

where M is the mass of the sample during drying while M_0 and M_∞ refer to its initial and equilibrium value, respectively. Because the values of M_∞ is really small compared with M_0 and M the (42) can be written as follows:

$$M_R = \frac{M(T)}{M_0}. \tag{43}$$

During the drying, carried on at fixed temperatures, a selected sample has been used to make the MRI experiment. After weight measurements and MRI acquisitions, the samples were immediately placed in the oven to continue the drying process. The weight loss obtained by gravimetric measurements have been compared with relaxation data collected by magnetic resonance imaging and are shown in section 5.5.

5.4 ^{1}H MR imaging on pumpkin

Using the ^{1}H MR imaging on biological samples, the proton signal comes predominantly from the water proton. It is possible to distinguish three water environments: inter-cellular, intra-cellular and cell wall water. Each environment corresponds to a different bound strength. Taking into account these differences, it is possible to talk about free water (FW), loosely bound water (LBW) and strongly bound water (SBW). Water mobility, defined as the ability of water molecules to rotate freely, is clearly related to the type of bound: it decreases as bound strength increases.

The transverse relaxation time, T_2, is influenced by the molecular mobility of the water. Higher values of T_2 can be associated to a greater mobility of water; lower values instead reveal the presence of a more rigid structure. This explains the presence of different T_2 components. This behaviour is described by mono-

exponential or multi-exponential decay curve, indicating different water mobility. T_2 value can be a powerful tool to get information on water dynamics.

Generally, in inhomogeneous systems, each voxel contains various water compartments and the signal decay curve becomes multi-exponential, with several T_2 relaxation times depending on water location.

In homogenous systems, T_2 relaxation process is mono-exponential with a well-defined T_2 relaxation time. NMR experiments have already highlighted a correlation between the T_2 and the water content [90]. This means that T_2 shows a behaviour roughly proportional with the level of samples hydration. Khan et al. [91] shows that in a pumpkin sample the major percentage of water appear loosely bound (LBW) and this kind of water is removed for the most part during drying process. Figure 38 shows the comparison of the prevalence of water binding in several different vegetables.

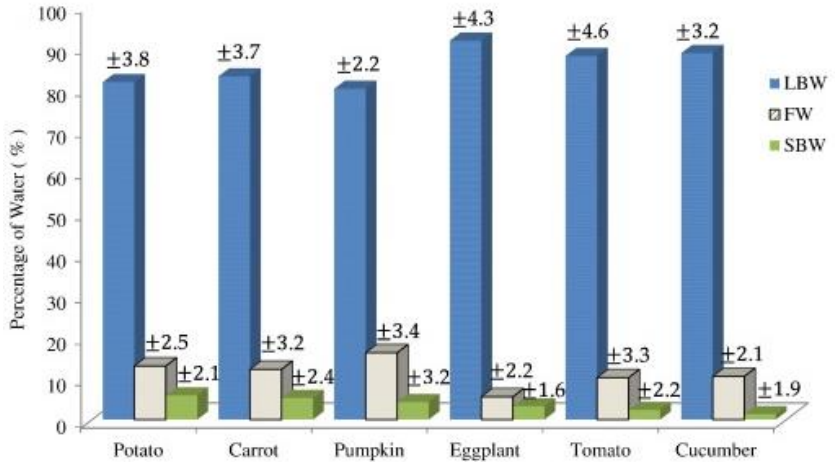

Figure 38 *Percentage of the different water environments in various vegetables (taken from* [91]*).*

Since in the mapping procedure a single T_2 value is ascribed to each voxel, to establish the correlation between the T_2 and the water content, it is necessary to convert this local information into a global one. This is necessary in order to have a value comparable with the gravimetric one. So all T_2 values in map were collected in a unique global value, named S; for fresh samples, this sum was named S_0. S is estimated at each drying step by adding together all the T_2 values

coming from each voxel and normalizing it to the global T_2 value of the fresh sample, defining a new value:

$$ST_2 = \frac{S}{S_0} \tag{44}$$

Using the value ST_2, the T_2 profile could be compared with moisture ratio values (M_R) obtained by gravimetric measurements.

MRI protocol

NMR experiments were recorded using the Bruker spectrometer (described in details in chapter 4), operating at the frequency of 300 MHz ($B_0 = 7$ T) equipped with a MicWB40 Probe in combination with the Micro2.5 Gradient System.

In order to describe the water changes during drying process, T_2 maps were obtained by 2D imaging of the pumpkin sections. The map has been obtained from a MSME sequence registered at the end of each drying cycle. The results are shown in the section 5.5.

The acquisition time has been of about 1 hour for each sample.

The MRI sampling parameters have been set as follow:

- TR = 5*T_1
- TE as short as possible in order to have a T_2 maps

For quantitative measurements a better choice is to set a TR five times bigger than T_1 in order to assure the complete longitudinal relaxation.

To evaluate the best TR the MSMEVTR_8e_8r sequence (Multi-Slice Multi-Echo Method with variable Relaxation Delay) has been used on fresh samples.

This sequence uses a saturation pattern (TR variated) to acquire T_1 and a multi-echo (TE variated) CPMG scheme to acquire T_2. In the study, eight TR values (800÷15000 ms) and eight TE values (15÷270 ms) have been used. The ROI (Region Of Interest) has been chosen to cover the whole sample. Other image parameters were: FOV (Field Of View) =16 mm × 16 mm, slice thickness =1.0 mm, matrix size=128×128. The spatial resolution was 0.063 mm. The time

constant T_1 is carried out from the ISA analysis tool. The value obtained is about T_1= (2600 ± 60) ms.

The sequence used to produce the map is MSME with the following parameters: TR=5T_1= 13*10^3 ms and TE from 5 ms to 100 ms, matrix size = (256 x 256).

The FOV has been chosen to cover the whole sample: FOV =16 mm x 16 mm and slices of 1mm thickness are selected.

The intensity of the T_2

map has been calculated using the ISA tool package.

T_2 is calculated from the relation:

$$Y = A + C \times exp\left(-\frac{t}{T_2}\right) \tag{45}$$

where A is the absolute bias and C the signal intensity.

This function uses an Echo Time list calculated from the protocol parameters to generate the t-axis. The fit is based on magnitude images of the reconstructed dataset. In order to generate a cut off of the noise level for the T_2 calculation of the image, the All-ROI threshold is chosen at 15% with respect the default value of 10%, automatically defined in the active viewport.

This generates a cut off of the noise level for the T_2 calculation of the image.

The standard deviation of the whole fit is the last image in the sequence [ParaVision manual]. An example of the fit obtained is shown in Figure 39.

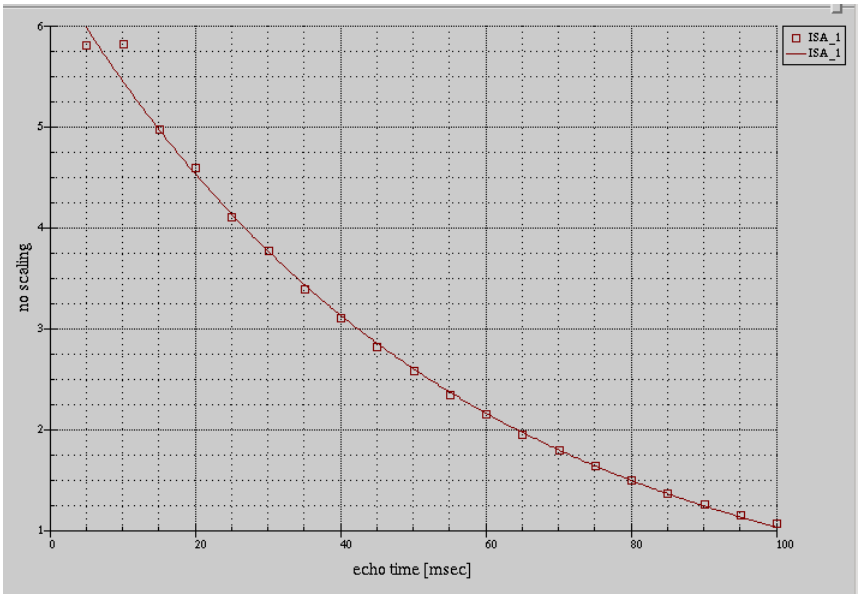

Figure 39 *The envelope of the spin-echo peaks decays exponentially with T_2 obtained with ISA Tool.*

5.5 Results

Raw data obtained from the NMR measurements were processed either by the software provided by Bruker TopSpin and ParaVision respectively for spectroscopy and imaging and then processed also by analysis tool, Origin.

In the pumpkin samples, the moisture content decreases during drying. In Figure 40 we show the moisture ratio of samples (in percentage) during dehydration at different drying temperatures, obtained just through the gravimetric method using a digital balance.

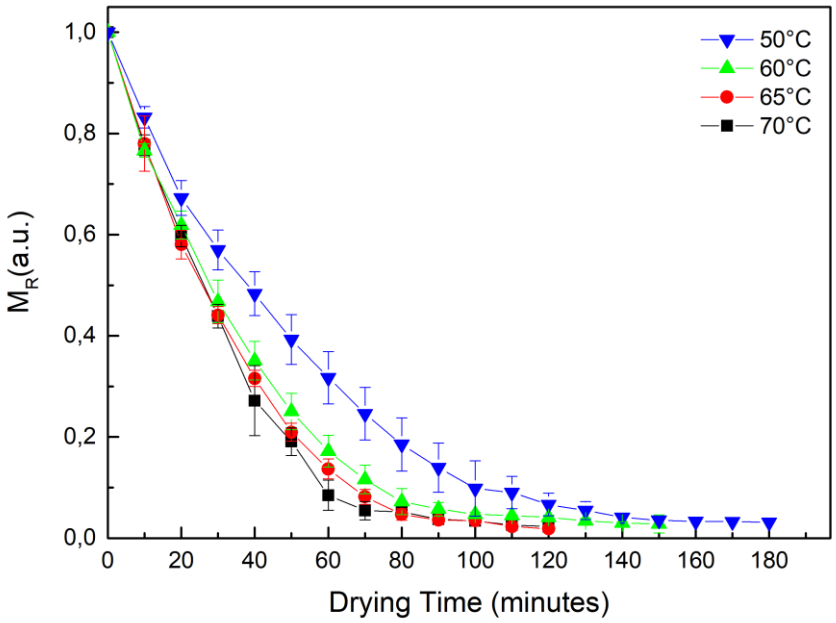

Figure 40 *Drying kinetics obtained by gravimetric procedure.*

As expected, it is evident that higher temperature reduces drying time. The residual moisture content at the end of process is similar for each test at 50°, 60°, 65° and 70°C.

Observing the plots that represent the moisture loss versus time (Figure 40) we can point out, with regard to the drying rate, two main regions. In the earliest stages of the process a rapid moisture loss occurs that leads to a fast drying rate. In the second region, instead, the moisture migration is slower and the drying rate decreases.

It can be observed, in fact, that after an initial *constant rate* period, the drying process for pumpkin samples continues with a phase characterised by a *falling rate* region. The constant rate is the initial stage of drying when the moisture removal occurs at the surface by evaporation and the internal moisture transfer is sufficient enough to maintain the saturated surface. In the falling-rate stage, the surface of the sample is not saturated and the evaporation rate is greater than the transfer rate of water through the sample.

There are several reasons that can justify this behaviour. At a certain time, the partial pressure of water through the whole sample is below the saturation level.
In order to be supplied to the inner part, heat has to be conducted through dry solid and porous regions, both of which have low thermal conductivity.
As long as the moisture content in the sample decreases, the internal resistance to moisture transfer increases [92]. For these reasons the drying rate in this period is extremely slow. In this final stage, the diffusion is the dominant mechanism governing moisture transport inside the sample.
This behaviour is in agreement with the results reported in literature for pumpkin and other vegetables [93] [94] [95].
The goodness of our method in terms of T_2 estimation of moisture content is evaluated by plotting the values obtained through gravimetric measurements together with the ST_2 values extracted, at each drying step, by the T_2 maps and described in details in section 5.4 (MRI protocol).
The very good agreement ($r^2 > 0.995$) between the curves of global weight loss obtained by standard gravimetric method (black squares) and MRI data obtained with the procedure described above (red squares) are shown in the following plots (from Figure 41 to Figure 44).

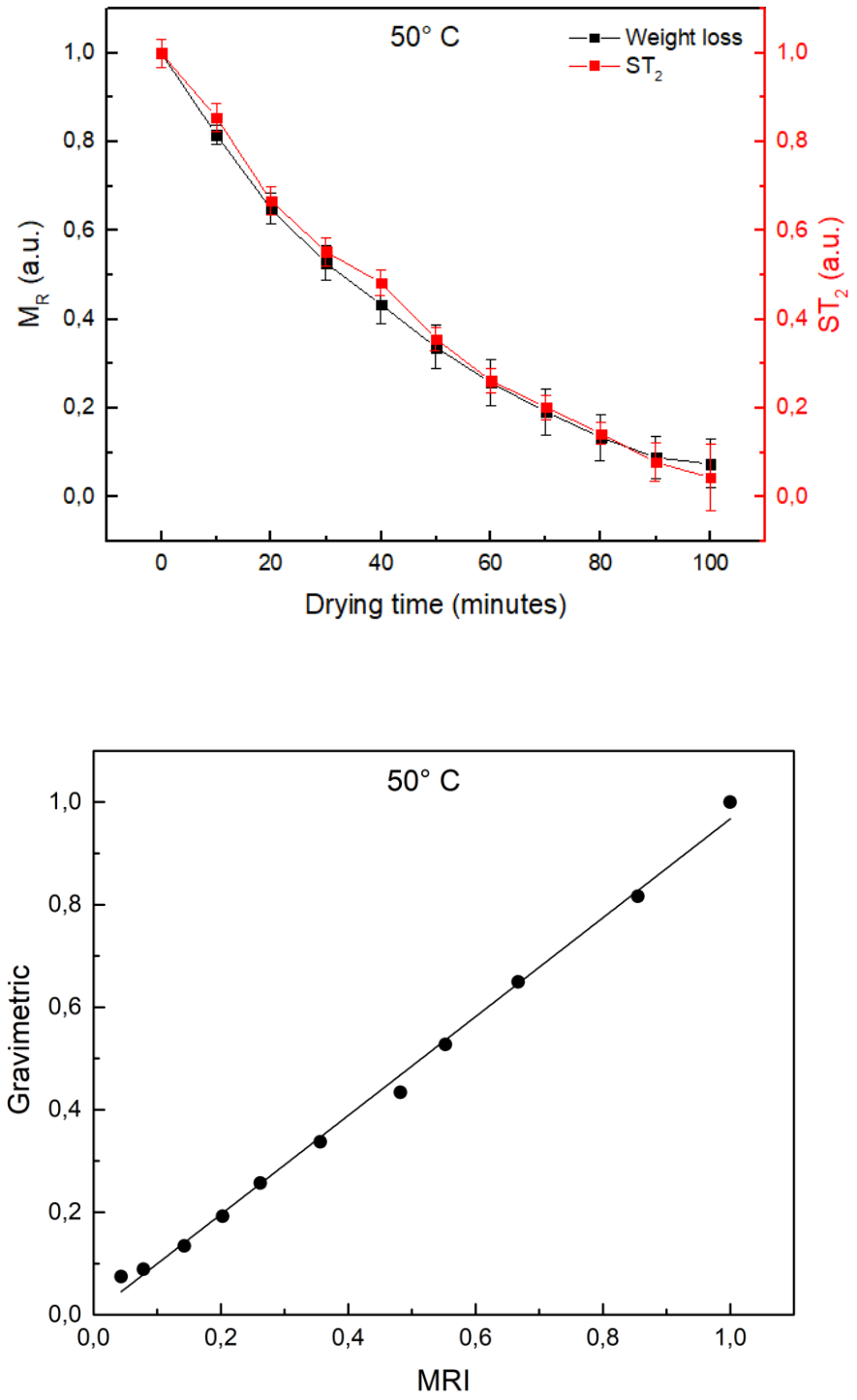

Figure 41 *Moisture ratio (a.u.) of samples during drying, obtained by gravimetric method and MRI at T=50° C (r^2=0,995).*

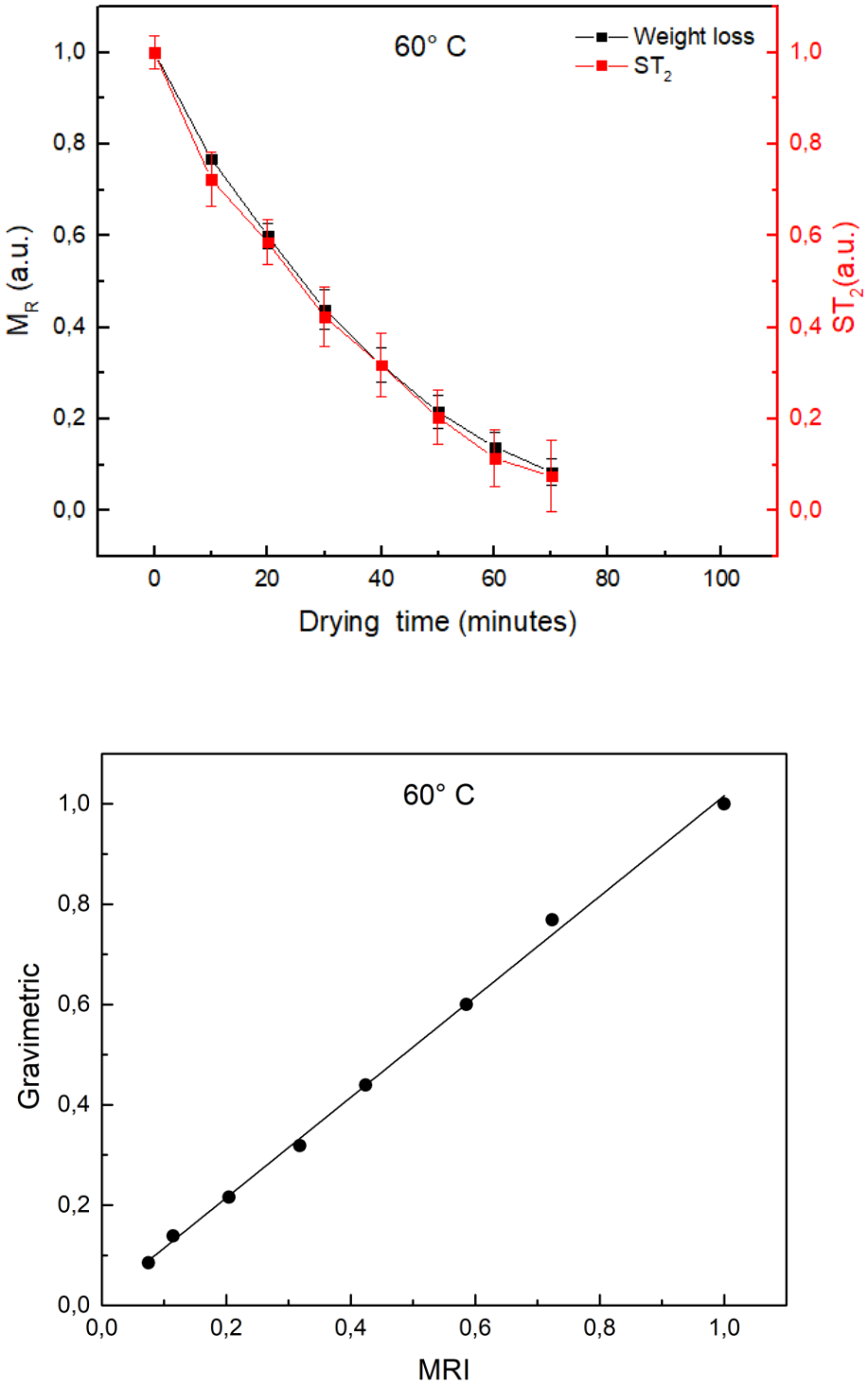

Figure 42 *Moisture ratio (a.u.) of samples during drying, obtained by gravimetric method and MRI at T=60° C (r^2=0,997).*

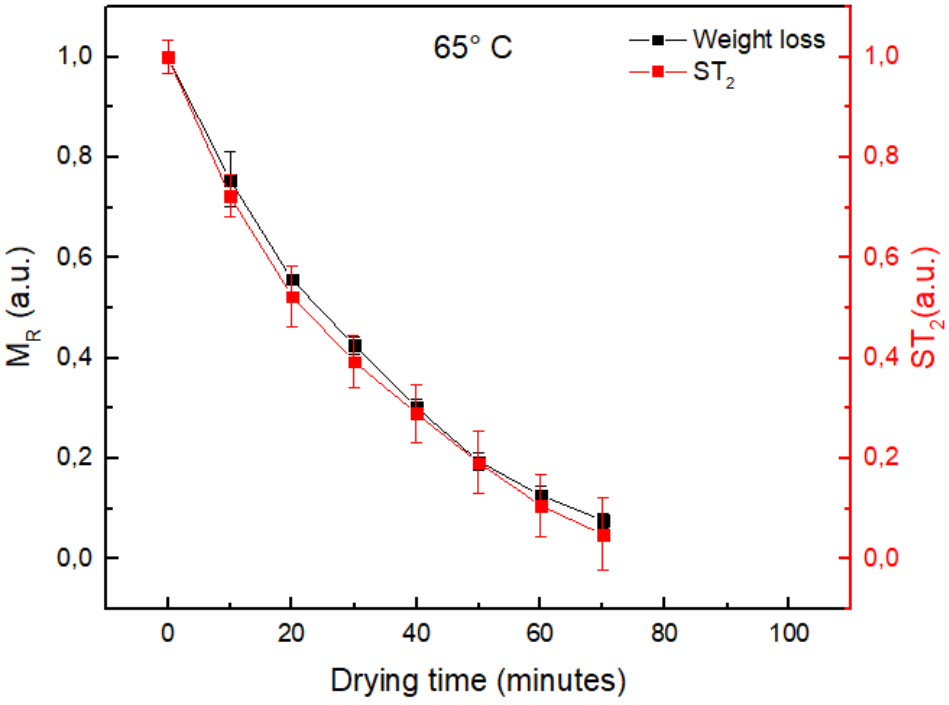

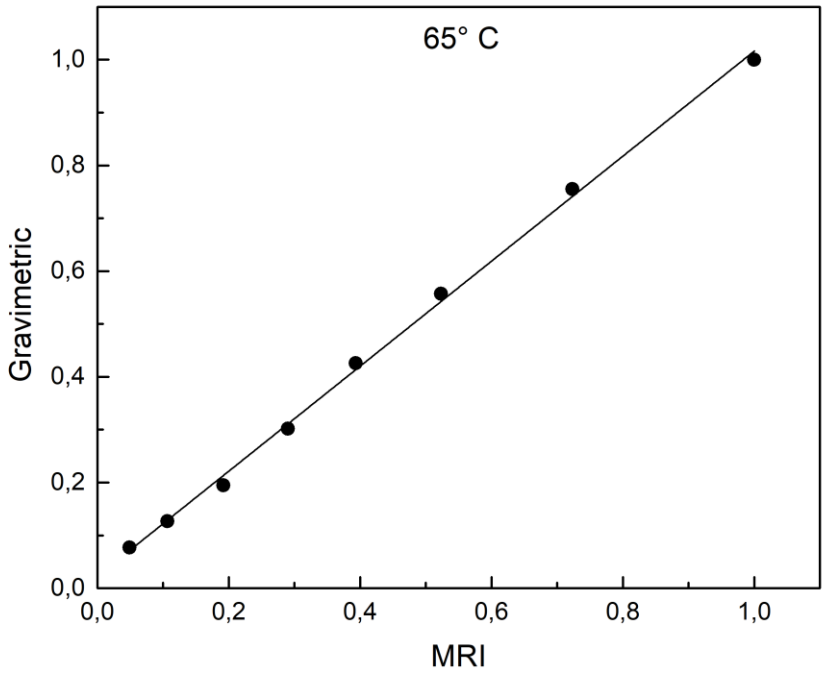

Figure 43 *Moisture ratio (a.u.) of samples during drying, obtained by gravimetric method and MRI at T=65° C (r^2=0,997).*

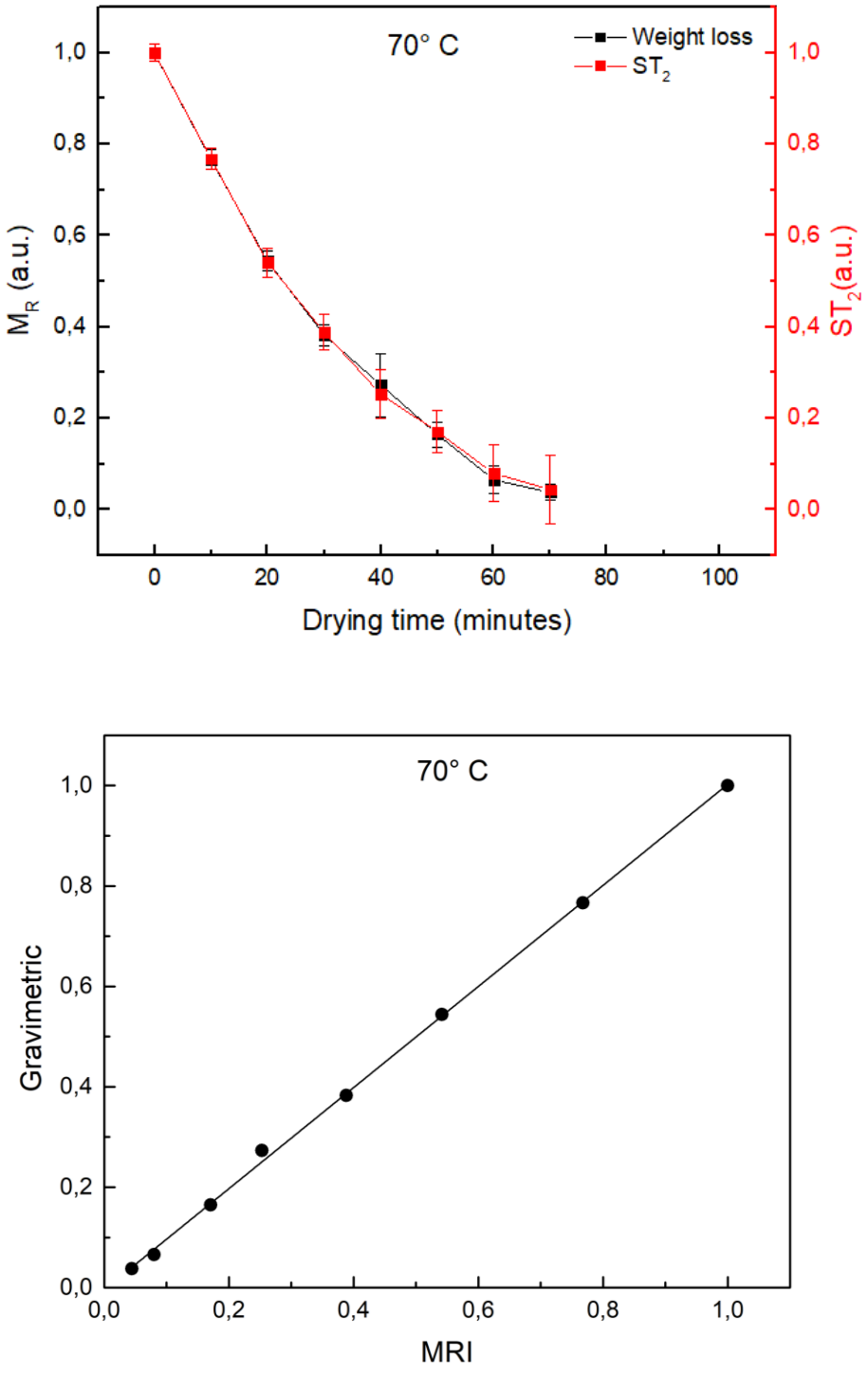

Figure 44 *Moisture ratio (a.u.) of samples during drying, obtained by gravimetric method and MRI at T=70°C (r^2=0,999).*

As we can see, looking at the 50° C temperature plots, the T_2 estimation give measurable signals even after 100 minutes of drying.

For the other temperatures (60°, 65° and 70°C), the T_2 signal extracted by the maps becomes too small to be detected, already, after 70 minutes of drying.

Referring to Figure 40, for M_R values below 0.1, the water distributed inside the food matrix is hardly evaporated during the drying process. Indeed, the time required to remove the residual moisture content from 10% to 3% is almost equivalent to the time required to remove the first 90% of the total moisture content.

As a matter of fact, when the water content in the sample become too small, usually strongly bound or immobilized inside the food matrix, also the T_2 measurements and the signals related become hard to be measured with our method. Nevertheless, this concern actually the residual water, well below 10% with respect to the total moisture content of the fresh sample.

For this reason, a comparison between the gravimetric measurements and the T_2 data has been done only in the range in which we have measurable T_2 signals.

The contrast in the MR images reflect the magnitude of T_2 values reconstructed; longer T_2 indicates a higher moisture content (bright area) whereas shorter T_2 a low content of water (dark area). It is clear that in the pumpkin sample, where the water content is higher than 90%, the area is almost completely white.

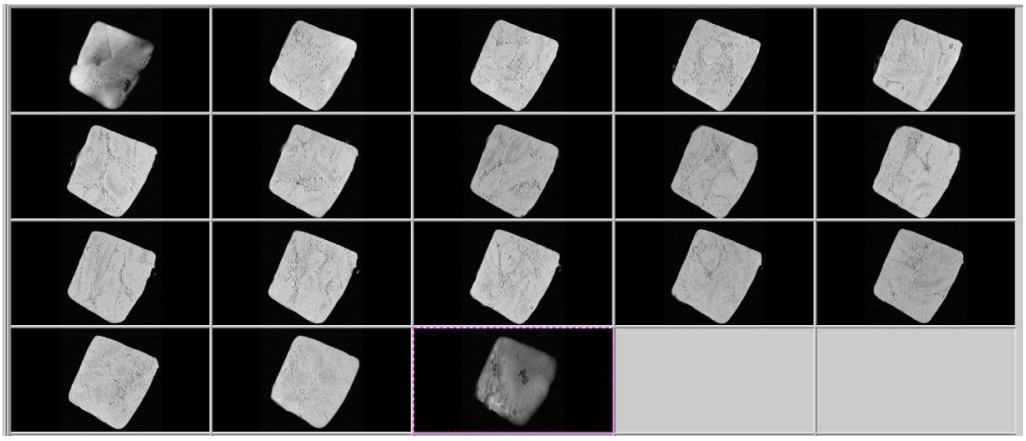

Figure 45 *Axial slices of fresh pumpkin sample at 70°C.*

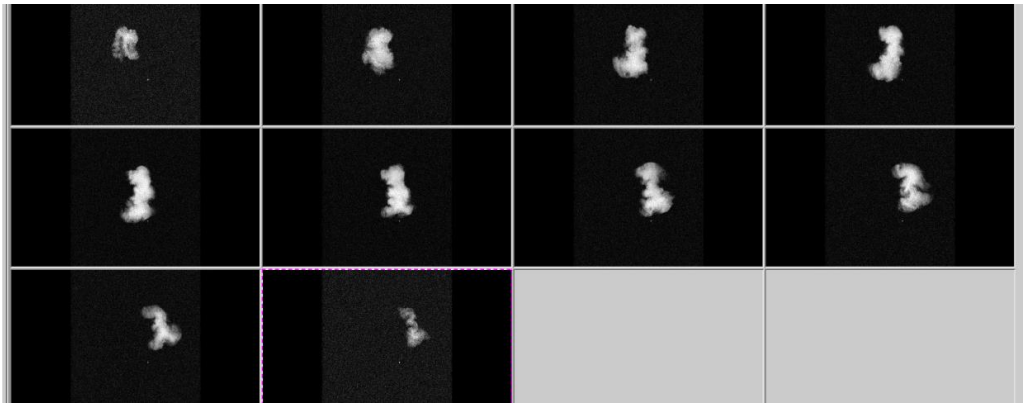

Figure 46 *Axial slices of pumpkin sample after 70 minutes at 70°C.*

During the drying processes, the most obvious effect of water evaporation is the loss of weight.

As we can notice after 70 minutes at 70° C (Figure 46) the impact of the loss of water cause a visible shrinkage of the pumpkin sample which show a considerable reduction in size, as expected. This behaviour will be described in detail in the remainder of the chapter.

In fact, another way to extract information from the T_2 data is to plot the transverse profiles of normalized T_2, taken slice-by-slice and step-by-step during drying, as shown in the following figures:

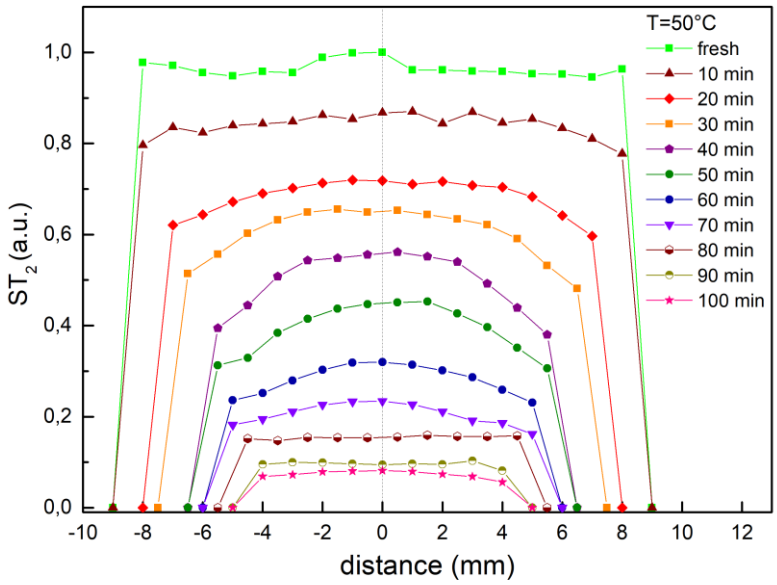

Figure 47 *Transverse profiles of normalized T_2 taken slice by slice for selected drying times at 50°C.*

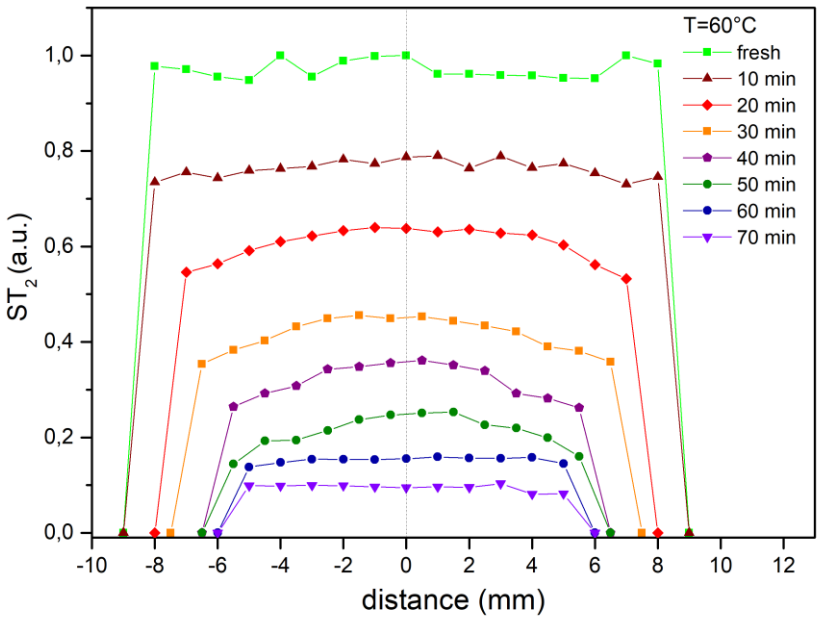

Figure 48 *Transverse profiles of normalized T_2 taken slice by slice for selected drying times at 60°C.*

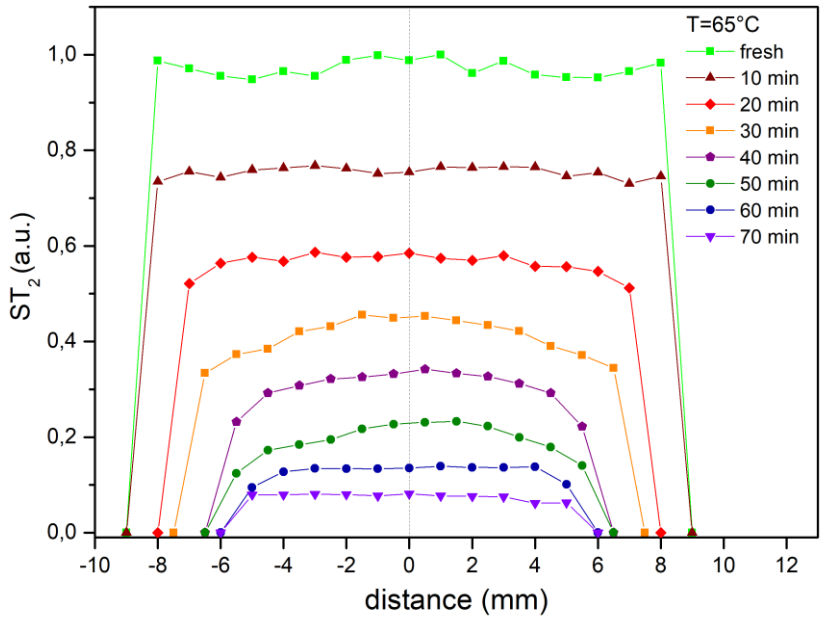

Figure 49 *Transverse profiles of normalized T_2 taken slice by slice for selected drying times at 65°C.*

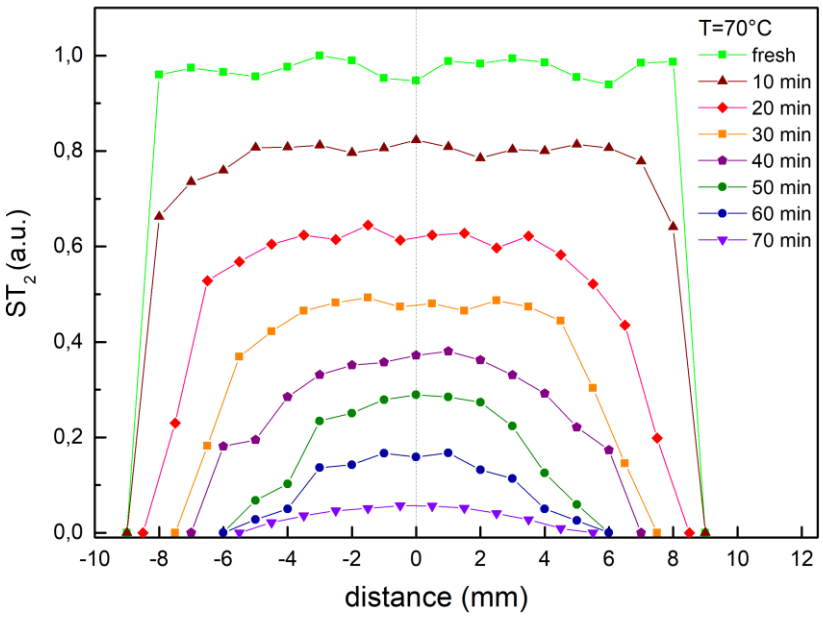

Figure 50 *Transverse profiles of normalized T_2 taken slice by slice for selected drying times at 70°C.*

The moisture loss and the reduction in size of the samples are clearly observed. Integrating the area under each curve it is possible to compare the trend for each temperature, as shown in the Figure 51.

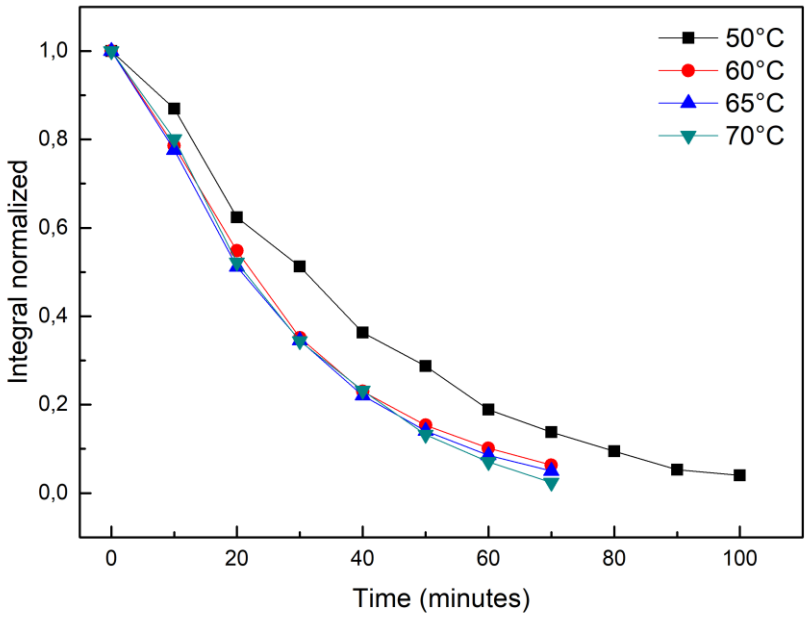

Figure 51 *Comparison at all temperatures between the values of normalized integral area under water peak.*

During the drying process, the samples reach half their weight in only two steps (2x10 min) for temperatures spanning from 60°C to 70°C, whereas it is needed an additional drying step (3x10 min) to obtain the same decrease at 50°C.

The amplitudes of profiles and their shapes are clearly affected by both the drying time and the temperature. A more real vision of the drying process and its impact on the size and shape of the pumpkin sample can be seen in the series of 3D MR images taken at three different drying steps, shown in Figure 52.

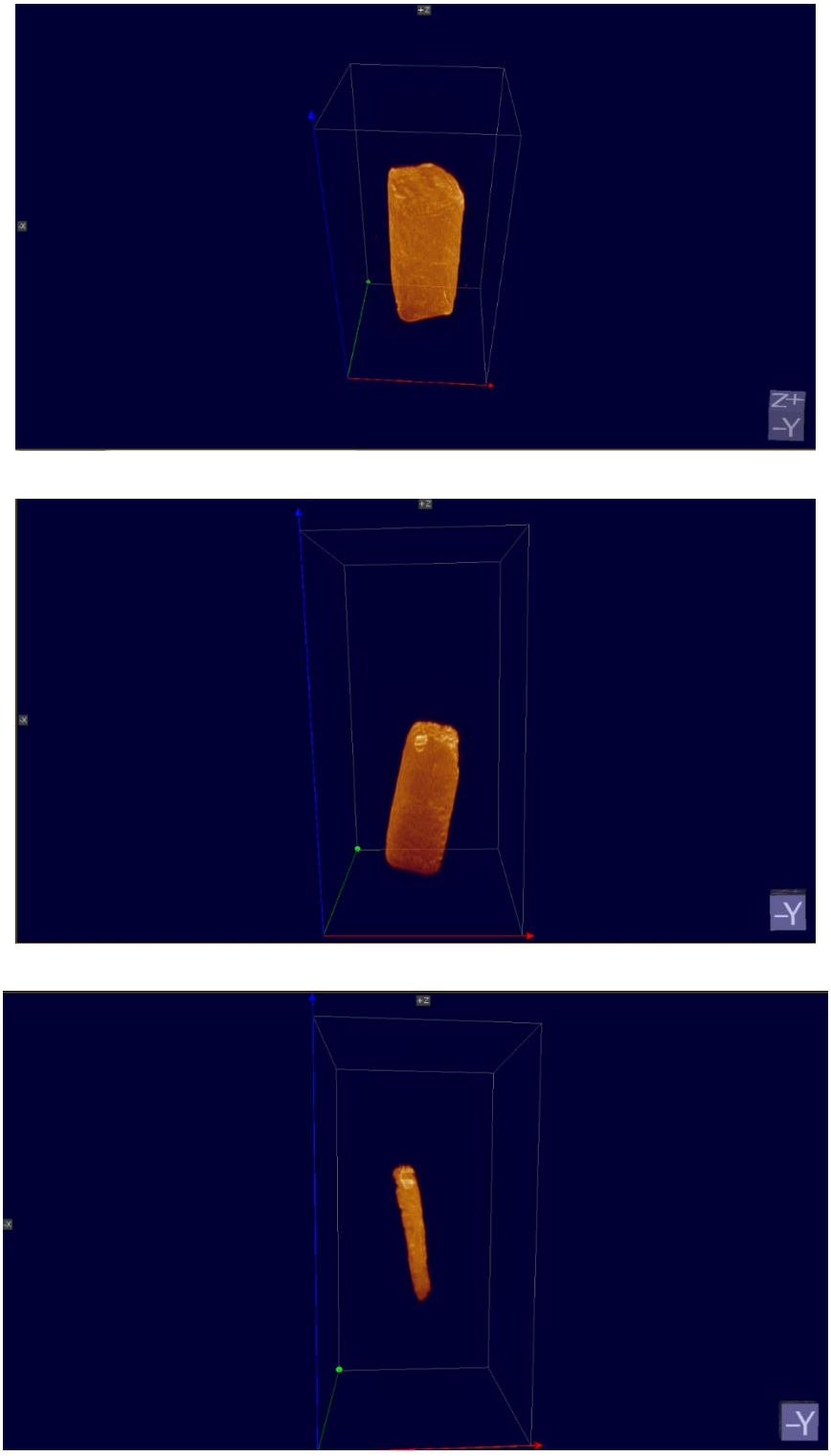

Figure 52 *3D images of fresh pumpkin sample and after 30 and 70 minutes at 60° C.*

As expected, the shape of the sample changes dramatically during dehydration. Shrinkage of samples has been observed for all drying temperatures, it increases with the volume of water removed, since the more the water is removed the more contraction stresses are originated in the samples [96].

Extracting wall plots from the data shown from Figure 47 to Figure 50, we obtain the plots illustrated from Figure 53 to Figure 56.

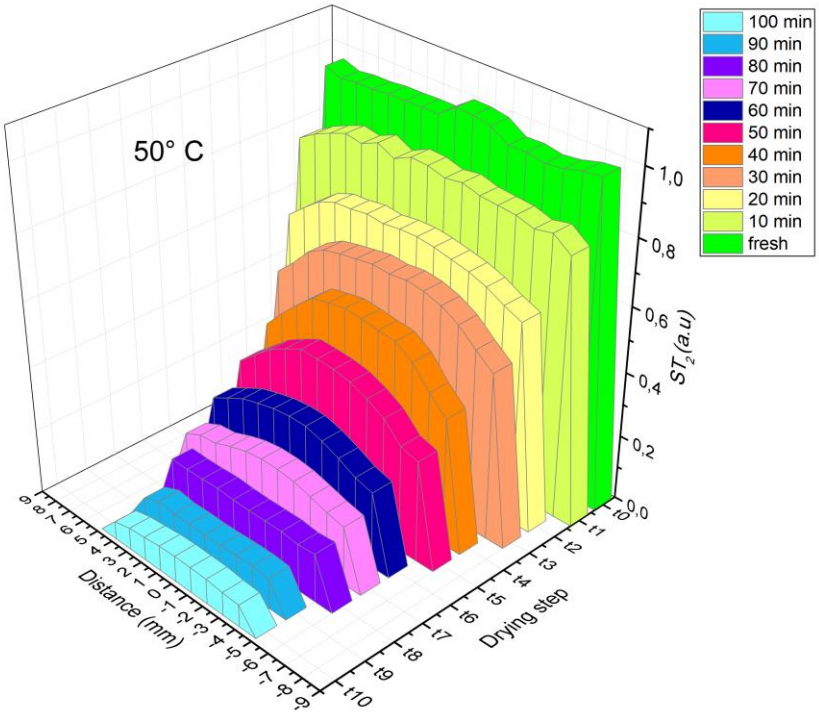

Figure 53 *Representation of moisture content extracted by MR T_2 data taken slice by slice for each drying step at 50°C.*

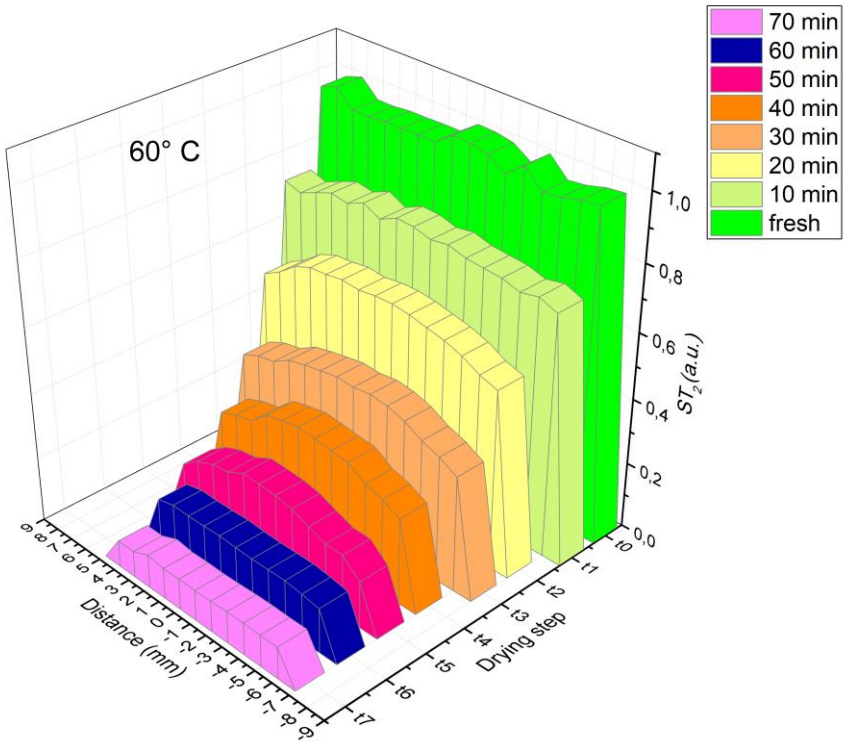

Figure 54 *Representation of moisture content extracted by MR T_2 data taken slice by slice for each drying step at 60°C*

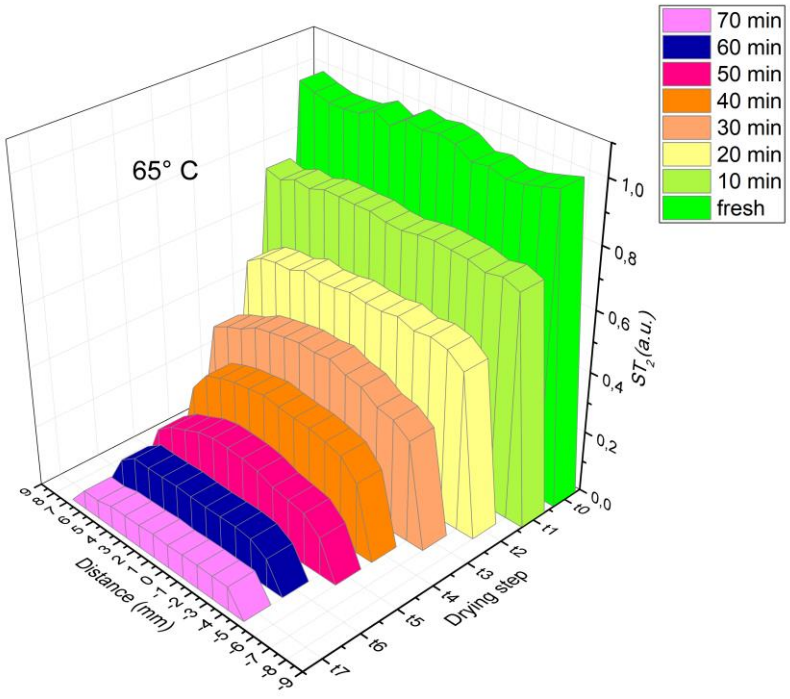

Figure 55 *Representation of moisture content extracted by MR T_2 data taken slice by slice for each drying step at 65°C*

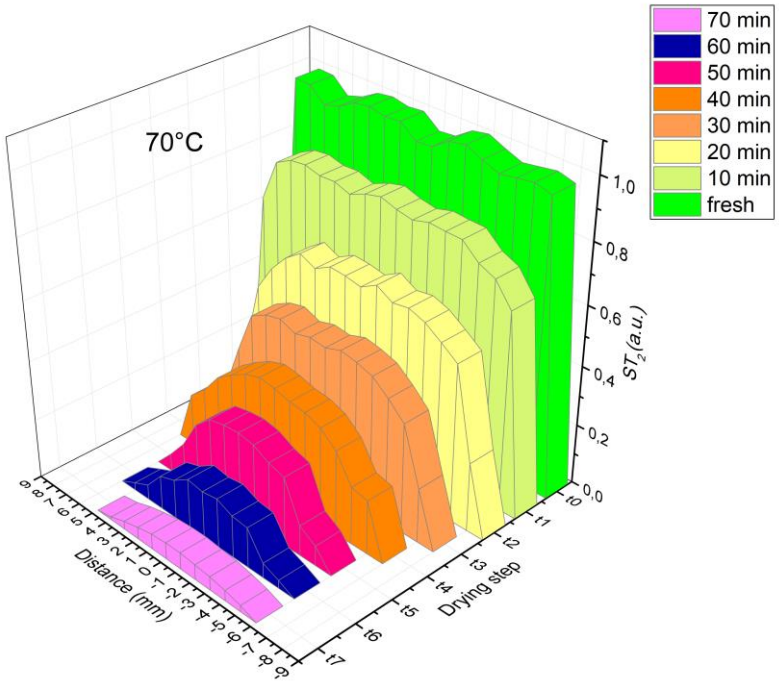

Figure 56 *Representation of moisture content extracted by MR T_2 data taken slice by slice for each drying step at 70°C*

These plots show in a clear and striking way the simultaneous loss of water and the reduction of the volume caused by the shrinkage of the sample during the drying process.

Figure 57 shows pictures of the real sample, respectively the fresh one in the left picture and, in the right picture, after few drying steps.

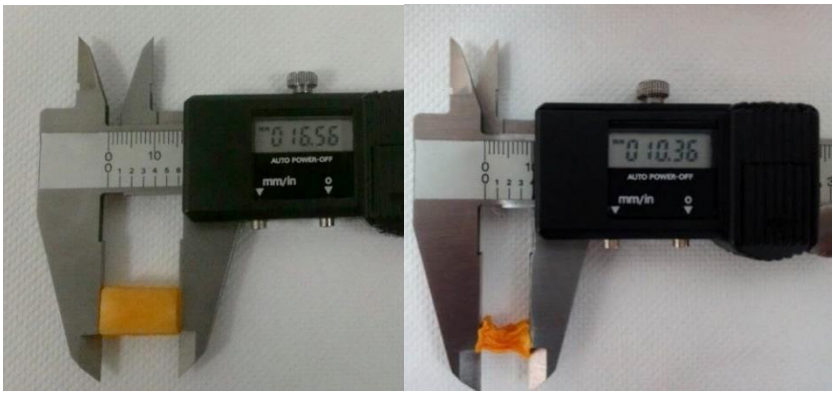

Figure 57 *Shrinkage of pumpkin sample during drying process.*

According to L. Mayor et al [97], shrinkage is more accentuated at mid-length and mid-thickness of sample whereas, at the edges, shrinkage is less pronounced. This effect, clearly observed in the most dehydrated samples, it is also clearly visible in Figure 57.

Eventually we have extracted, from each MR image collected during the study, the area of each slice.

Knowing that the thickness of each slice is 1 mm, we can easily calculate the volume of the sample at each drying step. The volume data obtained in this way are compared with the gravimetric measurements and with the ST_2 data obtained from MR T_2 maps at each drying step. The comparison is shown from Figure 58 to Figure 61, together with the data tables, where the agreement among the three physical quantities is remarkable for every drying temperature.

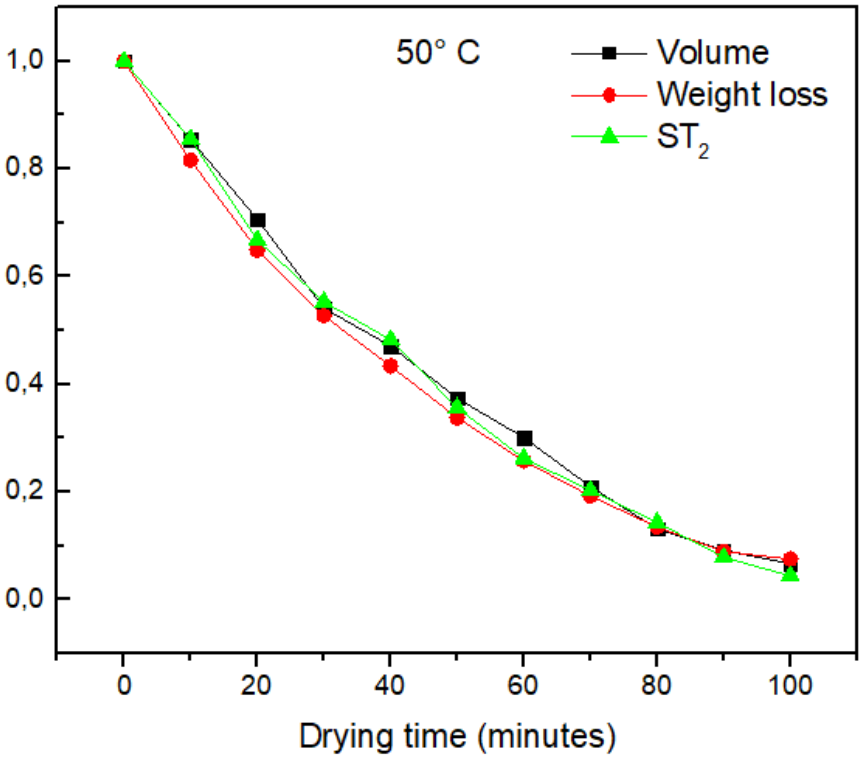

Drying time (50° C) minutes	Volume a.u.	Weight loss a.u.	T2 a.u.
0	1	1	1
10	0,85497	0,81596	0,85522
20	0,70612	0,64923	0,66718
30	0,54112	0,52707	0,55283
40	0,47112	0,43371	0,48229
50	0,37385	0,33735	0,35612
60	0,30055	0,25719	0,26187
70	0,20973	0,19212	0,20265
80	0,13105	0,13442	0,14284
90	0,09147	0,08914	0,07838
100	0,0661	0,07481	0,0435

Figure 58 *Volume shrinkage, weight loss and T_2 trends during dehydration and data values at 50°C.*

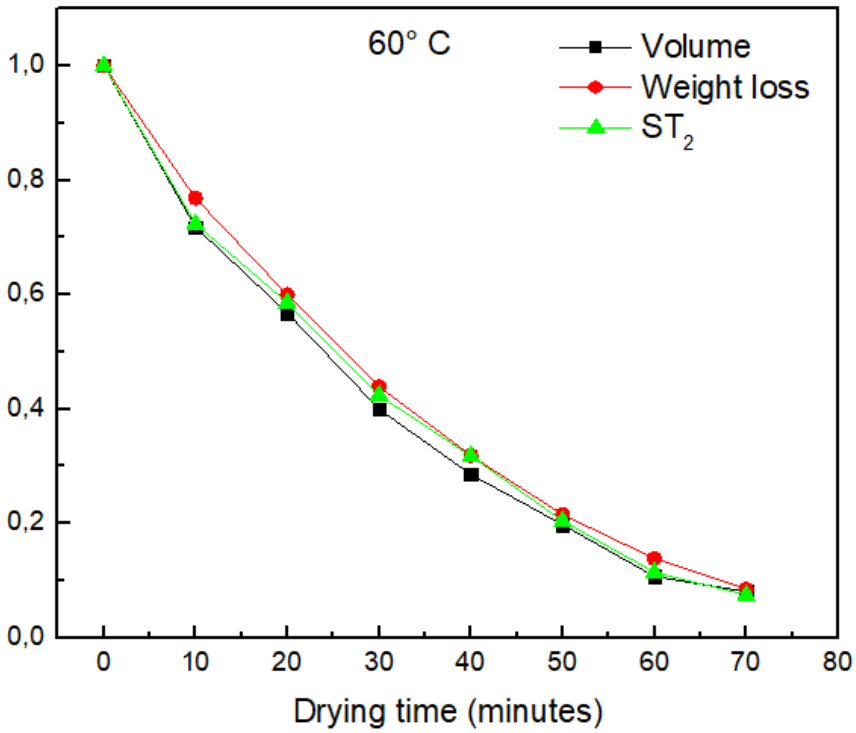

Drying time (60° C) minutes	Volume a.u.	Weight loss a.u.	T2 a.u.
0	1	1	1
10	0,71822	0,76871	0,72363
20	0,56809	0,59989	0,58586
30	0,39992	0,43933	0,42391
40	0,28582	0,31865	0,31798
50	0,1981	0,21569	0,20441
60	0,10725	0,1388	0,11461
70	0,08096	0,08538	0,07515

Figure 59 *Volume shrinkage, weight loss and T_2 trends during dehydration and data values at 60°C.*

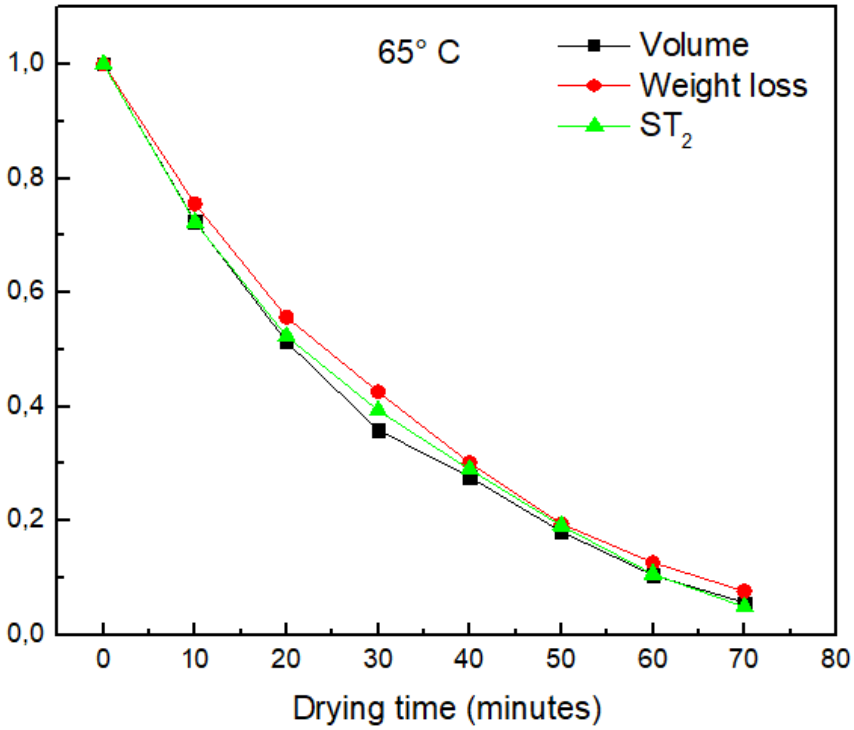

Drying time (65° C) minutes	Volume a.u.	Weight loss a.u.	T2 a.u.
0	1	1	1
10	0,72446	0,75544	0,72321
20	0,51352	0,55696	0,52333
30	0,35916	0,42598	0,39356
40	0,27708	0,30168	0,29016
50	0,1812	0,19472	0,19163
60	0,10531	0,1269	0,10666
70	0,05694	0,07697	0,0491

Figure 60 *Volume shrinkage, weight loss and T_2 trends during dehydration and data values at 65°C.*

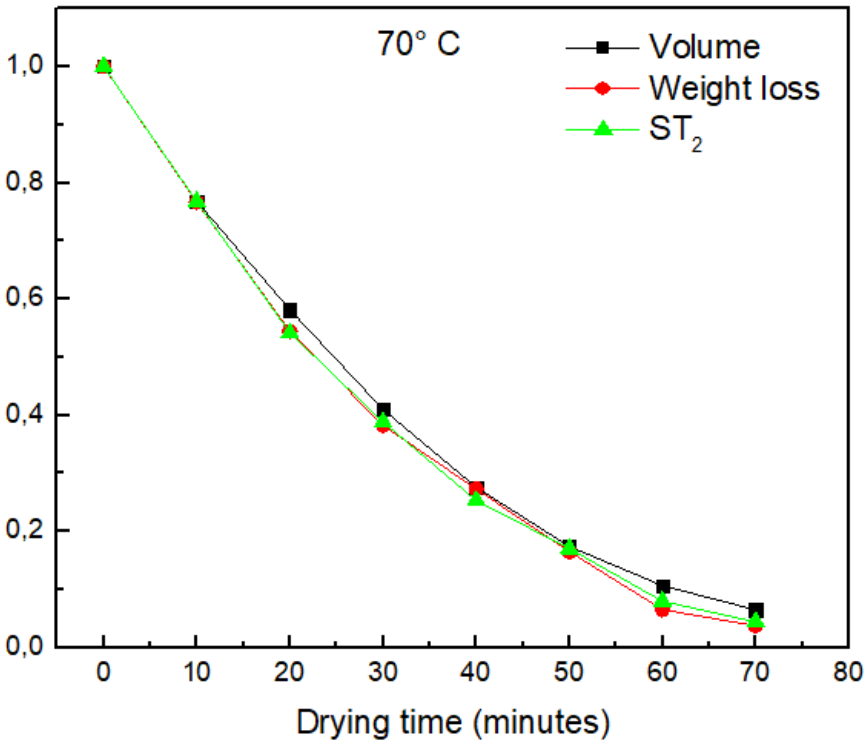

Drying time (70° C) minutes	Volume a.u.	Weight loss a.u.	T2 a.u.
0	1	1	1
10	0,76792	0,76664	0,76776
20	0,58187	0,54433	0,54167
30	0,40981	0,38264	0,38843
40	0,27599	0,27317	0,25325
50	0,17421	0,16516	0,17069
60	0,10692	0,06567	0,07985
70	0,06525	0,03763	0,04443

Figure 61 *Volume shrinkage, weight loss and T_2 trends during dehydration and data values at 70°C.*

The volume shrinkage during the drying process shows the same trend of the weight loss and of the decreasing of the ST_2 values.
The wall plots illustrated from Figure 53 to Figure 56, may be then considered as a representation of the real behaviour of the samples, in terms of moisture content and shape changes due to the shrinkage, during the drying process and they are obtained using exclusively MR T_2 data.

One of the main aims of this study will be to extend this method to different food matrices and validate this approach, which reveal to be suitable to investigate water contents and dynamics in biological samples under different conditions.

5.6 Spectra

The spectrometer (300 MHz/89 mm) gives us also the possibility to complement the imaging procedure with a local spectroscopy of the sample, performed voxel by voxel (Single Voxel Spectroscopy, SVS).
We have developed an alternative approach on the use of MRI technique to extract water content information, combining the imaging technique with spectroscopic data.
A significant advantage of this method is the relatively fast acquisition time, more or less 1 minute, with respect to the T_2 mapping that require more than 50 minutes. Collecting information in a short time represent a crucial point towards the development of a real-time and fast protocol to monitoring the drying process.
The analysis has been again performed on the pumpkin (*Cucurbita Maxima)*. The ea is the same described in the section 5.4. The sequence that allows this kind of approach is the PRESS sequence, described in the section 2.3, which is used for the localized ^{1}H-MRS.
Before the measurement, the automatic shimming procedure, B_0 MAP, is used to achieve optimal uniformity of the magnetic field across the voxel volume.

The shimming allows us to adjust the homogeneity of the static magnetic field B_0 by changing the currents through the shim system (a set of field gradient).

The FID signals are Fourier-Transformed, and the phase and the baseline of the spectra are corrected using the Bruker software TopSpin. The PRESS sequence has been used used with the following parameters *TR = 3500 ms, TE = 17 ms.*

Remembering that for the pumpkin the percentage of water is higher than 90%, the local spectroscopy returns mainly a significant peak corresponding roughly to the water contribution.

The integrated intensity of a signal is a measure of signal strength and is determined by integrating the area under the signal peak.

The Figure 62 below shows the spectrum of the pumpkin sample obtained as described above. It clearly appear the main contribution of the water peak at 4.7 ppm.

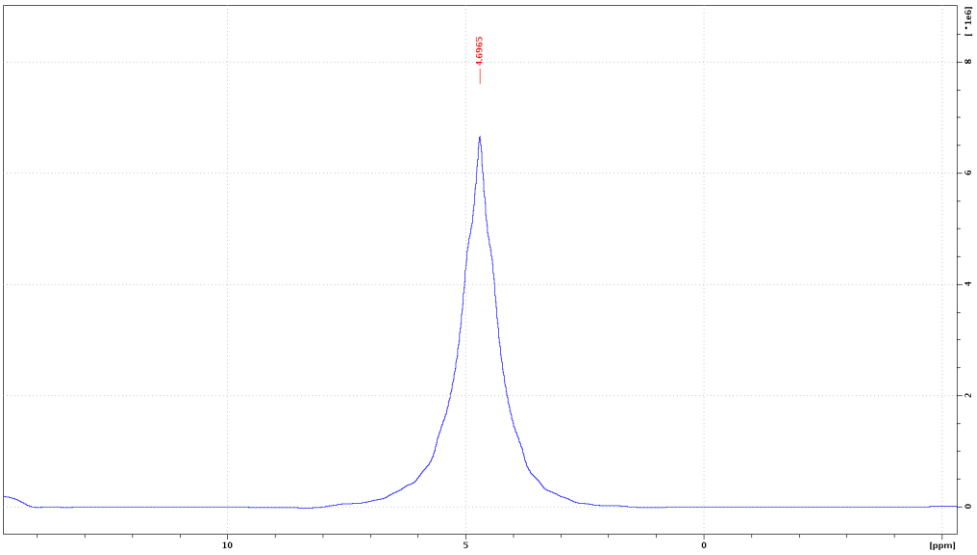

Figure 62 *NMR spectrum of pumpkin sample.*

Since the signal intensity is proportional to the proton density, it is possible to compare the decreasing of the area under the signal peak with the loss of water.

To evaluate this area, it is needed to take into account the receiver gain (RG) value. This parameter characterizes the amplification of the signal coming from the sample. RG is adjusted automatically and it change for each measurements.

An advantage of this approach is that the starting point is the image and the sample preparation in this case is easy, non-invasive and absolutely non-destructive, so it does not have the drawbacks of the common spectroscopy. On the other hand, the resolution is lower and below the “water peak” there are certainly other contribution, which we consider anyway very small. After all, if we have in mind to evaluate the total water contribution this method appear to be very promising. The plots below show the moisture ratio of samples (in percentage) during drying, obtained by gravimetric method (black squares) and MRI spectroscopy values, extracted for each temperature (red squares).

In the comparison, the agreement between data is very high with r^2 value usually higher than or very close to 0.99.

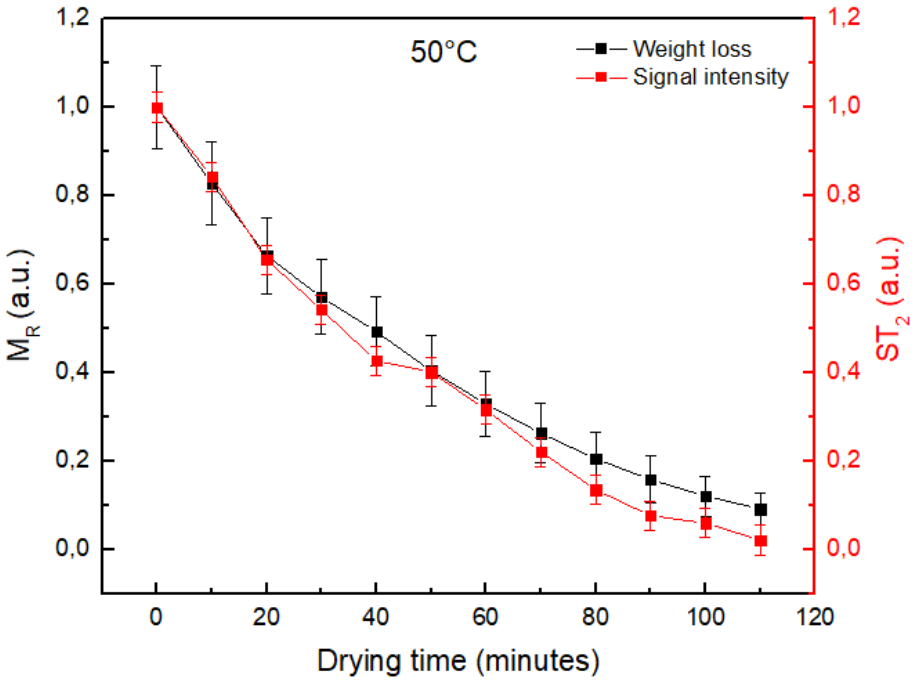

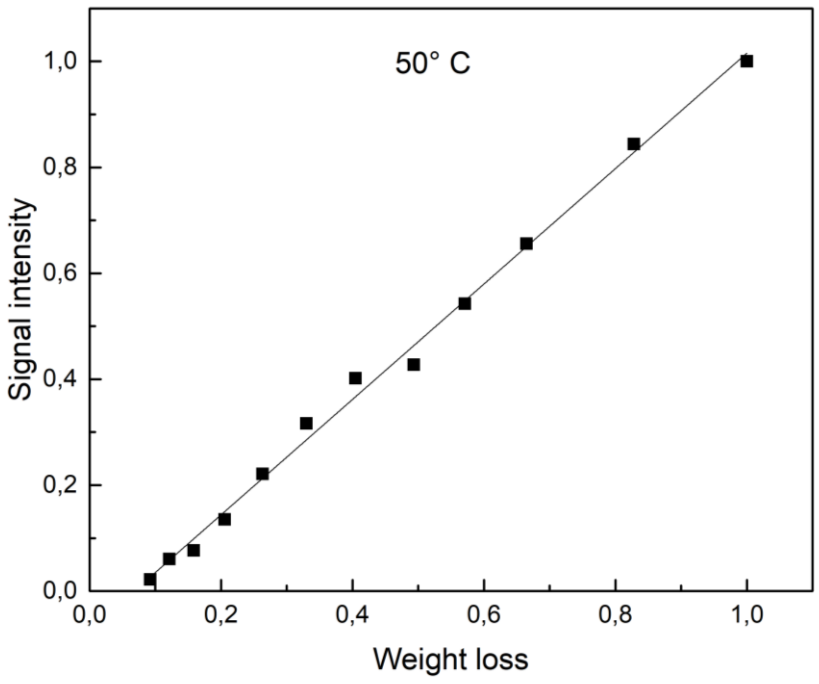

Figure 63 *Weight loss of samples during drying obtained by gravimetric method compared with the signal intensity obtained by local spectroscopy, at 50° C (r^2=0,995).*

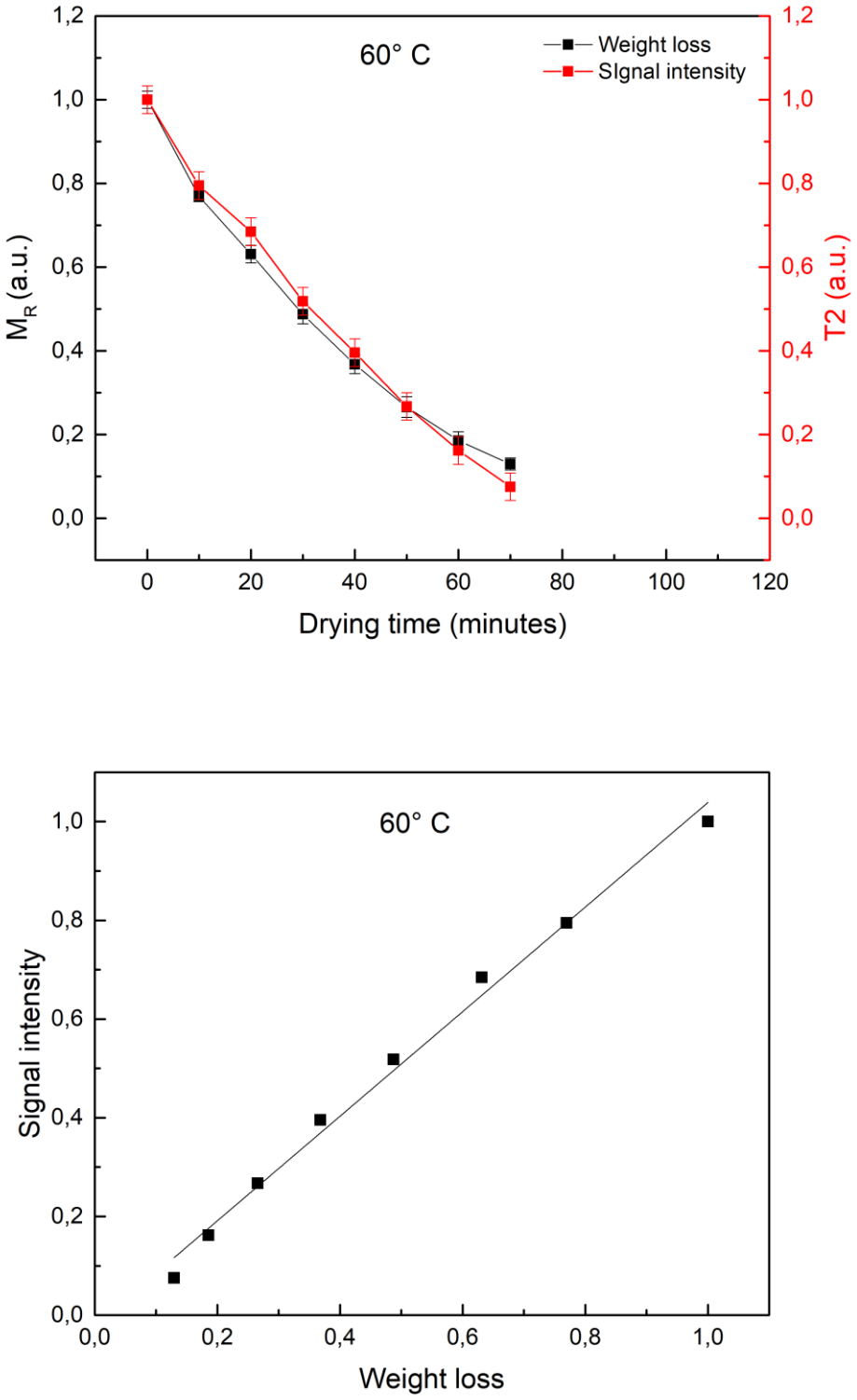

Figure 64 *Weight loss of samples during drying obtained by gravimetric method compared with the signal intensity obtained by local spectroscopy, at 60° C (r^2=0,990).*

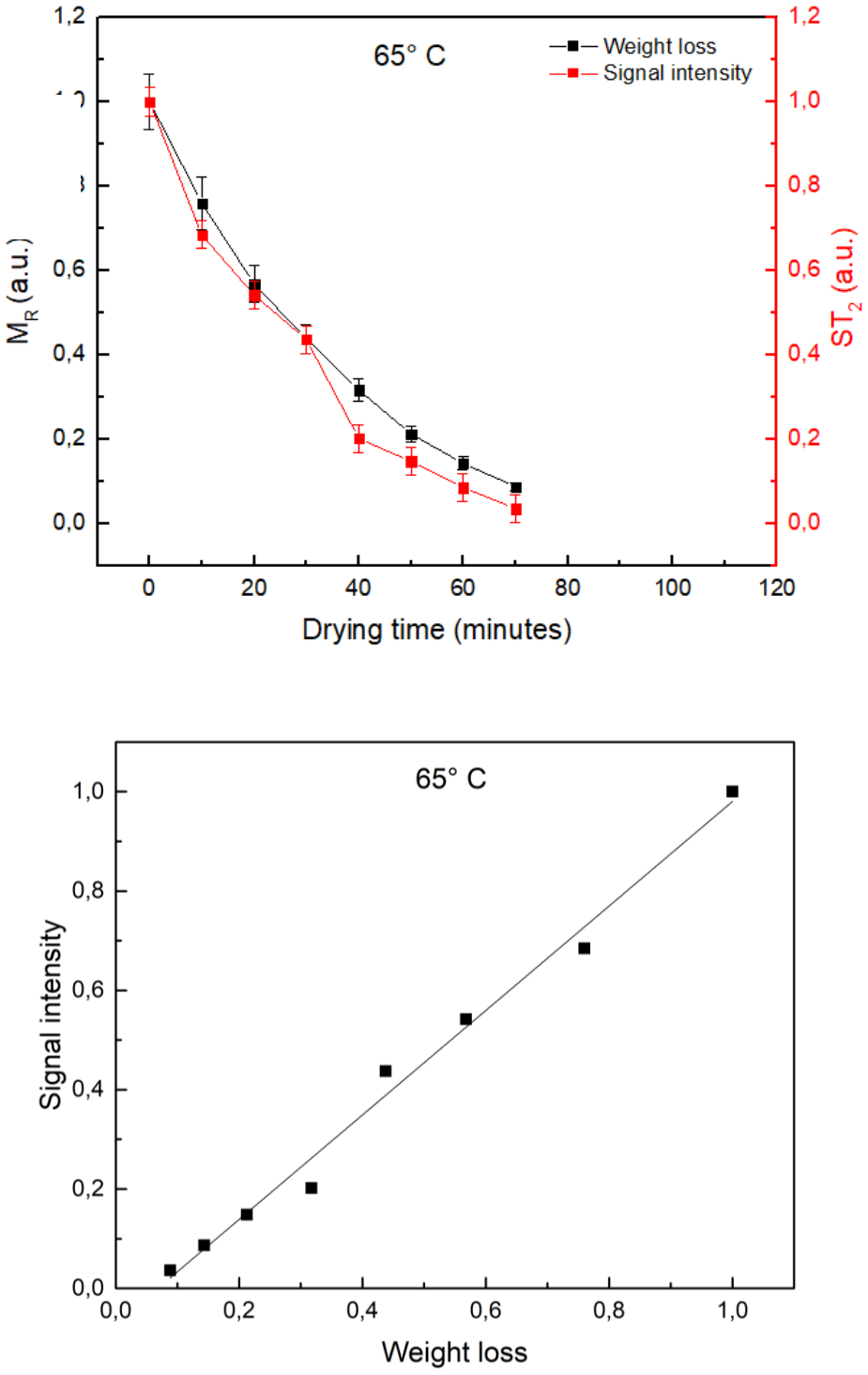

Figure 65 *Weight loss of samples during drying obtained by gravimetric method compared with the signal intensity obtained by local spectroscopy, at 65° C (r^2=0,987).*

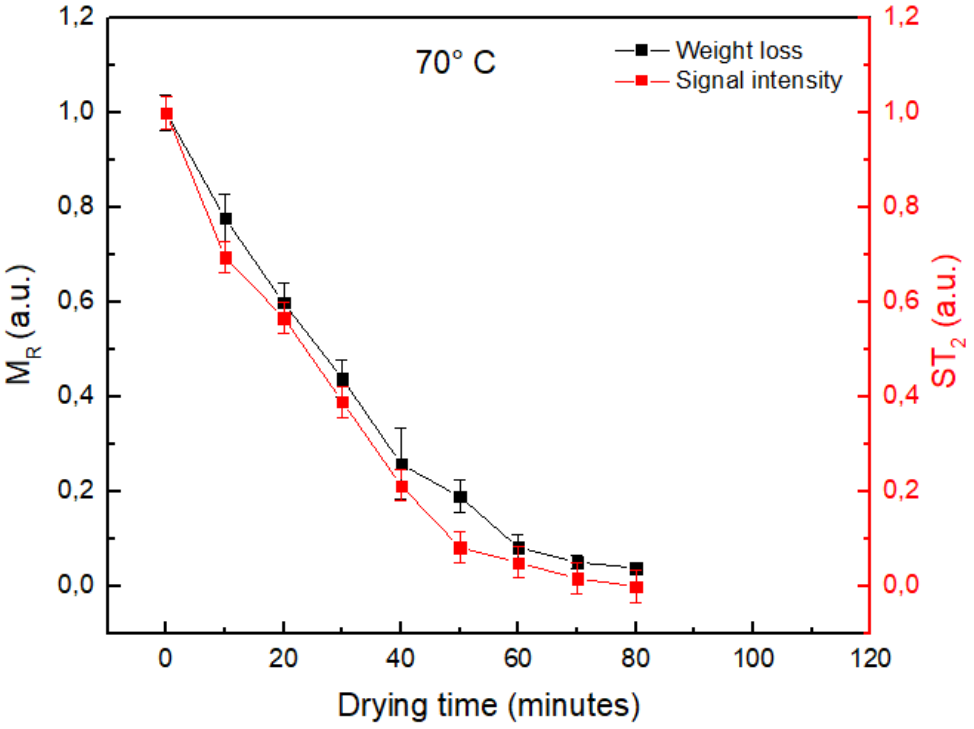

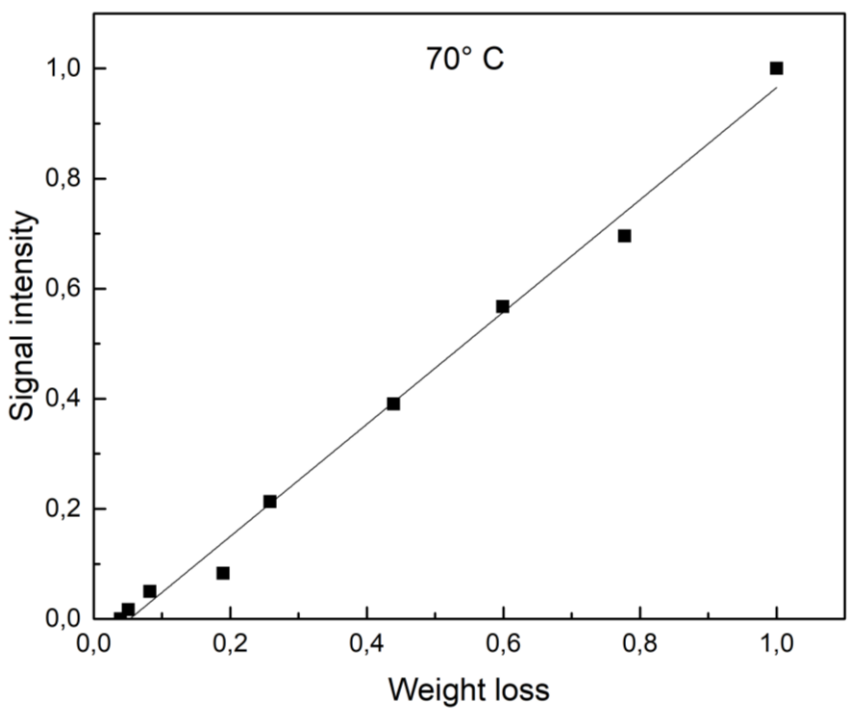

Figure 66 *Weight loss of samples during drying obtained by gravimetric method compared with the signal intensity obtained by local spectroscopy, at 70° C (r^2=0,991).*

As seen in the previous section (5.5), to allow a comparison within the same range of the MRI data, a selection on the gravimetric data has been done, excluding the gravimetric measurements characterized by very low water contents, which are unable to provide measurable T_2 signals through NMR.

It is evident that the NMR signal coming from the sample is measurable up to 110 minutes at 50°C (the lower drying temperatures) and up to 70 minutes for 60°C and 65°C. For 70°C (the higher drying temperature) the T_2 signal become too small after 80 minutes of drying process.

We should expect that the time decreases as the temperature increases. Referring to the Figure 66, the points corresponding to 70°C show a measurable T_2 signal at greater time with respect to the ones at 60°C and 65°C. This could be ascribed to the slicing procedure since the fresh sample used for the 70° C measurements has been moulded in a volume slightly bigger with respect to the other samples.

To understand the effectiveness of this method, we have compared the weight loss trend with both the ST_2 data shown in the previous paragraph and the spectra data. The comparison highlights, despite of the roughness of the spectra method and the necessary refinement and validation, a remarkable agreement (r^2>0.99).

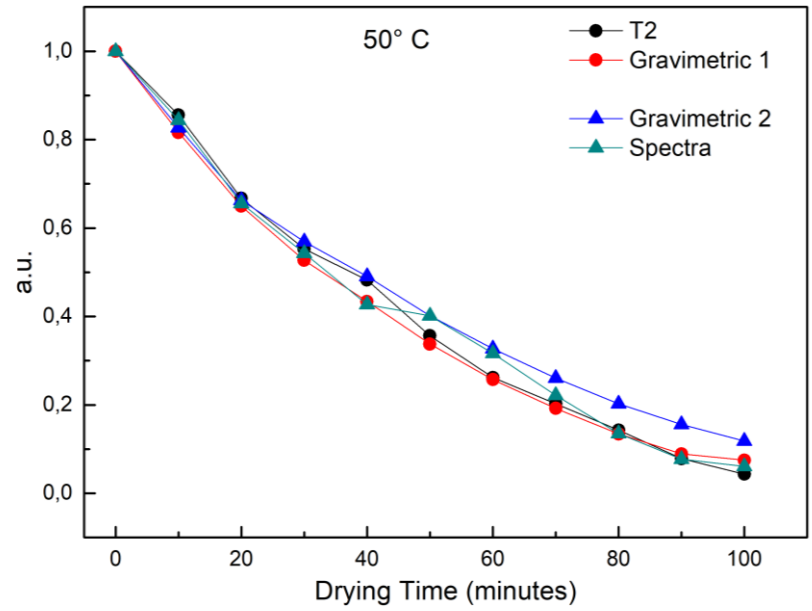

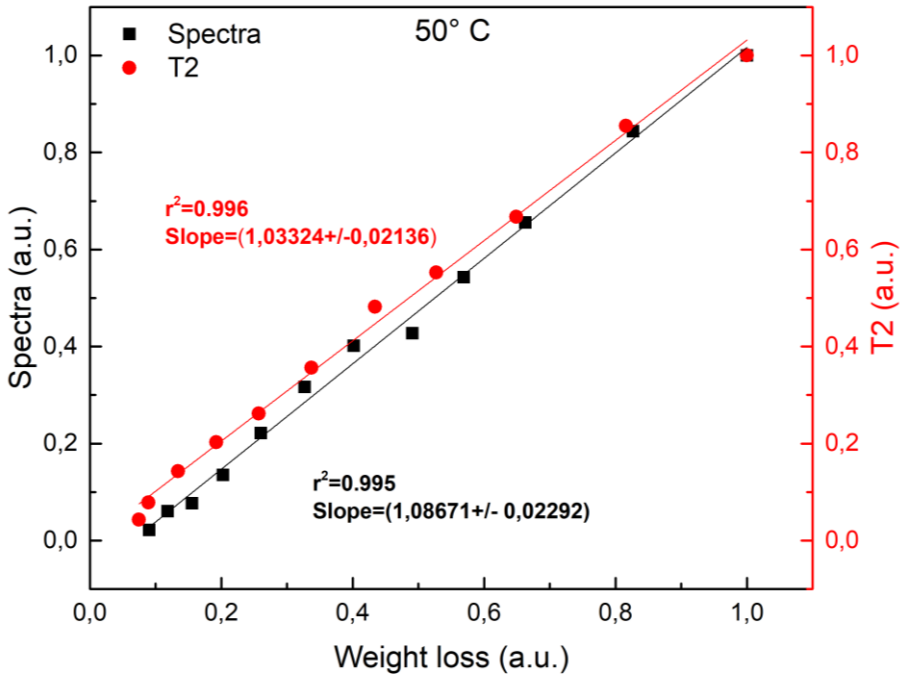

Figure 67 *Comparison between the gravimetric weight loss trend and both the T_2 and the spectra data at 50°C.*

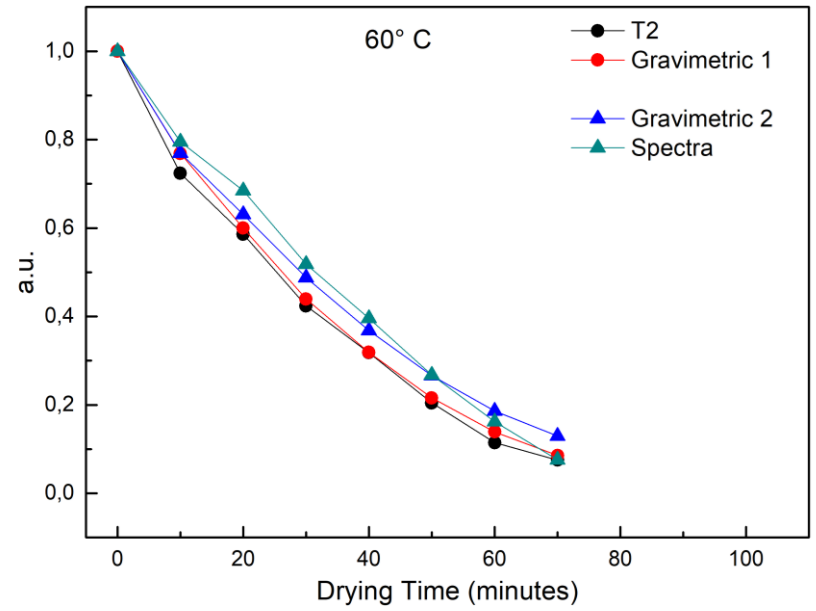

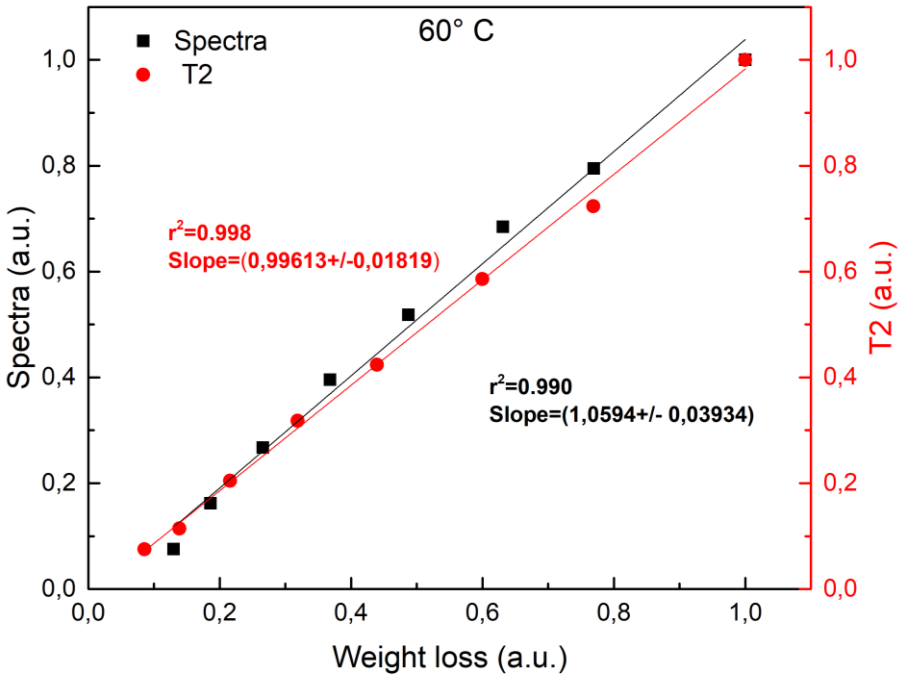

Figure 68 *Comparison between the gravimetric weight loss trend and both the T_2 and the spectra data at 60°C.*

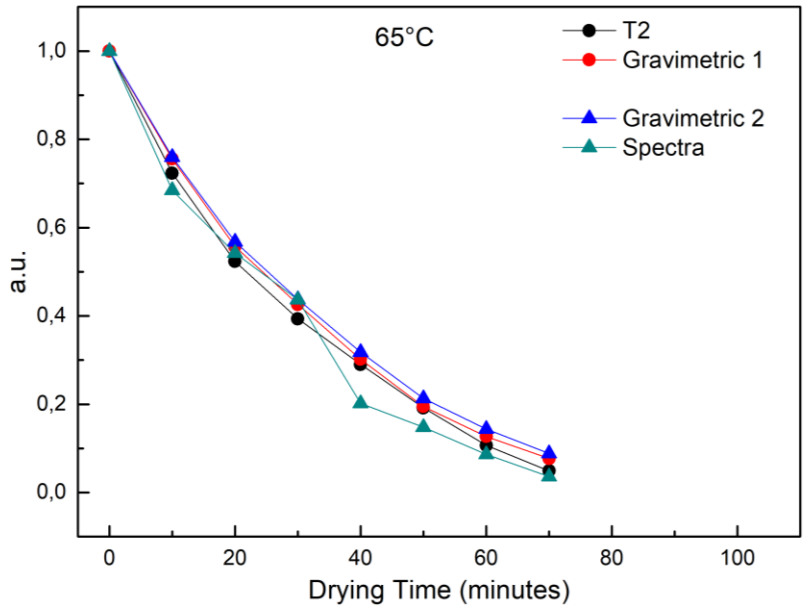

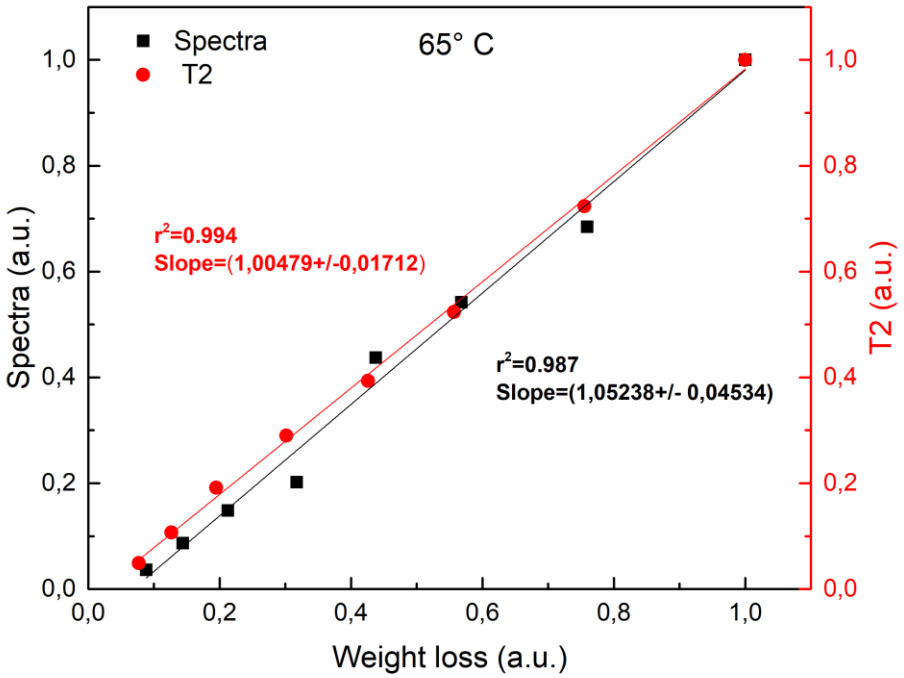

Figure 69 *Comparison between the gravimetric weight loss trend and both the T_2 and the spectra data at 65°C.*

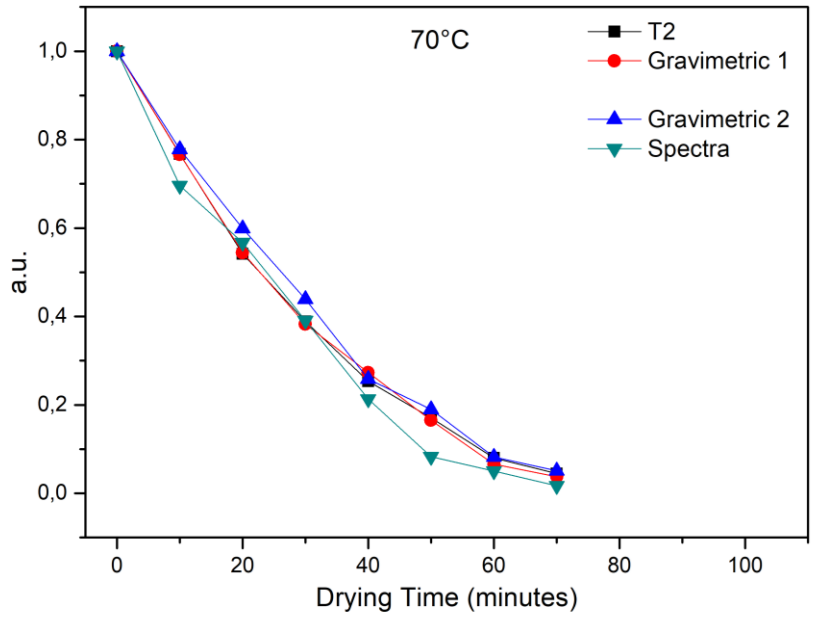

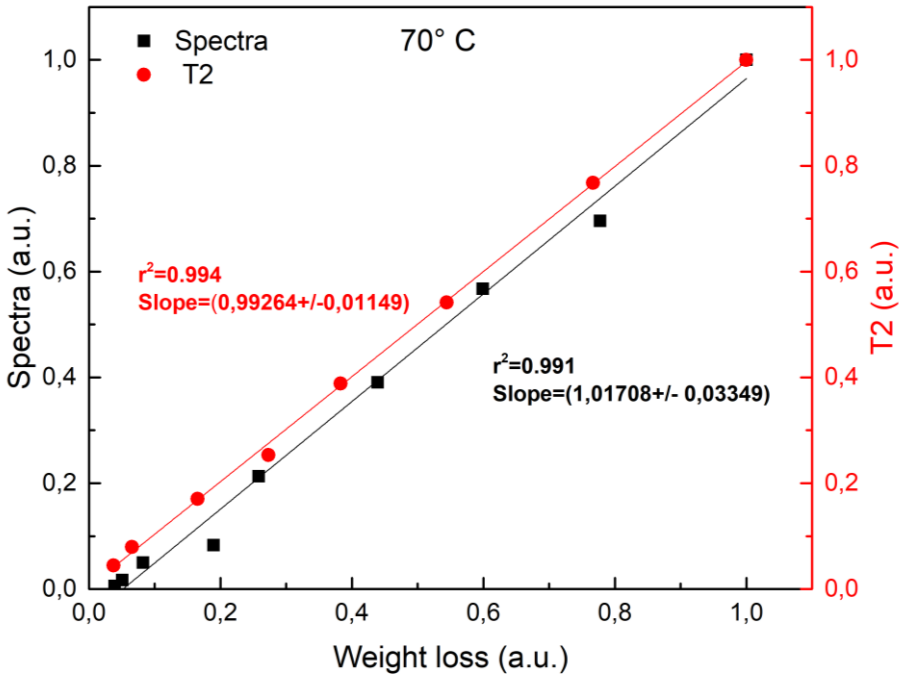

Figure 70 *Comparison between the gravimetric weight loss trend and both the T_2 and the spectra data at 70°C.*

All the advantages of the MRI mentioned in this chapter can be really useful also for the study of living plants. Also plants are rich in water and through MRI it is possible to extract information within the images and use them to study the dynamics of water uptake in a plant and water transport in the stem [98], in particular as a function of changing environmental conditions.
This topic will be treated in the next chapter.

6. MRI of plants

By permitting non-invasive and in vivo monitoring of the whole plants, MRI has become a powerful tool in the studies on living plants.
The potential for investigating root viability using NMR micro imaging is an increasingly technique widely used in the last two decade (section 4.4).
Coming from the water protons, that are naturally present in plants, the MRI signal can be analysed under realistic environmental conditions.

6.1 Roots water uptake

The idea for the current experiment, for which we are still developing the technique, is to follow the growing of a plant from the initial state as seed to the complete development, observing each step of the growth through MRI.
In particular, the aim is the monitoring of the process of absorption from the roots, focusing on the differences, which can be highlighted by the MRI, between the absorption process from a "safe" soil and a contaminated one.
Nowadays, an emerging method that uses living plants to uptake, store and degrade contaminants is the *phytoremediation* [99] [100] [101]; it is a new evolving field of science and technology where the MRI can play a significant role.

Plants are used to extract, and/or detoxify pollutants. This technique is widely viewed as the ecologically responsible alternative to the environmentally destructive physical remediation methods currently practiced, such as physically removing contaminated soil from a site and burying it elsewhere, that are generally too costly and environmentally destructive to be widely applied (i.e.: thermal desorption, excavation and dredging).

The interplay between root activity and soil function influences the plant growth and productivity and results difficult to be observes because of the natural position of the roots underground and the complexity of the root system architecture [102].

Another interesting aspect concerns the contamination by metals: plants can be used either to stabilize or remove metals from the soil and groundwater [103][104][105]. The combination of local NMR spectroscopy and 2-3 D imaging and their feature to be non-invasive and non-destructive give the possibility to have an overall view of the process. The possibility to reproduce the conditions closest to the real process can render unexpected insights to achieve a better understanding of contaminant absorption.

MRI has just been successfully applied to investigate temporal and spatial water uptake and distribution in germinating lupine [106] and tobacco seeds [107], to define the water content changes due to root water uptake in *ricinus* roots [108], to monitor the water uptake of loblolly pine [109]. D. van Dusschoten at al. have done a quantitative 3D analysis of plant roots growing in soil [110], demonstrating that MRI can be used for non-invasive imaging of roots grown in relatively large (up to 8.6 L) soil-filled pots.

The study of the interactions of plant and roots has also been analysed combining MRI technique with neutron imaging [111]. Dry or fully imbibed seeds of western white pine were studied using high-resolution MRI [112]. MRI has also been used to study the water uptake and distribution in soybean seeds during hydration [113], in bean embryos during ethylene induced precocious germination [114]. It has been shown that MRI can provide the water mobility detection [115] and is able to measure plant trait in the soil [116].

Definitively, MR imaging is a versatile protocol to investigate, non-invasively, plants and roots performance.

6.2 Experiment

The method to be developed has to be simple, using reagents compatible with the environment and replicable in other laboratories.

The study will concern the growing of a plant born respectively in a safe (agar[1] + H_2O) and infected soil, monitoring the development of the root system over the time by MRI.

Maize seed *(Zea Mays)* have been chosen to conduct the experiment. The literature shows that Zea Mays is a good candidate for phytoremediation [117]; it results useful for the remediation of soil contaminated with atrazine, an herbicide. Residues of atrazine were reduced in faster rate in contaminated soil planted with Zea Mays than the unplanted soil.

Other studies show how Zea Mays is a good choice for remediation of soil contaminated with petroleum [118] and heavy metals such as cadmium [119].

The contamination will be studied respectively through different processes of:

- contamination of the soil at the time of sowing
- contamination after a suitable time (i.e.: after one week)
- contamination on an adult plant.

To start the experiment the pentahydrate copper sulphate ($CuSO_4 \cdot 5H_2O$ - 2500 ppm) has been chosen. The $CuSO_4$ is the most common copper salt because of its stability; at room temperature, it looks like a blue crystal. It is soluble in water and it can be used as herbicide, fungicide and pesticide. Copper in $CuSO_4$ binds to proteins and damages the cells causing them to leak and die. Copper can kill snails, disrupting the normal function of the skin cells and enzymes [120][121].

Additional test will be carried out with the Oxadixyl ($C_{14}H_{18}N_2O_4$) and 2,3,7,8-Tetrachlorodibenzo-P-dioxin ($C_{12}H_4Cl_4O_2$).

[1] Agar is commonly used to help feed microorganisms such as bacteria.

The idea is also to improve the analysis to apply the protocol on samples of soil taken from an area comprises between the provinces of Napoli and Caserta, the so-called “Terra dei fuochi (Lands of Fires)”. Unfortunately, this area has suffered environmental degradation and contamination due to illegal dumping of toxic and hazardous waste. This area has been used as a gigantic landfill by criminal organizations where burn every toxic waste. This is the reason of its name. The obvious consequence are the soil and air contamination [122].

MRI protocol

NMR experiments were recorded using the Bruker 300 MHz/89 mm spectrometer. We have acquired T_2 and T_1 maps, Single voxel spectroscopy and 3D images.

Similarly to the process scheme followed for the pumpkin T_2 map, to evaluate the best TR, the MSMEVTR_8e_8r sequence has been used on seeds.

The time constant T_1 through MSMEVTR is carried out from the ISA analysis tool. The value obtained is about T_1= (406 ± 23) ms. As said, the better choice is to set a TR five time bigger than T_1 in order to assure the complete longitudinal relaxation.

The sequence used to produce the T_2 map is again MSME with the following parameters: TR = 2100 ms and TE from 5 ms to 100 ms, matrix size = (256 x 256). The FOV has been chosen to cover the whole sample according to the seed development.

To obtain a T_1 map, IR sequence has been used. This mapping consists in a series of IR sequences varying the TI (see section 2.3.2). The parameters used are the following: TR from 380 ms to 15000 ms (8 repetitions) and TE from 6.5 ms, matrix size = (256 x 256). Also in this case the FOV has been chosen to cover the whole according to the seed development.

The localized ^{1}H-MRS has been done on the seeds using the PRESS sequence as just explained previously (section 2.4). This sequence uses one 90° pulse and two 180° pulses to detect a spin echo from the localized volume.

Using T_1 mapping with IR it is possible to achieve an exceptionally good image contrast. In T_1 weighted image there is a strong dependence on the TR value.

Choosing a short TR, the image contrast will depend on the differences in longitudinal magnetization recovery (T_1), but if TR is too short, the T_1 could be not measured correctly. Usually the TR must always be at least five times the longest T_1 present to relax after the 90° pulse.

T_1 is strongly dependent on the magnetic field strength. Although it may be extrapolated to other field strengths based on theoretical predictions, such results will have significant uncertainties.

The Bruker software calculates T_1 through the ISA function:

$$Y = A + C \times \left(1 - exp\left(-\frac{t}{T_1}\right)\right), \tag{46}$$

where A is the absolute bias and C the signal intensity.

It process the data like explained in the section 5.5 for the T_2-mapping.

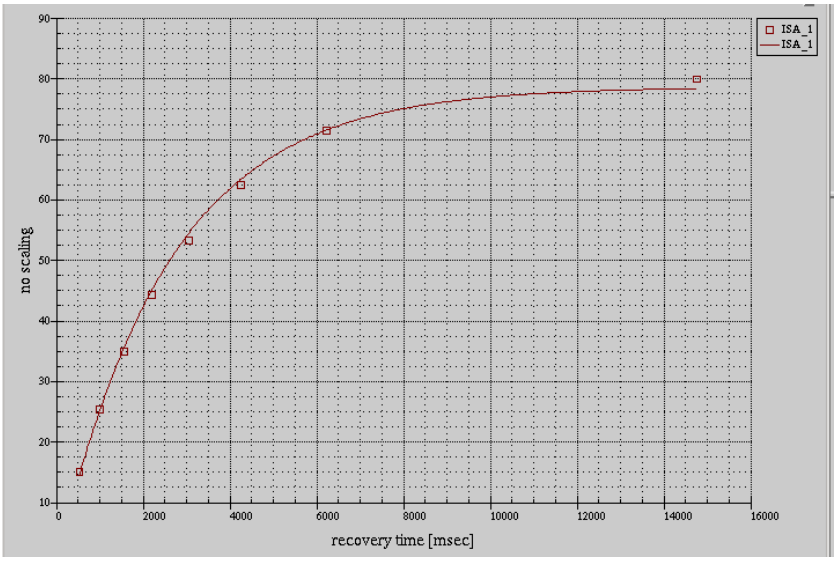

Figure 71 *Envelope of the spin-echo peaks decays exponentially with T_1 obtained with ISA Tool.*

Finally, we acquired 3D images in order to collect more information about the microstructure of roots (see next section).

6.3 First preliminary results

Lentils

To set the appropriate imaging parameters, trial measurements have been performed first on lentils.

Two common lentils (A and B) were placed in the test tubes (diameter 1.5 cm) on hydrophilic cotton wet with water. One of these, sample A, was chosen to MRI analysis, inserted in the probe and left inside for five days.

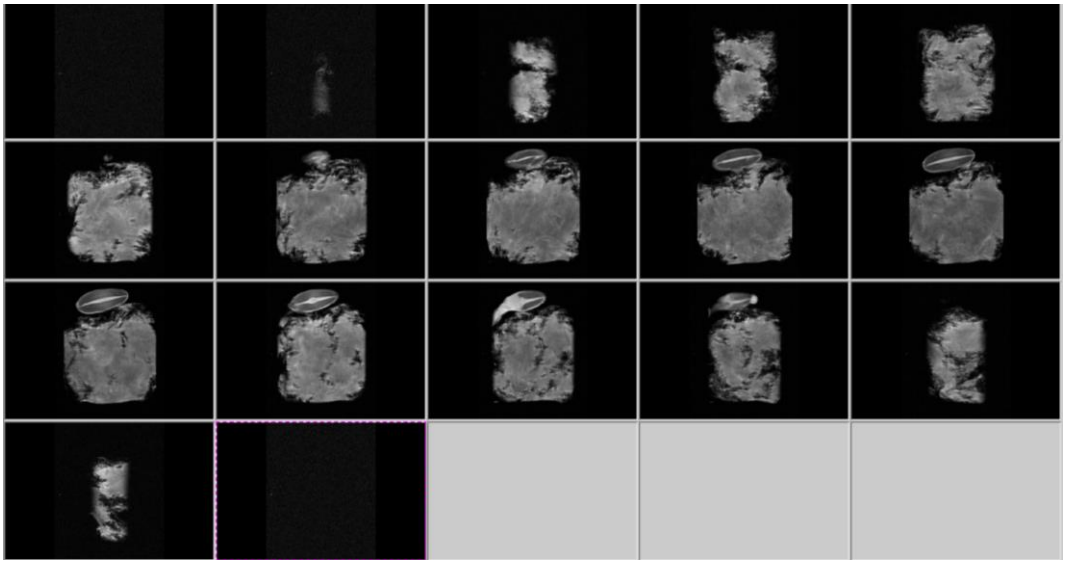

Figure 72 *2D images of lentil A.*

In these initial conditions, the result was not very satisfying, because the poor quantity of water that easily evaporated from the cotton and the absence of light did not allow a good growth.

Figure 73 *Lentil A after 5 days.*

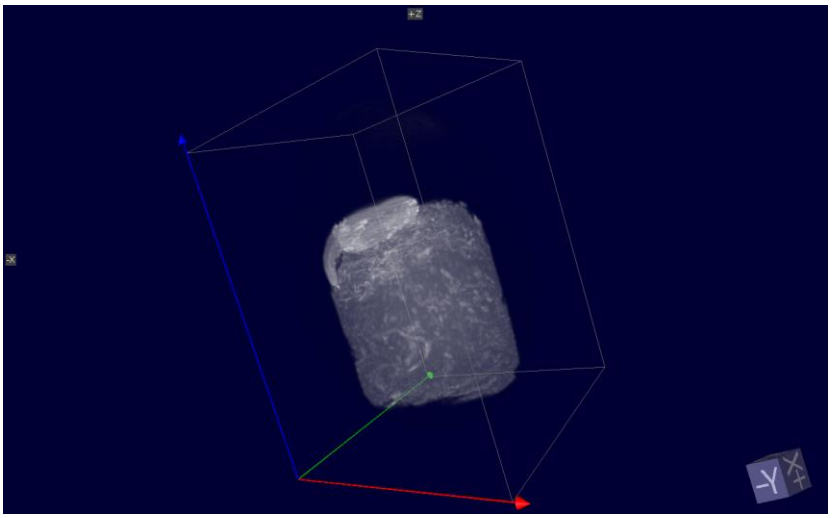

Figure 74 *3D image of lentil A.*

The second lentil (B), which had been left growing up in the lab, out of the spectrometer, has shown a better result as shown in Figure 75 and Figure 76.

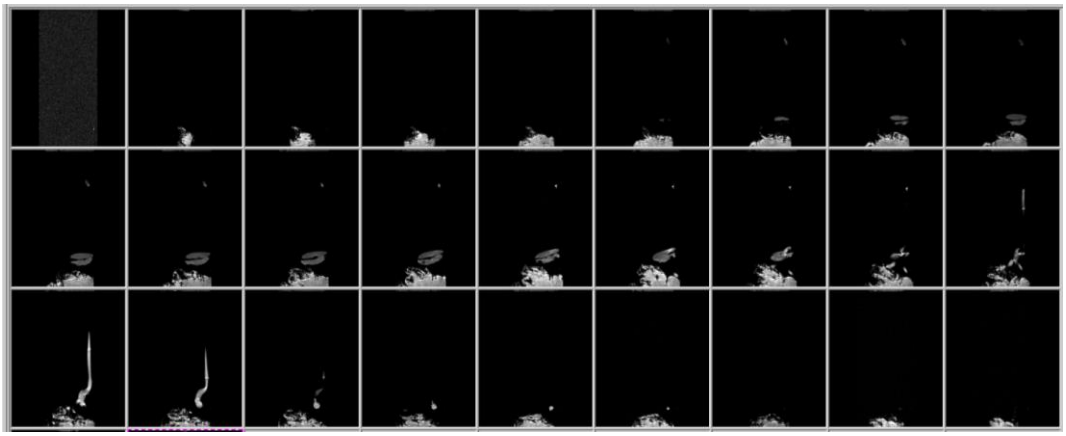

Figure 75 *2D image of lentil B after a week.*

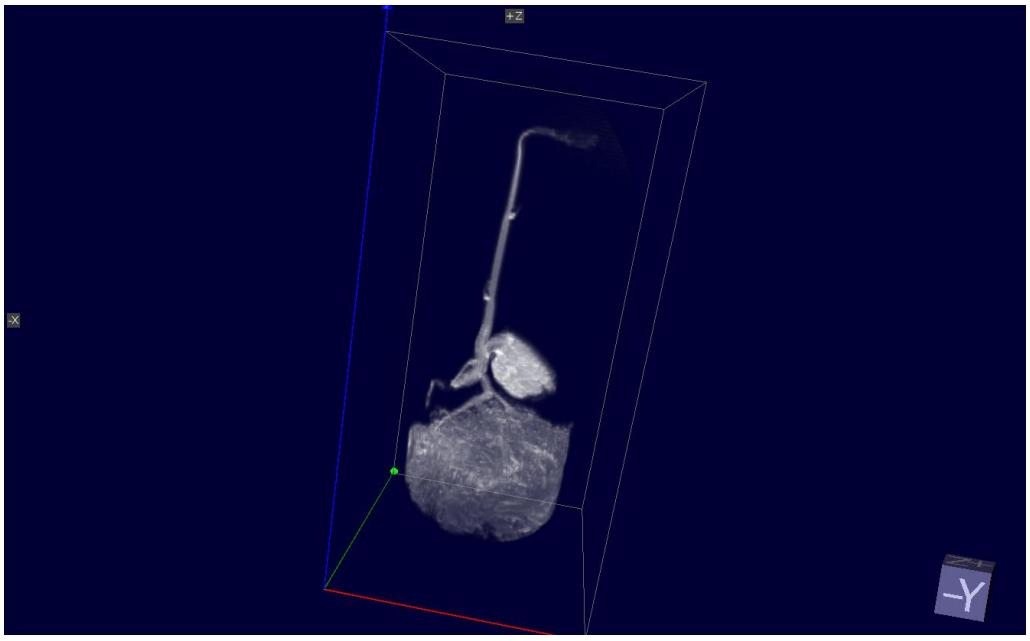

Figure 76 *3D image of lentil B after a week.*

After this preliminary study on lentils, to performed the method feasibility and set the convenient parameters, the seed chosen for the experiment has been the maize.

Maize

Tanned maize (*Zea mays*) seeds have been undertaken to the same procedure used for lentils, but they have been previously kept soaked in water for 12 hours.

At the beginning, the seed was put on the hydrophilic cotton and then, in order to improve the growing conditions, the hydrophilic cotton has been replaced with a solution of agar (1 g) mixed with water (99 g) to obtain a 1% solution.

To sterilize the solution, it has been put for 20 minutes at 120°C in an autoclave (mod Asal 760). Five maize seeds were placed in five test tubes (diameter 1.5 cm- Figure 77). One of these has been inserted in the probe for MRI measurements and left there for several days. At the same time, the remaining seeds have been left growing outside.

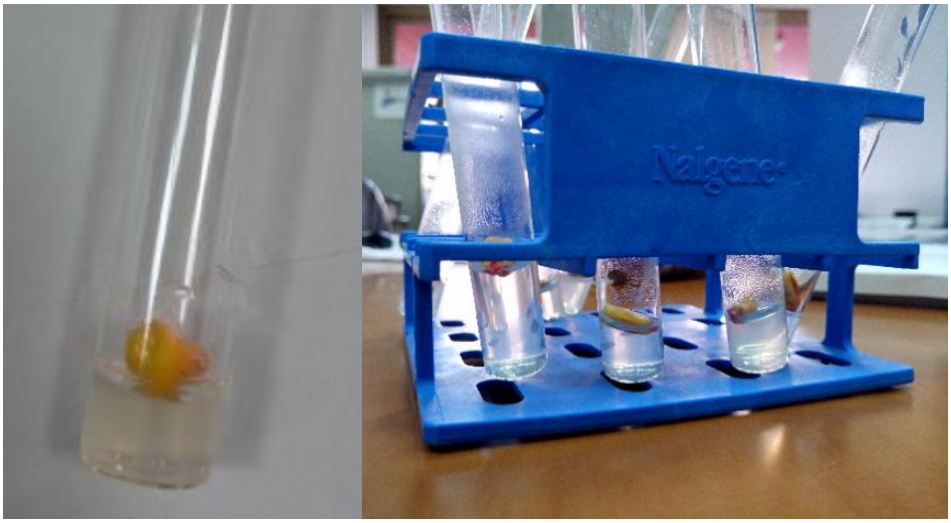

Figure 77 *Maize seeds in the tube test filling with agar and water.*

The first 2D images acquired are shown below (from Figure 78 to Figure 83):

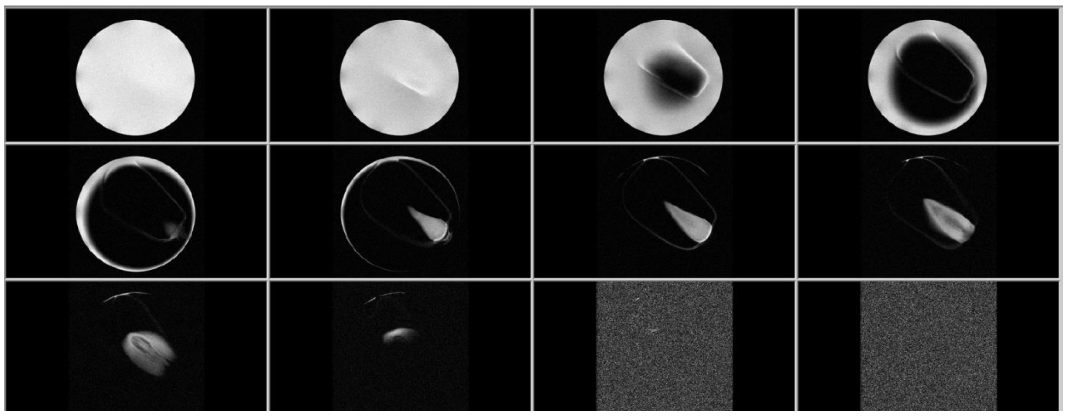

Figure 78 *Axial T_1 weighted image first day.*

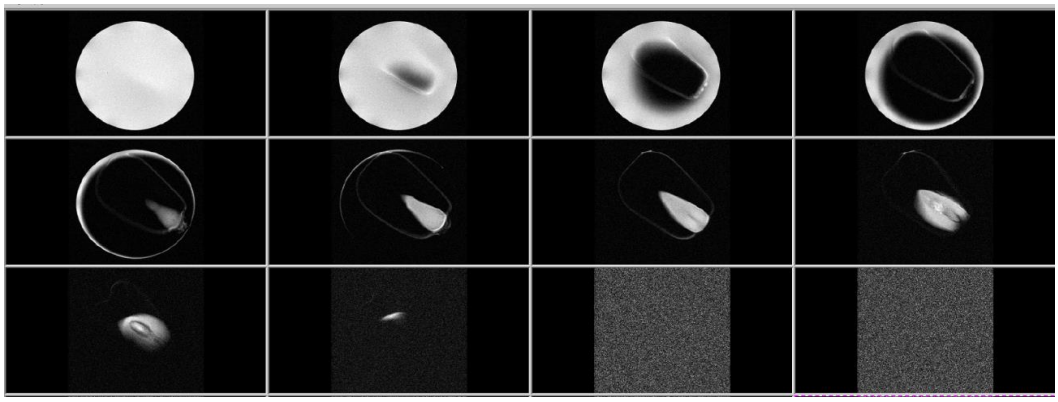

Figure 79 *Axial T_1 weighted image 2th day.*

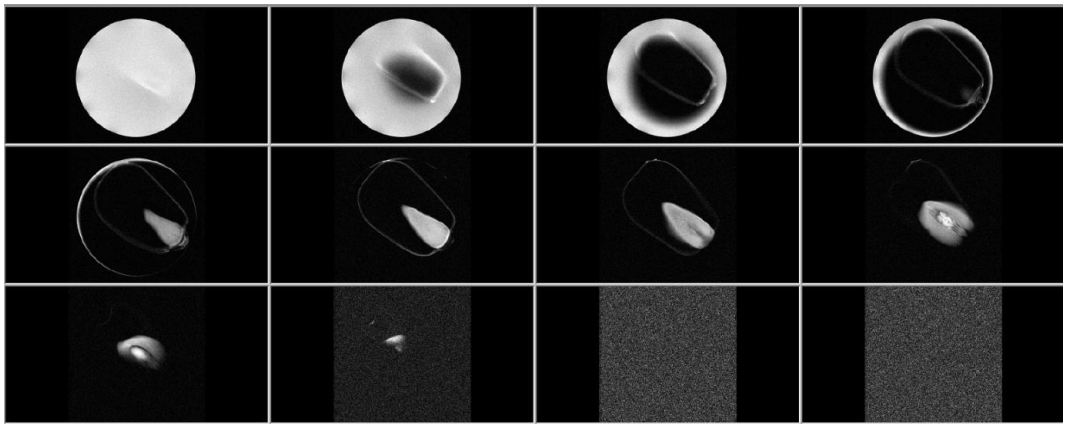

Figure 80 *Axial T_1 weighted image 3th day.*

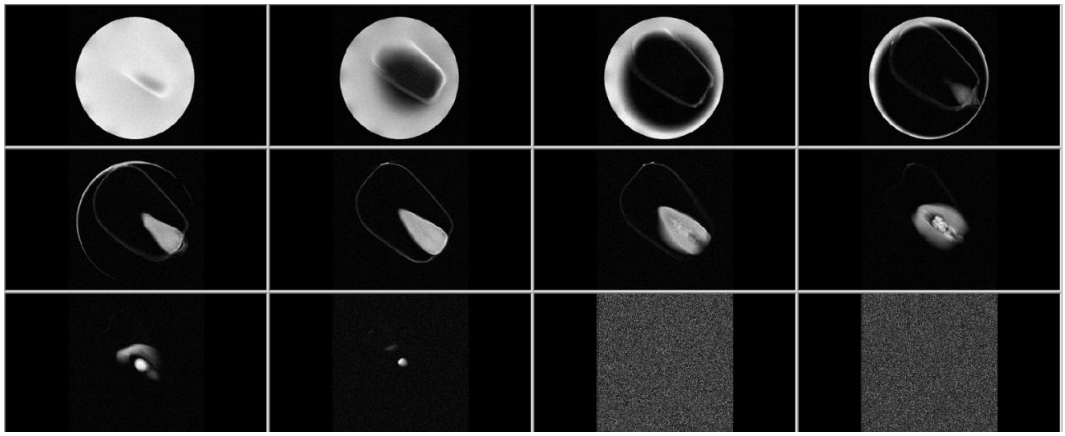

Figure 81 *Axial T_1 weighted image 4th day.*

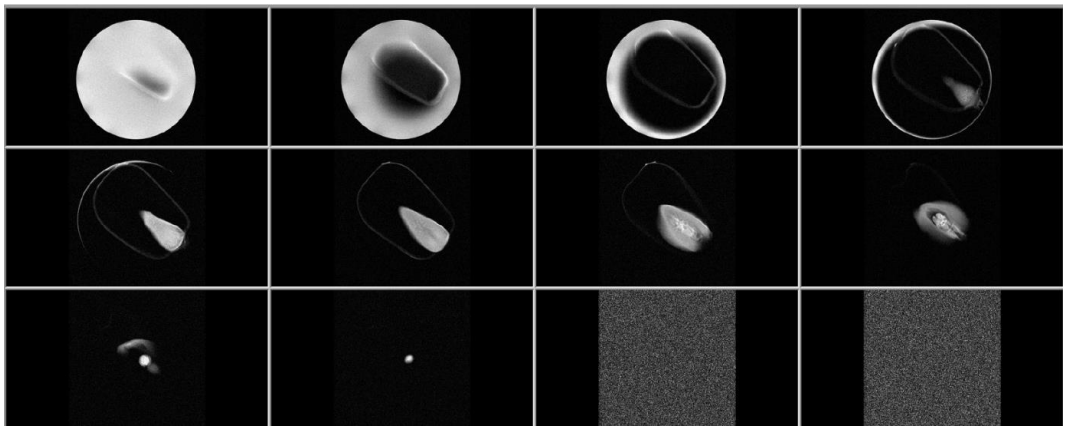

Figure 82 *Axial T1 weighted image 5th day.*

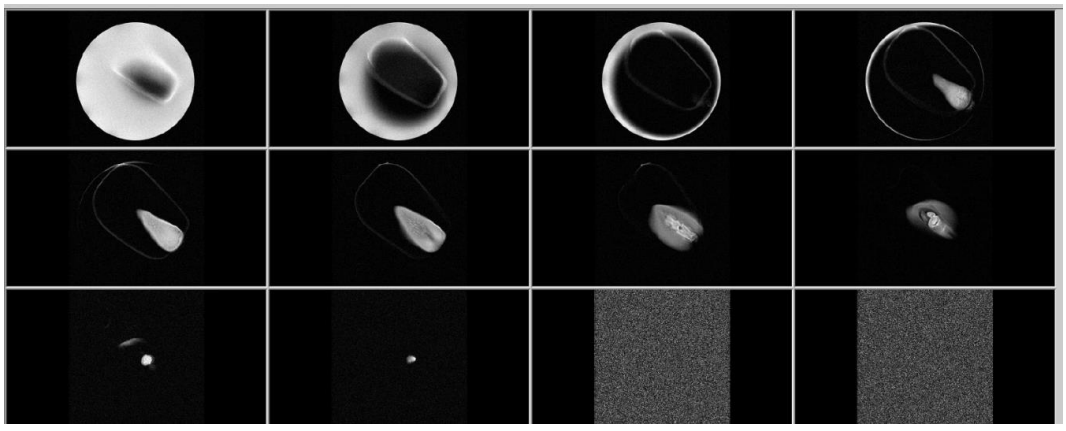

Figure 83 *Axial T1 weighted image 6th day.*

A series of 3D MRI images have also been acquired to monitor the development of a maize seed.

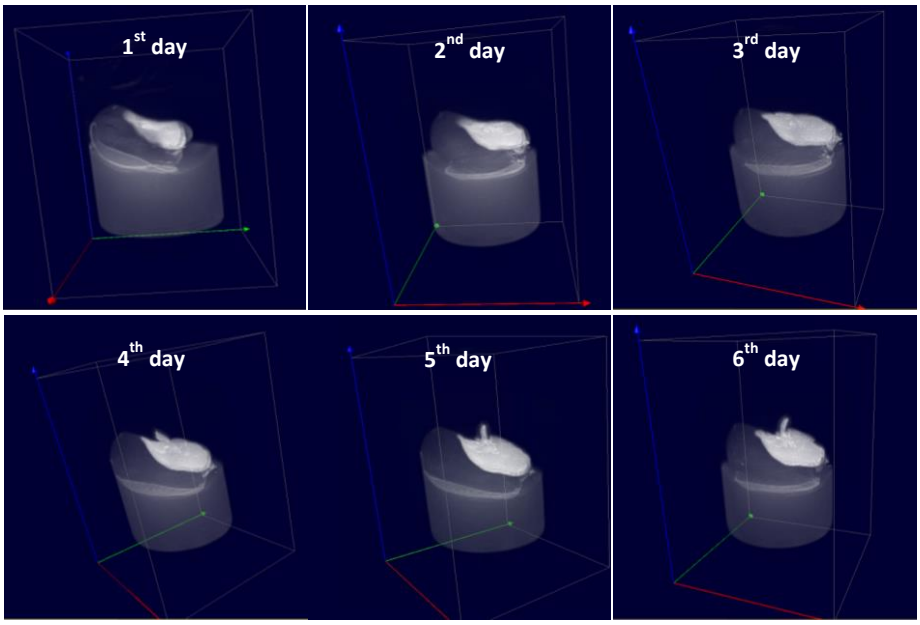

Figure 84 *Sequence of 3D images acquired during six days.*

The seed has continued to grow inside the probe inserted in the NMR. MR image (Figure 85) shows the architecture of the roots but the development of the plant has been complete as shown in Figure 86.

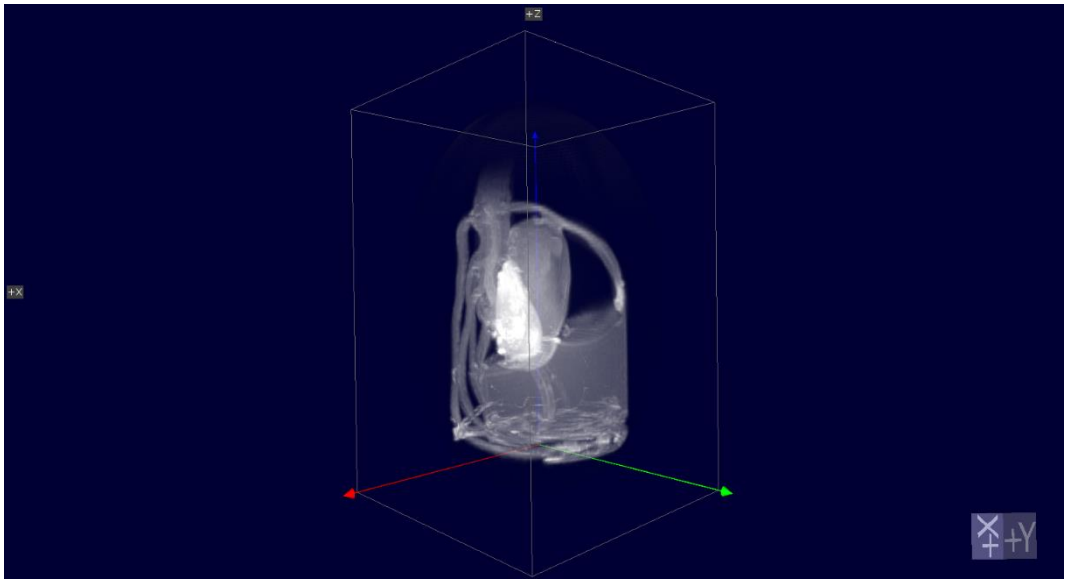

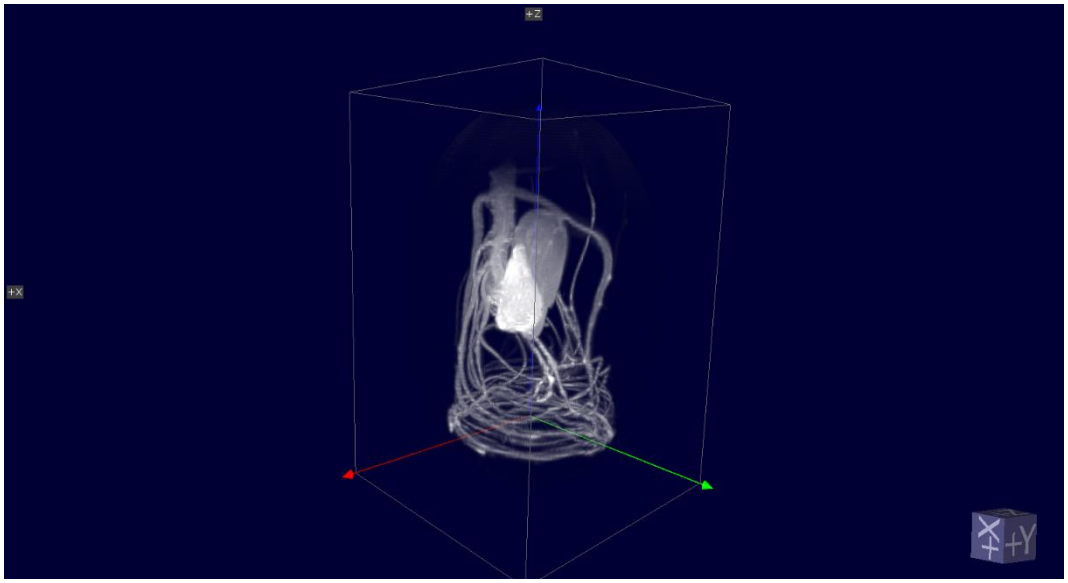

Figure 85 *Maize seed developed. The root architecture is evident.*

Figure 86 *Maize after tot days.*

Using the voxel MR spectroscopy, it is possible to extract the Zea mays spectrum from the MRI image (Figure 87):

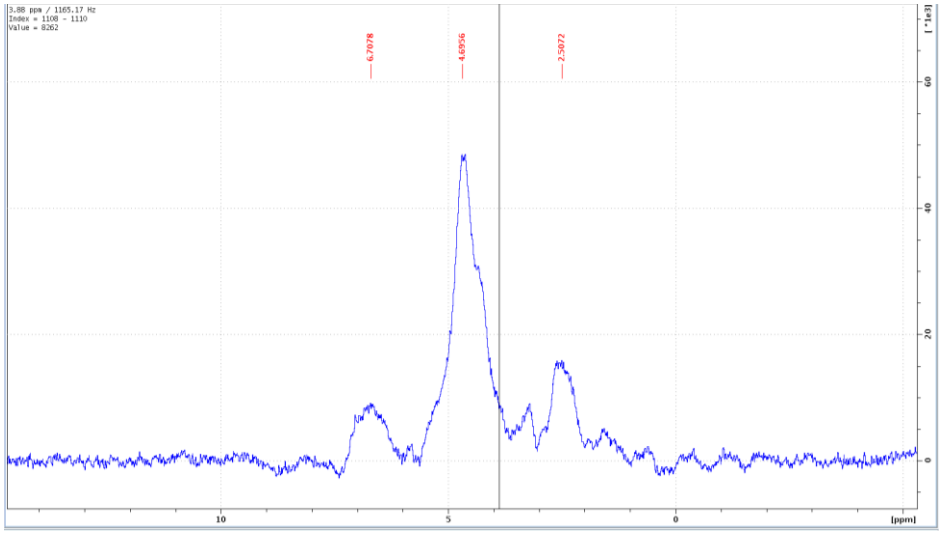

Figure 87 *Spectrum of Zea Mays obtained from a ^{1}H MRI.*

The image is acquired with the PRESS sequence. The noise is very probably due to the small voxel dimension but it looks like how expected, the next figure (Figure 88) shows the spectrum obtained with the ^{13}C-CPMAS NMR on untreated Zea mays [123].

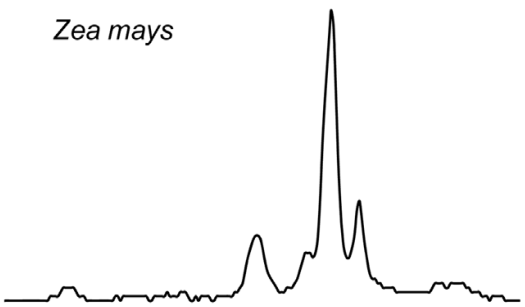

Figure 88 *^{13}C-CPMAS NMR Spectrum of untreated Zea Mays.*

Furthermore, in order to improve the experiment and reproduce as best as possible the natural environment condition for the seed grown, the system will be equipped with the following tools:

- Luminosity sensor
- Temperature sensor

- Humidity sensor
- Bigger tube test (from 1.5 to 2.5 cm)
- Video camera
- ^{13}C Imaging

The idea is to realize a monitoring system for the environmental parameters to control the growing of the plant. The aim is to maintain the root system bathed in nutrient and whole plant in an environment of controlled humidity, temperature, and luminosity intensity [124].

An additional significant improvement will be the ^{13}C imaging that will be performed after the installation of the new Bruker probe acquired in the lab.

Several techniques available in MRI field will be used, such as diffusion and chemical shift imaging, to reinforce and validate the results obtained in this work.

Conclusion and future perspectives

MRI is certainly among the most used technique exploited, in a large number of disciplines, as a diagnostic and assessment tool. Based on the findings of many researches carried out in the recent past, it is possible to affirm that MRI is a successful tool for the monitoring of the internal structures and features of biological samples.

MRI images can provide detailed information, mixing spectroscopy and relaxometry. A difficulty to overcome is that, as seen, MRI is based on a significant number of parameters (PD, T_1, T_2, TR, TE) and, in this respect, each image involve the modification of many of them at the same time.

It is extremely important to consider this feature for a good interpretation of images in order to obtain a consistent description of a process.

In this thesis, we have proposed new ways to apply MRI extracted information in the field of food science. The availability, in our lab, of a new Bruker spectrometer, 7 Tesla – 300 MHz, has given us the possibility to develop new approaches using high magnetic field.

The main idea is to obtain data, extracted from images, in order to turn MRI into a true quantitative tool by combining spatial and relaxation information. The goal is to prove the validity of this approach and improve it, in order to validate MRI as a measurement instrument capable to quantify water content and dynamic, in biological samples under different conditions. We have initially started with a specific and simple food matrix to extend, in a near future, the tests to other fruits or vegetables, to prove that the method is reliable and gives reproducible results. The quantitative moisture distribution maps allow future development and verification of models for prediction of mass transport phenomena in food during

drying to extend the shelf-life of food materials: a major challenge for modern food industry.

The combining of MRI with local spectroscopy allows the development of a new fast procedure to quantify the water content inside the sample under inspection. An advantage of this approach is that the starting point is simply the image and, with respect to the common spectroscopy, the preparation of the sample under study is really easy, non-invasive and absolutely non-destructive.

There are several other possibilities for future improvements of our method. The protocol can be extended to work with new time sequences of images, such as the diffusion-weighted images (DWI).

The same approach could be also very promising in the field of the study of living intact plants. The common features with food is that their functionality is determined by complex multiple length scale architectures. However plants, being living systems, depend critically on transport and signalling processes between and within tissues and organs. The functional tomography of living plants through MRI can represent a great tool to understand the complex regulatory plant performance mechanisms. Part of the work of this thesis has been devoted to the developments of protocols allowing the study of living plants, starting from seed, grew inside the spectrometer and measured continuously during the growth with various procedures. In order to reproduce as best as possible the natural environmental conditions for the seed grown, we plan to improve the whole apparatus with sensors and tools, to implement a monitoring system for the environmental parameters and control the growing of the plants.

Overall, this thesis demonstrated the benefits of MRI and its application, in particular, in food and plants research; this technique results versatile and able to quantify different physical and chemical parameters.

Use and validate the MRI as quantitative tool is our major challenge and the results obtained in this thesis keep us confident about the achievement of this goal. This could hopefully open a way for new methods to perform MRI analysis.

List of acronyms

NMR - Nuclear Magnetic Resonance

MRI - Magnetic Resonance Imaging

2D - 2-dimensional

3D - 3-dimensional

RF- Radio Frequency

FID - Free Induction Decay

PD - Proton Density

T_1 - Spin-Lattice Relaxation Time

T_2 - Spin-Spin Relaxation Time

TR - Repetition time

TE - Echo time

SE – Spin Echo

IR - Inversion Recovery

PRESS - Point Resolved Spectroscopy

STEAM - STimulated Echo Acquisition Mode

CPMG - Carr–Purcell–Meiboom–Gill

MSME - Multi Slice Multi Echo

RARE - Rapid Acquisition with Refocused Echoes

FSE - Fast Spin Echo

RSE - Rapid Spin Echo

GE - Gradient Echo

FLASH - Fast Low Angle Shot

fMRI - functional Magnetic Resonance Imaging

BOLD - Blood Oxygen Level Dependent

DTI - Diffusion Tensor Imaging

FEM - Finite Element Method

M_R - Moisture Ratio

FW - Free Water

LBW- Loosely Bound Water

SBW- Strongly Bound Water

DWI – Diffusion Weighted Images

ROI - Region Of Interest

FOV - Field Of View

MRS - Magnetic resonance spectroscopy

MVS- Multi Voxel Spectroscopy

VOI – Volume Of Interest

ATM - Automated Tuning Routine

BBI - Double Resonance Broadband Probe

CPMAS - Probe Cross Polarization Magic Angle Spinning

HRMAS - Probe High Resolution Magic Angle Spinning

ISA - Image Sequence Analysis

RG - Receiver Gain

List of figures

Bibliography

[1] Callaghan PT. Principles of Nuclear Magnetic Resonance Microscopy. vol. 19. 1991. doi:10.1118/1.596918.

[2] McRobbie DW, Moore EA, Graves MJ, Prince MR. MRI from picture to proton. 2006. doi:10.1017/CBO9780511545405.

[3] M. Coriasco, O.Rampado GBB. Elementi di risonanza magnetica. Dal protone alle sequenze per le principali applicazioni diagnostiche. 2014. doi:10.1007/978-88-470-5641-1.

[4] Bernstein MA, King KF, Zhou XJ. Handbook of MRI Pulse Sequences. 2004. doi:10.1016/B978-0-12-092861-3.X5000-6.

[5] Chen Q, Stock KW, Prasad P V, Hatabu H. Fast magnetic resonance imaging techniques. Eur J Radiol 1999;29:90–100. doi:10.1016/S0720-048X(98)00172-7.

[6] Na. Pulsed Nuclear Magnetic Resonance : Spin Echoes. MIT Dep Phys 2014;0:1–12.

[7] Klose U. Measurement sequences for single voxel proton MR spectroscopy. Eur J Radiol 2008;67:194–201. doi:10.1016/j.ejrad.2008.03.023.

[8] Tal S, Maresky HS, Bryan T, Ziv E, Klein D, Persitz A, et al. MRI in detecting facial cosmetic injectable fillers. Head Face Med 2016;12. doi:10.1186/s13005-016-0124-y.

[9] Di Girolamo M, Mattei M, Signore A, Grippaudo FR. MRI in the evaluation of facial dermal fillers in normal and complicated cases. Eur Radiol 2015;25:1431–42. doi:10.1007/s00330-014-3513-2.

[10] Barale PJ, Fong CG, Green M a., Luft P a., McInturff a. D, Reimer J a., et al. The use of a permanent magnet for water content measurements of wood chips. IEEE Trans Appl Supercond 2002;12:975–8. doi:10.1109/TASC.2002.1018563.

[11] Kalmar JA, Eick JJ, Merritt CR, Shuler SE, Miller KD, McFarland GB, et al. A review of applications of MRI in soft tissue and bone tumors.

Orthopedics 1988;11:417–25.

[12] Chen CA, Chen W, Goodman SB, Hargreaves BA, Koch KM, Lu W, et al. New MR imaging methods for metallic implants in the knee: Artifact correction and clinical impact. J Magn Reson Imaging 2011;33:1121–7. doi:10.1002/jmri.22534.

[13] Detre JA. Magnetic Resonance Imaging. Neurobiol. Dis., Elsevier; 2007, p. 793–800. doi:10.1016/B978-012088592-3/50075-X.

[14] Logothetis NK, Pauls J, Augath M, Trinath T, Oeltermann A. Neurophysiological investigation of the basis of the fMRI signal. Nature 2001;412:150–7. doi:10.1038/35084005.

[15] Inglese M, Fleysher L, Oesingmann N, Petracca M. Clinical applications of ultra-high field magnetic resonance imaging in multiple sclerosis. Expert Rev Neurother 2018;18:221–30. doi:10.1080/14737175.2018.1433033.

[16] Van Der Kolk AG, Hendrikse J, Zwanenburg JJM, Visser F, Luijten PR. Clinical applications of 7 T MRI in the brain. Eur J Radiol 2013;82:708–18. doi:10.1016/j.ejrad.2011.07.007.

[17] Duyn JH. The future of ultra-high field MRI and fMRI for study of the human brain. Neuroimage 2012;62:1241–8. doi:10.1016/j.neuroimage.2011.10.065.

[18] Song YQ. Magnetic resonance of porous media (MRPM): A perspective. J Magn Reson 2013;229:12–24. doi:10.1016/j.jmr.2012.11.010.

[19] Zhang Y, Blümich B. Spatially resolved D-T2 correlation NMR of porous media. J Magn Reson 2014;242:41–8. doi:10.1016/j.jmr.2014.01.017.

[20] Capitani D, Di Tullio V, Proietti N. Nuclear magnetic resonance to characterize and monitor cultural heritage. Prog Nucl Magn Reson Spectrosc 2012;64:29–69. doi:10.1016/j.pnmrs.2011.11.001.

[21] Proietti N, Capitani D, Di Tullio V. Applications of nuclear magnetic resonance sensors to cultural heritage. Sensors (Basel) 2014;14:6977–97. doi:10.3390/s140406977.

[22] Camaiti M, Bortolottic V, Fantazzini P. Stone porosity, wettability changes and other features detected by MRI and NMR relaxometry: A more than

15-year study. Magn Reson Chem 2015;53:34–47. doi:10.1002/mrc.4163.

[23] Blumich B, Casanova F, Perlo J, Presciutti F, Anselmi C, Doherty B. Noninvasive testing of art and cultural heritage by mobile NMR. Acc Chem Res 2010;43:761–70. doi:10.1021/ar900277h.

[24] McDonald PJ. The application of broad line MRI to the study of porous media. Magn. Reson. Imaging, vol. 14, 1996, p. 807–10. doi:10.1016/S0730-725X(96)00168-3.

[25] Gooneratne CP, Li B, Moellendick TE. Downhole Applications of Magnetic Sensors. Sensors (Basel) 2017;17.

[26] Anferova S, Anferov V, Rata DG, Blümich B, Arnold J, Clauser C, et al. A mobile NMR device for measurements of porosity and pore size distributions of drilled core samples. Concepts Magn Reson Part B Magn Reson Eng 2004;23:26–32. doi:10.1002/cmr.b.20020.

[27] Ghojogh JN, Esmaili M, Noruzi-Masir B, Bakhshi P. Quantification of pore size distribution in reservoir rocks using MRI logging: A case study of South Pars Gas Field. Appl Radiat Isot 2017;130:172–87. doi:10.1016/j.apradiso.2017.09.033.

[28] Dobmann G, Kurz JH, Taffe A, Streicher D. Non-Destructive Evaluation of Reinforced Concrete Structures. 2010. doi:10.1533/9781845699604.1.30.

[29] Demco DE, Blümich B. NMR imaging of materials. Curr Opin Solid State Mater Sci 2001;5:195–202. doi:10.1016/S1359-0286(00)00044-9.

[30] Leventis A, Papavassiliou G, Fardis M, Milia F, Chaniotakis E, Dolinsek J, et al. H-1 NMR study of the local magnetic field gradients in evoluting porous structures. An application to cement gels. J Chem Phys 2000;113:7621–6.

[31] Karakosta E, Diamantopoulos G, Katsiotis MS, Fardis M, Papavassiliou G, Pipilikaki P, et al. In situ monitoring of cement gel growth dynamics. Use of a miniaturized permanent halbach magnet for precise1H NMR studies. Ind Eng Chem Res 2010;49:613–22. doi:10.1021/ie901255b.

[32] Milia F, Fardis M, Papavassiliou G, Leventis A. NMR in porous materials. Magn. Reson. Imaging, vol. 16, 1998, p. 677–8. doi:10.1016/S0730-

725X(98)00025-3.

[33] Gummerson RJ, Hall C, Hoff WD, Hawkes R, Holland GN, Moore WS. Unsaturated water flow within porous materials observed by NMR imaging. Nature 1979;281:56–7. doi:10.1038/281056a0.

[34] Carpenter TA, Davies ES, Hall C, Hall LD, Hoff WD, Wilson MA. Capillary water migration in rock: process and material properties examined by NMR imaging. Mater Struct 1993;26:286–92. doi:10.1007/BF02472950.

[35] Kleinberg RL, Straley C, Kenyon WE, Akkurt R, Farooqui SA. Nuclear Magnetic Resonance of Rocks: T1 vs. T2. SPE Annu. Tech. Conf. Exhib., 1993. doi:10.2118/26470-MS.

[36] Kleinberg RL, Kenyon WE, Mitra PP. Mechanism of NMR Relaxation of Fluids in Rock. J Magn Reson Ser A 1994;108:206–14. doi:10.1006/jmra.1994.1112.

[37] Hall LD, Amin MHG, Dougherty E, Sanda M, Votrubova J, Richards KS, et al. MR properties of water in saturated soils and resulting loss of MRI signal in water content detection at 2 tesla. Geoderma 1997;80:431–48. doi:10.1016/S0016-7061(97)00065-7.

[38] Robinson DA, Campbell CS, Hopmans JW, Hornbuckle BK, Jones SB, Knight R, et al. Soil Moisture Measurement for Ecological and Hydrological Watershed-Scale Observatories: A Review. Vadose Zo J 2008;7:358. doi:10.2136/vzj2007.0143.

[39] Link J, Kaufmann J, Schenker K. Water transport in concrete. Magn Reson Imaging 1994;12:203–5. doi:10.1016/0730-725X(94)91516-4.

[40] Beyea SD, Balcom BJ, Bremner TW, Prado PJ, Green DP, Armstrong RL, et al. Magnetic resonance imaging and moisture content profiles of drying concrete. Cem Concr Res 1998;28:453–63. doi:10.1016/S0008-8846(98)00009-X.

[41] Valckenborg RME, Pel L, Hazrati K, Marchand J, Kopinga K. Pore water distribution in mortar during drying as determined by NMR. Mater Struct 2005;34:599–604. doi:10.1617/13586.

[42] Yuya Sakai, Yuki Yokoyama TK. Non-Destructive Imaging of Water Permeation through Cementitious Materials Using MRI n.d.

[43] Hall LD, Gao Amin MH, Evans S, Nott KP, Sun L. Magnetic resonance imaging for industrial process tomography. J Electron Imaging 2001;10:601–7. doi:10.1117/1.1377307.

[44] Creber SA, Vrouwenvelder JS, van Loosdrecht MCM, Johns ML. Chemical cleaning of biofouling in reverse osmosis membranes evaluated using magnetic resonance imaging. J Memb Sci 2010;362:202–10. doi:10.1016/j.memsci.2010.06.052.

[45] Van As H, Van Duynhoven J. MRI of plants and foods. J Magn Reson 2013;229:25–34. doi:10.1016/j.jmr.2012.12.019.

[46] Van As H. Intact plant MRI for the study of cell water relations, membrane permeability, cell-to-cell and long distance water transport. J Exp Bot 2007;58:743–56. doi:10.1093/jxb/erl157.

[47] PálJAKUSCH. Application of Magnetic Resonance Imaging (MRI) in Plant-Water Relationship n.d.

[48] Dagmar van Dusschoten, Ralf Metzner, Johannes Kochs, Johannes A. Postma, Daniel Pflugfelder, Jonas Bühler, Ulrich Schurr SJ. Quantitative 3D Analysis of Plant Roots 13 growing in Soil using Magnetic Resonance Imaging. Plant Physiol n.d.

[49] Pflugfelder D, Metzner R, van Dusschoten D, Reichel R, Jahnke S, Koller R. Non-invasive imaging of plant roots in different soils using magnetic resonance imaging (MRI). Plant Methods 2017;13:102. doi:10.1186/s13007-017-0252-9.

[50] Le Bihan D, Mangin J-F, Poupon C, Clark CA, Pappata S, Molko N, et al. Diffusion tensor imaging: Concepts and applications. J Magn Reson Imaging 2001;13:534–46. doi:10.1002/jmri.1076.

[51] Schulz H, Postma JA, van Dusschoten D, Scharr H, Behnke S. Plant Root System Analysis from MRI Images. Commun. Comput. Inf. Sci., vol. 359 CCIS, 2013, p. 411–25. doi:10.1007/978-3-642-38241-3_28.

[52] Gruwel MLH. In situ magnetic resonance imaging of plant roots. Vadose

Zo J 2014;13. doi:10.2136/vzj2013.08.0158.

[53] Kimura T, Geya Y, Terada Y, Kose K, Haishi T, Gemma H, et al. Development of a mobile magnetic resonance imaging system for outdoor tree measurements. Rev Sci Instrum 2011;82. doi:10.1063/1.3589854.

[54] Nagata A, Kose K, Terada Y. Development of an outdoor MRI system for measuring flow in a living tree. J Magn Reson 2016;265:129–38. doi:10.1016/j.jmr.2016.02.004.

[55] Ebrahimnejad Hamed, Ebrahimnejad Hadi, Salajegheh A. BH. Use of Magnetic Resonance Imaging in Food Quality Control: A Review n.d.

[56] Zhang B, Huang W, Li J, Zhao C, Fan S, Wu J, et al. Principles, developments and applications of computer vision for external quality inspection of fruits and vegetables: A review. Food Res Int 2014;62:326–43. doi:10.1016/j.foodres.2014.03.012.

[57] Melado-Herreros A, Hernandez-sanchez N, Jimenez- T, Verlinden B, Val J, Barreiro P. On-line MRI sequences for the evaluation of Apple internal quality. Insid Food Symp 2013;c:9–12.

[58] Hadimani MB, Rajgoli IU. Applied Engineering in Agriculture: A five-year (2004-2008) citation study. Ann Libr Inf Stud 2010;57:140–5.

[59] Yamakawa M, Khot LR, Ehsani R, Kondo N. Real-time nondestructive citrus fruit quality monitoring system: development and laboratory testing. Agric Eng Int CIGR J 2012;14:117–24.

[60] Lunadei L, Diezma B, Lleó L, Ruiz-Garcia L, Cantalapiedra S, Ruiz-Altisent M. Monitoring of fresh-cut spinach leaves through a multispectral vision system. Postharvest Biol Technol 2012;63:74–84. doi:10.1016/j.postharvbio.2011.08.004.

[61] McGlone VA, Fraser DG, Jordan RB, Künnemeyer R. Internal quality assessment of mandarin fruit by vis/NIR spectroscopy. J Near Infrared Spectrosc 2003;11:323–32. doi:10.1255/jnirs.383.

[62] Rajkumar P, Wang N, EImasry G, Raghavan GS V, Gariepy Y. Studies on banana fruit quality and maturity stages using hyperspectral imaging. J Food Eng 2012;108:194–200. doi:10.1016/j.jfoodeng.2011.05.002.

[63] Kuroki S, Oshita S, Sotome I, Kawagoe Y, Seo Y. Visualization of 3-D network of gas-filled intercellular spaces in cucumber fruit after harvest. Postharvest Biol Technol 2004;33:255–62. doi:10.1016/J.POSTHARVBIO.2004.04.002.

[64] Di Rajagopal Vadivambal DSJ. Bio-Imaging: Principles, Techniques, and Applications n.d.

[65] Ogawa T, Adachi S. Measurement of Moisture Profiles in Pasta During Rehydration Based on Image Processing. Food Bioprocess Technol 2014;7:1465–71. doi:10.1007/s11947-013-1156-y.

[66] Bernin D, Steglich T, Röding M, Moldin A, Topgaard D, Langton M. Multi-scale characterization of pasta during cooking using microscopy and real-time magnetic resonance imaging. Food Res Int 2014;66:132–9. doi:10.1016/j.foodres.2014.09.007.

[67] Kojima TI, Horigane AK, Nakajima H, Yoshida M, Nagasawa A. T2map, moisture distribution, and texture of boiled Japanese noodles prepared from different types of flour. Cereal Chem 2004;81:746–51. doi:10.1094/CCHEM.2004.81.6.746.

[68] Horigane AK, Naito S, Kurimoto M, Irie K, Yamada M, Motoi H, et al. Moisture distribution and diffusion in cooked spaghetti studied by NMR imaging and diffusion model. Cereal Chem 2006;83:235–42. doi:10.1094/CC-83-0235.

[69] Cornillon P, Salim LC. Characterization of water mobility and distribution in low- and intermediate-moisture food systems. Magn Reson Imaging 2000;18:335–41. doi:10.1016/S0730-725X(99)00139-3.

[70] Weglarz WP, Hemelaar M, van der Linden K, Franciosi N, van Dalen G, Windt C, et al. Real-time mapping of moisture migration in cereal based food systems with Aw contrast by means of MRI. Food Chem 2008;106:1366–74. doi:10.1016/j.foodchem.2007.04.077.

[71] Troutman MY, Mastikhin I V., Balcom BJ, Eads TM, Ziegler GR. Moisture migration in soft-panned confections during engrossing and aging as observed by magnetic resonance imaging. J Food Eng 2001;48:257–67.

doi:10.1016/S0260-8774(00)00167-9.

[72] Ramos-Cabrer P, Van Duynhoven JP, Timmer H, Nicolay K. Monitoring of moisture redistribution in multicomponent food systems by use of magnetic resonance imaging. J Agric Food Chem 2006;54:672–7.

[73] Hernández-Sánchez N, Hills BP, Barreiro P, Marigheto N. An NMR study on internal browning in pears. Postharvest Biol Technol 2007;44:260–70. doi:10.1016/j.postharvbio.2007.01.002.

[74] Gonzalez JJ, Valle RC, Bobroff S, Biasi W V, Mitcham EJ, McCarthy MJ. Detection and monitoring of internal browning development in 'Fuji' apples using MRI. Postharvest Biol Technol 2001;22:179–88. doi:10.1016/S0925-5214(00)00183-6.

[75] Ciampa A, Dell'Abate MT, Masetti O, Valentini M, Sequi P. Seasonal chemical-physical changes of PGI Pachino cherry tomatoes detected by magnetic resonance imaging (MRI). Food Chem 2010;122:1253–60. doi:10.1016/j.foodchem.2010.03.078.

[76] Musse M, Quellec S, Devaux M-F, Cambert M, Lahaye M, Mariette F. An investigation of the structural aspects of the tomato fruit by means of quantitative nuclear magnetic resonance imaging. Magn Reson Imaging 2009;27:709–19. doi:10.1016/j.mri.2008.11.005.

[77] Andaur JE, Guesalaga AR, Agosin EE, Guarini MW, Irarrázaval P. Magnetic Resonance Imaging for Nondestructive Analysis of Wine Grapes. J Agric Food Chem 2004;52:165–70. doi:10.1021/jf034886c.

[78] Chen P, McCarthy MJ, Kauten R, Sarig Y, Han S. Maturity Evaluation of Avocados by NMR Methods. J Agric Eng Res 1993;55:177–87. doi:10.1006/jaer.1993.1042.

[79] Zhang L, McCarthy MJ. Black heart characterization and detection in pomegranate using NMR relaxometry and MR imaging. Postharvest Biol Technol 2012;67:96–101. doi:10.1016/J.POSTHARVBIO.2011.12.018.

[80] Mariette F, Collewet G, Davenel A, Lucas T, Musse M. Quantitative MRI in Food Science & Food Engineering. EMagRes 2007:1–8. doi:10.1002/9780470034590.emrstm1272.

[81] Wang S, Lin Z, Xia K, Li Y, Tan M. Dynamics of water mobility and distribution in Sur clam (Mactra chinensis) during dehydration and rehydration processes assessed by low-field NMR and MRI. J Food Meas Charact 2017;11:1342–54. doi:10.1007/s11694-017-9512-7.

[82] Cheng S, Zhang T, Yao L, Wang X, Song Y, Wang H, et al. Use of low-field-NMR and MRI to characterize water mobility and distribution in pacific oyster (Crassostrea gigas) during drying process. Dry Technol 2018;36:630–6. doi:10.1080/07373937.2017.1359839.

[83] Sandulachi E. Water activity concept and its role in food preservation n.d.

[84] Adiletta G, Iannone G, Russo P, Patimo G, De Pasquale S, Di Matteo M. Moisture migration by magnetic resonance imaging during eggplant drying: A preliminary study. Int J Food Sci Technol 2014;49:2602–9. doi:10.1111/ijfs.12591.

[85] Brasiello A, Iannone G, Adiletta G, De Pasquale S, Russo P, Di Matteo M. Mathematical model for dehydration and shrinkage: Prediction of eggplant's MRI spatial profiles. J Food Eng 2017;203:1–5. doi:10.1016/j.jfoodeng.2017.01.013.

[86] Arévalo-Pinedo A, Murr FEX. Kinetics of vacuum drying of pumpkin (Cucurbita maxima): Modeling with shrinkage. J Food Eng 2006;76:562–7. doi:10.1016/j.jfoodeng.2005.06.003.

[87] Que F, Mao L, Fang X, Wu T. Comparison of hot air-drying and freeze-drying on the physicochemical properties and antioxidant activities of pumpkin (Cucurbita moschata Duch.) flours. Int J Food Sci Technol 2008;43:1195–201. doi:10.1111/j.1365-2621.2007.01590.x.

[88] Perez NE, Schmalko ME. Convective drying of pumpkin: Influence of pretreatment and drying temperature. J Food Process Eng 2009;32:88–103. doi:10.1111/j.1745-4530.2007.00200.x.

[89] Krokida MK, Karathanos VT, Maroulis ZB, Marinos-Kouris D. Drying kinetics of some vegetables. J Food Eng 2003;59:391–403. doi:10.1016/S0260-8774(02)00498-3.

[90] Kojima TI, Horigane AK, Yoshida M, Nagata T, Nagasawa A. Change in

the status of water in Japanese noodles during and after boiling observed by NMR micro imaging. J Food Sci 2001;66:1361–5. doi:10.1111/j.1365-2621.2001.tb15215.x.

[91] Khan MIH, Wellard RM, Nagy SA, Joardder MUH, Karim MA. Investigation of bound and free water in plant-based food material using NMR T2relaxometry. Innov Food Sci Emerg Technol 2016;38:252–61. doi:10.1016/j.ifset.2016.10.015.

[92] Srikiatden J, Roberts JS. Moisture transfer in solid food materials: A review of mechanisms, models, and measurements. Int J Food Prop 2007;10:739–77. doi:10.1080/10942910601161672.

[93] Jackson Lim Hwa Keen, Farah Saleena Taip, Mohd. Nordin Ibrahim, Norashikin Abdul Aziz MRISU. Effect of Pre-Treatment on the Physical Properties of Pumpkin Powder. Aust J Basic Appl Sci 2016;10:146–51.

[94] Haile F, Admassu S, Fisseha A. Effects of pre-treatments and drying methods on chemical composition, microbial and sensory qualities of orange-fleshed sweet potato flour and porridge. Am J Food Sci Technol 2015;3:82–8. doi:10.12691/ajfst-3-3-5.

[95] Onwude DI, Hashim N, Janius RB, Nawi N, Abdan K. Modelling the convective drying process of pumpkin (Cucurbita moschata) using an artificial neural network. Int Food Res J 2016;23.

[96] Mayor L, Sereno AM. Modelling shrinkage during convective drying of food materials: A review. J Food Eng 2004;61:373–86. doi:10.1016/S0260-8774(03)00144-4.

[97] Mayor L, Moreira R, Sereno AM. Shrinkage, density, porosity and shape changes during dehydration of pumpkin (Cucurbita pepo L.) fruits. J Food Eng 2011;103:29–37. doi:10.1016/j.jfoodeng.2010.08.031.

[98] van As H, Scheenen T, Vergeldt FJ. MRI of intact plants. Photosynth Res 2009;102:213–22. doi:10.1007/s11120-009-9486-3.

[99] Meagher RB. Phytoremediation of toxic elemental and organic pollutants. Curr Opin Plant Biol 2000;3:153–62. doi:10.1016/S1369-5266(99)00054-0.

[100] Peuke AD, Rennenberg H. Phytoremediation. EMBO Rep 2005;6:497–501.

doi:10.1038/sj.embor.7400445.

[101] Reichenauer TG, Germida JJ. Phytoremediation of organic contaminants in soil and groundwater. ChemSusChem, vol. 1, 2008, p. 708–17. doi:10.1002/cssc.200800125.

[102] Pohlmeier A, Vergeldt F, Gerkema E, As H Van, Dusschoten D Van, Vereecken H. MRI in Soils: Determination of Water Content Changes Due to Root Water Uptake by Means of a Multi-Slice-Multi-Echo Sequence (MSME). Open Magn Reson J 2010;3:69–74. doi:10.2174/1874769801003020069.

[103] Raskin I, Smith RD, Salt DE. Phytoremediation of metals: Using plants to remove pollutants from the environment. Curr Opin Biotechnol 1997;8:221–6. doi:10.1016/S0958-1669(97)80106-1.

[104] Chaney RL, Malik M, Li YM, Brown SL, Brewer EP, Angle JS, et al. Phytoremediation of soil metals. Curr Opin Biotechnol 1997;8:279–84. doi:10.1016/S0958-1669(97)80004-3.

[105] Ghori Z, Iftikhar H, Bhatti MF, Nasar-Um-Minullah, Sharma I, Kazi AG, et al. Phytoextraction: The Use of Plants to Remove Heavy Metals from Soil. Plant Met. Interact. Emerg. Remediat. Tech., 2015, p. 361–84. doi:10.1016/B978-0-12-803158-2.00015-1.

[106] Garnczarska M, Zalewski T, Kempka M. Water uptake and distribution in germinating lupine seeds studied by magnetic resonance imaging and NMR spectroscopy. Physiol Plant 2007;130:23–32. doi:10.1111/j.1399-3054.2007.00883.x.

[107] Manz B. Water Uptake and Distribution in Germinating Tobacco Seeds Investigated in Vivo by Nuclear Magnetic Resonance Imaging. PLANT Physiol 2005;138:1538–51. doi:10.1104/pp.105.061663.

[108] Pohlmeier A, Oros-Peusquens A, Javaux M, Menzel MI, Vanderborght J, Kaffanke J, et al. Changes in soil water content resulting from Ricinus root uptake monitored by magnetic resonance imaging. Vadose Zo J 2008;7:1–8. doi:10.2136/vzj200.

[109] MACFALL JS, JOHNSON GA, KRAMER PJ. Comparative water uptake

by roots of different ages in seedlings of loblolly pine (Pinus taeda L.). New Phytol 1991;119:551–60. doi:10.1111/j.1469-8137.1991.tb01047.x.

[110] van Dusschoten D, Metzner R, Kochs J, Postma JA, Pflugfelder D, Buehler J, et al. Quantitative 3D Analysis of Plant Roots growing in Soil using Magnetic Resonance Imaging. Plant Physiol 2016:pp.01388.2015. doi:10.1104/pp.15.01388.

[111] Oswald SE, Tötzke C, Haber-Pohlmeier S, Pohlmeier A, Kaestner AP, Lehmann E. ScienceDirect Combining Neutron and Magnetic Resonance Imaging to Study the Interaction of Plant Roots and Soil. Phys Procedia 2015;69:237–43. doi:10.1016/j.phpro.2015.07.033.

[112] Terskikh V V., Feurtado JA, Ren C, Abrams SR, Kermode AR. Water uptake and oil distribution during imbibition of seeds of western white pine (Pinus monticola Dougl. ex D. Don) monitored in vivo using magnetic resonance imaging. Planta 2005;221:17–27. doi:10.1007/s00425-004-1426-z.

[113] Pietrzak LN, Frégeau-Reid J, Chatson B, Blackwell B. Observations on water distribution in soybean seed during hydration processes using nuclear magnetic resonance imaging. Can J Plant Sci 2002;82:513–9. doi:10.4141/P01-150.

[114] Fountain DW, Forde LC, Smith EE, Owens KR, Bailey DG, Callaghan PT. Seed development in Phaseolus vulgaris L. cv. Seminole. 3. NMR imaging of embryos during ethylene-induced precocious germination. Seed Sci Res 1998;8:357–65. doi:10.1017/S0960258500004281.

[115] Macfall JS, Johnson GA. Plants, seeds, roots, and soils as applications of magnetic resonance microscopy. eMagRes, vol. 1, 2012, p. 147–54. doi:10.1002/9780470034590.emrstm0396.

[116] Metzner R, van Dusschoten D, BÃ¼hler J, Schurr U, Jahnke S. Belowground plant development measured with magnetic resonance imaging (MRI): exploiting the potential for non-invasive trait quantification using sugar beet as a proxy. Front Plant Sci 2014;5. doi:10.3389/fpls.2014.00469.

[117] Ibrahim SI, Abdel Lateef MF, Khalifa HMS, Abdel Monem AE. Phytoremediation of atrazine-contaminated soil using Zea mays (maize). Ann Agric Sci 2013;58:69–75. doi:10.1016/J.AOAS.2013.01.010.

[118] Liao C, Xu W, Lu G, Liang X, Guo C, Yang C, et al. Accumulation of Hydrocarbons by Maize (Zea mays L.) in Remediation of Soils Contaminated with Crude Oil. Int J Phytoremediation 2015;17:693–700. doi:10.1080/15226514.2014.964840.

[119] Hechmi N, Aissa N Ben, Abdennaceur H, Jedidi N. PHYTOREMEDIATION POTENTIAL OF MAIZE (ZEA MAYS L.) IN CO-CONTAMINATED SOILS WITH PENTACHLOROPHENOL AND CADMIUM. Int J Phytoremediation 2013;15:703–13. doi:10.1080/15226514.2012.723067.

[120] Boone, C.; Bond, C.; Buhl, K.; Stone D. Copper Sulfate General Fact Sheet. Natl Pestic Inf Center, Oregon State Univ Ext Serv 2012:1–3. http://npic.orst.edu/factsheets/cuso4gen.html.

[121] Chemistry IU of P and A. Nomenclature of Inorganic Chemistry: IUPAC Recomendations 2005. 2005. doi:10.1515/ci.2005.27.6.25.

[122] Iengo I, Armiero M. The politicization of ill bodies in Campania, Italy. J Polit Ecol 2017;24:44–58.

[123] Bonanomi G, Ippolito F, Cesarano G, Vinale F, Lombardi N, Crasto A, et al. Biochar chemistry defined by13C-CPMAS NMR explains opposite effects on soilborne microbes and crop plants. Appl Soil Ecol 2018;124:351–61. doi:10.1016/j.apsoil.2017.11.027.

[124] Hills B. Magnetic resonance imaging in food science n.d.